Development of nanoscaled chemical systems for enabling atomically resolved reaction dynamics of model systems

Dissertation

with the aim of achieving a doctoral degree

at the Faculty of Mathematics, Informatics and Natural Sciences

Department of Chemistry

of Universität Hamburg

submitted by Maria Katsiaflaka

2019, Hamburg

i. Zusammenfassung

In den letzten Jahren bestand großes Interesse an der Synthese von Dünnschichtmaterialien. Die jüngsten Fortschritte bei den Techniken der Herstellung von Dünnschichten führten zu Durchbrüchen in Bereichen wie Leuchtdioden (LEDs), Energieumwandlungsvorrichtungen (Solarzellen), Speichervorrichtungen (Batterien), als auch Wirkstoffabgabe in vivo mittels Dünnschichten. Neben der breiten technologischen Anwendung dieser Systeme sind sie auch ideale Kandidaten für zeitaufgelöste Studien ihrer molekularen Struktur, mit dem Ziel, das derzeitige Verständnis für die Funktionsweise der Chemie zu verbessern und neue Wege zur Kontrolle der Materialeigenschaften zu eröffnen. Damit diese Versuche erfolgreich sind, müssen extrem hohe Anforderungen an Probeneigenschaften und -qualität gestellt werden.

In dieser Arbeit konzentriert sich der Autor auf die Herstellung und vollständige Charakterisierung kleiner Modellsysteme einschließlich organometallischer, photochromer und biologischer Analoga, um deren Kompatibilität mit Femtosekunden-Elektronenbeugungungstechniken (FED) zu demonstrieren, und somit allgemeine Methoden zur systematischen Untersuchung molekularer Strukturdynamik bereitzustellen. Das Erreichen dieses Ziels ermöglicht die direkte Beobachtung atomarer Bewegungen, wodurch die grundlegenden Prozesse der Chemie und Physik in atomaren Längen- und Zeitskalen beleuchtet werden. Um diese nanoskaligen dünnen Molekülschichten vollständig zu charakterisieren, wurden Elektronenmikroskopie, Elektronenbeugung, Spektroskopie und verschiedene Oberflächenanalysetechniken verwendet.

Metall-organische Gerüste (MOFs) und oberflächenmontierte Metall-organische Gerüste (SURMOFs) wurden unter Verwendung der Langmuir-Blodgett (LB) -Technik hergestellt. Durch Atomkraftmikroskopie (AFM) und Transmissionselektronenmikroskopie (TEM) wurden die auf Festkörperoberflächen gebildeten Monoschichten hinsichtlich ihrer Kristallinität und Dicke charakterisiert. Im Rahmen dieser Untersuchungen stellte der Autor erstmals TEM-Beugungsmuster und AFM-Bilder eines LB-SURMOF zur Verfügung. Darüber hinaus wurde der Photochromismus eines neuen amphiphilen Dithienylethen (DTE) -Konzepts untersucht. AFM- und TEM-Studien belegen, dass reversible morphologische Veränderungen in diesen Schichten auftreten, die einer Anregung mit ultraviolettem (UV) und sichtbarem

Licht unterliegen. Schließlich wurde die Leistungsfähigkeit verschiedener Techniken einschließlich der „Messerschneide" -Kristallisation, des Spincoating, der Ultramikrotomie und von der Langmuir-Blodgett / Schaefer -Methode für die Herstellung atomar dünner Vitamin-B12-Filme verglichen.

In dieser Arbeit wurden erhebliche Fortschritte bei der Herstellung und Charakterisierung verschiedener Arten organischer Dünnschichten erzielt, die den Weg für zukünftige strukturdynamische Untersuchungen mit der FED-Technik ebnen.

ii. Abstract

Over the past years, there has been much interest in the synthesis of thin film materials. Recent advances in thin film deposition techniques have led to breakthroughs in areas such as light emitting diodes (LEDs), energy conversion devices (solar cells), storage devices (batteries) and thin film drug delivery. Besides the wide technological application of these systems, they also promise to be ideal candidates for time resolved studies with the aim of improving the current understanding of how chemistry works, and opening up new ways of controlling material properties. For these experiments to be successful, extremely demanding requirements in terms of sample properties and quality have to be met.

In this thesis, the author focuses on the fabrication and full characterization of small model systems including organometallic, photochromic and biological analogues to demonstrate their compatibility with femtosecond electron diffraction (FED) techniques, with the ultimate goal of providing a general means to systematically study molecular dynamics at the atomic level. Achieving this objective will allow the direct observation of atomic motions, thus shedding light on the fundamental processes of chemistry and physics at atomic length- and timescales. To fully characterize these nanoscale thin molecular layers, electron microscopy, electron diffraction, spectroscopy, and various surface analysis techniques were used.

Metal–organic frameworks (MOFs), and surface-mounted metal–organic frameworks (SURMOFs), were fabricated using the Langmuir- Blodgett (LB) technique. Atomic force microscopy (AFM) and transmission electron microscopy (TEM) techniques were implemented to characterize the monolayers formed on solid surfaces in terms of their crystallinity and thickness. As part of these studies, the author provided for the first time TEM diffraction patterns and AFM images on a LB-SURMOF. Furthermore, the photochromism of a new amphiphilic dithienylethene (DTE) concept was studied, with AFM and TEM studies proving that reversible morphological changes occur in these layers subject to ultraviolet (UV) and visible light excitation. Finally, the performance of several techniques including 'knife-edge' crystallization, spin coating, ultramicrotomy, and Langmuir–Blodgett/Schaefer, were compared for the fabrication of atomically thin vitamin B_{12} films. In this work, considerable advancements in the fabrication and characterization of different types of thin organic films

have been achieved, paving the way for future structural dynamics investigations by the FED technique.

Ιθάκη

Σὰ βγεῖς στὸν πηγαιμὸ γιὰ τὴν Ἰθάκη,
νὰ εὔχεσαι νά ᾿ναι μακρὺς ὁ δρόμος,
γεμάτος περιπέτειες, γεμάτος γνώσεις.

Τοὺς Λαιστρυγόνας καὶ τοὺς Κύκλωπας,
τὸν θυμωμένο Ποσειδῶνα μὴ φοβᾶσαι,
τέτοια στὸν δρόμο σου ποτέ σου δὲν θὰ βρεῖς,
ἂν μέν᾿ ἡ σκέψις σου ὑψηλή, ἂν ἐκλεκτὴ
συγκίνησις τὸ πνεῦμα καὶ τὸ σῶμα σου ἀγγίζει.

Τοὺς Λαιστρυγόνας καὶ τοὺς Κύκλωπας,
τὸν ἄγριο Ποσειδῶνα δὲν θὰ συναντήσεις,
ἂν δὲν τοὺς κουβανεῖς μὲς στὴν ψυχή σου,
ἂν ἡ ψυχή σου δὲν τοὺς στήνει ἐμπρός σου.

Νὰ εὔχεσαι νά ᾿ναι μακρὺς ὁ δρόμος.
Πολλὰ τὰ καλοκαιρινὰ πρωινὰ νὰ εἶναι
ποῦ μὲ τί εὐχαρίστηση, μὲ τί χαρὰ
θὰ μπαίνεις σὲ λιμένας πρωτοειδωμένους.

Νὰ σταματήσεις σ᾿ ἐμπορεῖα Φοινικικά,
καὶ τὲς καλὲς πραγμάτειες ν᾿ ἀποκτήσεις,
σεντέφια καὶ κοράλλια, κεχριμπάρια κ᾿ ἔβενους,
καὶ ἡδονικὰ μυρωδικὰ κάθε λογῆς,
ὅσο μπορεῖς πιὸ ἄφθονα ἡδονικὰ μυρωδικά.

Σὲ πόλεις Αἰγυπτιακὲς πολλὲς νὰ πᾷς,

νὰ μάθεις καὶ νὰ μάθεις ἀπ᾽ τοὺς σπουδασμένους.

Πάντα στὸ νοῦ σου νά ᾽χεις τὴν Ἰθάκη.

Τὸ φθάσιμον ἐκεῖ εἶν᾽ ὁ προορισμός σου.

Ἀλλὰ μὴ βιάζεις τὸ ταξίδι διόλου.

Καλλίτερα χρόνια πολλὰ νὰ διαρκέσει.

Καὶ γέρος πιὰ ν᾽ ἀράξεις στὸ νησί,

πλούσιος μὲ ὅσα κέρδισες στὸν δρόμο,

μὴ προσδοκώντας πλούτη νὰ σὲ δώσει ἡ Ἰθάκη.

Ἡ Ἰθάκη σ᾽ ἔδωσε τ᾽ ὡραῖο ταξίδι.

Χωρὶς αὐτὴν δὲν θά ᾽βγαινες στὸν δρόμο.

Ἄλλα δὲν ἔχει νὰ σὲ δώσει πιά.

Κι ἂν πτωχικὴ τὴν βρεῖς, ἡ Ἰθάκη δὲν σὲ γέλασε.

Ἔτσι σοφὸς ποὺ ἔγινες, μὲ τόση πεῖρα,

ἤδη θὰ τὸ κατάλαβες οἱ Ἰθάκες τὶ σημαίνουν.

Κ. Π. Καβάφης

Ithaka

Once you set out for Ithaka

hope your road to be long,

full of adventures, full of knowledge.

Don't be afraid of the Laistrygonians and the Cyclops,

the angry Poseidon

you'll never find them on your way

if you keep your thoughts high,

if rare excitement touches your spirit and your body.

You won't meet the Laistrygonians and the Cyclops,

the wild Poseidon

unless you bring them along inside your soul,

unless your soul puts them in front of you.

Hope your road to be long

may there be many summer mornings

when you'll enter with pleasure, with joy,

the harbours you've seen for the first time

Stop in Phoenician trading stations

and get the good wares

pearls and corals, ambers and ebony,

and sensual herbs of every kind

as many sensual herbs as you can

Go to many Egyptian cities

to study and learn from the educated ones

keep Ithaka always in your mind

your arrival there is your destiny

But don't rush the journey at all

it better lasts for many years,

and then when you're old to stay on the island,

wealthy with all you've gained on the way

without expecting Ithaka to make you rich.

Ithaka gave you the beautiful journey.

without her you wouldn't have set out

there's nothing else to give you anymore

And if you find her poor, Ithaka hasn't fooled you.

now that you became wise with so much experience

you should have already understood what Ithakas mean

K. P. Kavafis

Στην υπέροχη οικογένειά μου....

List of publications

Maria Katsiaflaka, Andreas Rossos, Heshmat Noei, Elena Koenig, Robert Bucker, R. J. Dwayne Miller. 'Atomically thin Monolayers of Metal–Organic Frameworks (MOFs) through Implementing a Langmuir–Schaefer Method'. AIP Conference Proceedings 2018, 2022, 020007.

Andreas Rossos*, Maria Katsiaflaka*, Jianxin Cai*, Sean M. Myers, Elena Koenig, Robert Bucker, Sercan Keskin, Gunther Kassier, Regis Y. N. Gengler, R. J. Dwayne Miller, R. Scott Murphy. 'Photochromism of Amphiphilic Dithienylethenes as Langmuir–Schaefer Films'. Langmuir 2018, **34**, 10905–10912.

Andreas Rossos*, Maria Katsiaflaka*, Elena Koenig, Robert Bucker, Wesley D. Robertson, R. J. Dwayne Miller. 'Atomically Thin Vitamin B_{12} as Langmuir–Schaefer Films for Electron Diffraction'. To be submitted.

List of abbreviations

2D Two-dimensional

3D Three-dimensional

A Area

A absorbance

BTC Benzene tricarboxylic acid

C concentration

°C Celsius

cm Centimetre

Cryo-EM Cryo electron microscopy

DC Glow discharge

DMF Dimethylformamide

DPPC Dipalmitoylphosphatidylcholine

DTE-c Dithienylethene closed form

DTE-o Dithienylethene open form

DTEs Dithienylethenes

E Molar absorptivity coefficient of the material

E$_B$ Binding energy

E$_k$ Kinetic energy

ESCA Electron spectroscopy for chemical analysis

eV Electron volt

FED femtosecond electron diffraction

fs Femtosecond

BAM Brewster angle microscopy

Å Angstrom

AFM Atomic force microscopy

B$_{12}$ Cyanocobalamin

hv Photon energy

I Intensity of light leaving a sample cell

I$_o$ Intensity of light over a sample cell

keV kilo electronvolt

kT Boltzmann constant

kV kilo volt

LB Langmuir–Blodgett

LB trough Langmuir–Blodgett trough

LbL Layer by Layer

LED Light emitting diodes

LN$_2$ Liquid nitrogen

LS Langmuir–Schaefer

m metre

M molarity

mA Milli-amber

min minute

mN Milli newton

MOFs Metal–organic frameworks

MΩ Milli-Q

N Number of molecules

nm nanometre

P Pressure

ppm Parts per million

PMMA Poly (methyl 2-methylpropenoate)

RPM Revolutions per minute

RT Room temperature

SAED Selected area electron diffraction

Si Silicon

Si₃N₄ Silicon nitride

SURMOFs Surface-anchored metal–organic frameworks

T Temperature

t Thickness

TEM Transmission electron microscopy

Uv-vis Ultraviolet-visible

V volume

v/v volume per volume

W Watt

w/v Weight per volume

XPS X-ray photoelectron spectroscopy

θ Angle

λ Absorption

μL Microliter

μm Micrometre

π-A Surface pressure-area

ω Angular velocity

% Per ce

Contents

1. Introduction

Most of nature is dynamic, growing and changing due to chemical reactions. Scientists have always been trying to understand the connection between the structure of matter and its properties. Observing the atomic motions during their primary events causing changes in the structure of matter has been an ultimate goal[1].

The discovery of X-ray diffraction in 1912 by the physicist Max von Laue, which provided an experimental tool for studying atomic positions within crystals[2, 3], is regarded as a ground-breaking turning point in physics and chemistry. The technique immediately allowed scientists to observe the structure of materials with an unprecedented resolution. In the following years, it was understood that some of the properties of crystalline materials are directly related to their crystallographic structure or, simply put, to the way the atoms, ions or molecules are arranged in space.

The typical distance between two atoms in a molecule is about 1 Å (10^{-10} m) on average. If we consider a bond displacement of 1 Å, and the movement of the atoms to be at the speed of sound, the time it would take for a bond to break is approximately 100 fs[4, 5]. Although chemical reactions can occur on longer or shorter time scales depending on the reaction, we can regard 100 fs as a characteristic shutter speed required to capture the molecular reactions. This approximate time scale is also suggested by the Arrhenius theory for molecular motions[1, 5]. Therefore, the challenge is to build a 'molecular movie camera' that would be able to capture these molecular motions.

The dream experiment of directly observing atomic motions in real time has been realized[6]. Femtosecond electron diffraction (FED) gives a direct view of the atomic structure evolution of specimens by providing time-dependent atomic pair correlation function in case of amorphous samples, or time dependent Bragg peak intensities in case of crystals. In this way, structural dynamics of solids, liquids and gases, as well as phase transitions can be investigated[7]. In a FED experiment, one has a short optical excitation pulse (pump) to trigger the dynamics of interest, and an electron pulse of similar duration (probe) to track the atomic motions with a temporal resolution that is typically in the few 100 fs range. The diffraction pattern is recorded for different time delays and for different crystal orientations, providing

the necessary information to map the structural changes. This approach has allowed achieving the long-held dream to see atoms in action during structural changes. Atomic motions measured on this time scale can be called 'molecular movies'.

One of the most important factors in determining the quality of the diffraction patterns in FED, is the sample quality. To get good resolution in both imaging and diffraction with electrons[5, 8], the sample must be sufficiently thin so as to avoid multiple elastic and inelastic scattering of the electron beam, which would degrade the diffraction pattern and make its interpretation more difficult. A thickness of about 100 nm or less is desirable for organic samples, assuming 100 keV electrons. Transmission electron diffraction studies conducted at lower energies would require thinner layers down to monolayer dimensions[8, 9].

Another aspect that is very important for thin film samples is the crystallinity. Single crystal samples produce diffraction patterns with single distinct peaks. An amorphous or polycrystalline sample will give rise to a smooth radial function or a series of well- defined diffraction rings, respectively. The highest symmetry case of a single crystal diffraction pattern generally allows more detailed structural information to be extracted. For a time-resolved electron diffraction experiment, the sample capacity for undergoing the desired photoexcitation reaction is also of critical importance. For liquid and gas samples, there is more freedom for reaction processes, but in the solid state, the types of reactions that can be studied with this technique are very limited. For reversible processes, which are rather desired for pump probe experiments as they allow the same spot on the sample to be repeatedly pumped and probed to accumulate the signal, the sample should not be damaged by the laser pump pulse. It is an experimental observation that thin samples are more likely to be damaged by photo-excitation[8-10]. This calls for a trade-off between the advantages of thin samples in terms of electron beam penetration and resolution.

When it comes to irreversible samples (single-shot experiments), each measurement requires a fresh sample area. This means that a suitable sample needs to have a large uniform area, over which the sample proprieties are kept identical. A non-uniform sample with defects will distort the diffraction, making the reconstruction extremely difficult if not impossible[5, 11, 12].

Thus, it becomes clear that the sample preparation process for femtosecond electron diffraction is a demanding task. To meet the sample requirements for these experiments and

to produce it continuously, some limitations must be overcome. Suitably dimensioned (large area) samples which are homogenous as well as sufficiently thin are very difficult to fabricate.

In the present work, three different systems of real interest for time resolved electron diffraction studies as well as applications in a wide range of technological and industrial fields, were fabricated and characterized. The first systems studied were metal organic frameworks (MOFs), which comprise crystalline porous inorganic–organic hybrid materials, with a wide range of applications. To combine MOFs into specific devices, the growth of highly oriented surface-mounted metal–organic frameworks (SURMOFs) was controlled using the Langmuir–Blodgett/Langmuir–Schaefer (LB/LS) film fabrication technique. An important outcome of this thesis is that the LB technique provides a continuous and highly oriented 2D ultra-thin MOF monolayer that is deposited on a substrate with oriented crystalline structure. This system is a promising candidate for recording 'molecular movies'. Unfortunately, the domain sizes obtained thus far are too small to provide sufficiently large area single crystals for fs electron diffraction.

Secondly, dithienylethene compounds (DTEs) were studied. These can reversibly switch between two isomeric forms, ring-open isomer (colourless) and ring-closed isomer (coloured), when they are in the solution phase. The fully electroactive DTEs are unstable when they are in the coloured form and undergo ring-opening in the dark and at ambient temperature. In this thesis, the photochromism of three different amphiphilic dithienylethenes was studied under different irradiation conditions. Atomically thin monolayers were created for each of the three compounds to study the changes in morphology after every irradiation step.

The third system studied in this thesis was vitamin B_{12} (cyanocobalamin). Vitamin B_{12} has the most complex structure of all the vitamins. It is used as a cofactor for many proteins and its unique structure exhibits photochemistry not yet understood. It is hoped that the real-time observations will eventually help to decode these transitions. Remarkable efforts have been invested to create a thin film that could provide insight into the structure and function of this biological system and, although the ultimate goal has not yet been reached, considerable progress has been made. The detailed results are described in the body of the thesis.

Overview of the thesis:

Chapter 1 is a general introduction and describes the aim of this thesis, the term 'molecular movie', the electron diffraction technique and the main sample requirements for time resolved studies. Chapter 2 focuses on the nomenclature and description of the preparation procedures and materials used. Chapters 3–5 present the results, a short discussion, and a brief introduction of each system. More specifically, Chapter 3 introduces surface-anchored metal–organic frameworks (SURMOFs), starting with a short description of MOF material properties and applications, continuing with the specific method for thin film MOF fabrication, and concluding with the film characterization. The goal of this project was to create MOF thin films to provide the 'molecular movie'[5]. In Chapter 4, the amphiphilic dithienylethene compounds (DTEs) are introduced. The goal of this was to investigate the photochromism of amphiphilic DTEs in organized assemblies. The author evaluated their spreading behaviour and stability of Langmuir films on three different DTEs. Photochromism and the nanostructure of multilayer LS films using different characterization techniques also presented. In chapter 5, vitamin B_{12} thin film formation using state-of-the-art and traditional techniques is described. The formation of 2D films and their characterization are presented in detail. The main purpose was to characterize the photochemistry of cyanocobalamin (Vitamin B_{12}) in the solid state. In Chapter 6, the conclusions and the prospects are presented.

2. Aim of the work: sample preparation for making molecular movies

2.1 Thin film fabrication techniques

In this thesis, we used techniques such as Langmuir–Blodgett to create thin films from soluble organic materials. For precise thickness control, knife-edge and spin coating for thin film crystallization was used. Furthermore, an ultra-microtome was used to get thin film sections from bulky crystals, grown in different ways.

2.1.1 The Langmuir–Blodgett (LB) and Langmuir–Schaefer (LS) techniques

Usually, Langmuir films comprise surface active agents of surfactants captured at the interface between two phases, usually liquid–gas or liquid–liquid[13]. Surfactants are amphiphilic molecules (having both a hydrophilic and a hydrophobic part).

Surfactants dissolve into non-aqueous volatile solvents but are left at the liquid–gas interface when applied onto a polar liquid surface as it evaporates[13]. The head groups, which constitute the hydrophilic part, pull the molecule into the bulk of the water, whereas the tail groups, which form the hydrophobic part, point towards air. A surface monolayer can be created only if the amphiphilic balance between hydrophilic and hydrophobic parts is correct[14].

2.1.1.1 The Langmuir–Blodgett and Langmuir–Schaefer deposition methods

After spreading a few microliters of any surfactant on the water surface, all the molecules are spread around on the free surface area. Applying an external force on the floating surfactant molecules, their positions will change within the trough, and finally, after the application of an appreciable compression force, a solid film should be assembled[13, 15]. The formed monolayer compression undergoes a few phase transitions between solid, liquid, and gas phases (Fig. 2.1).
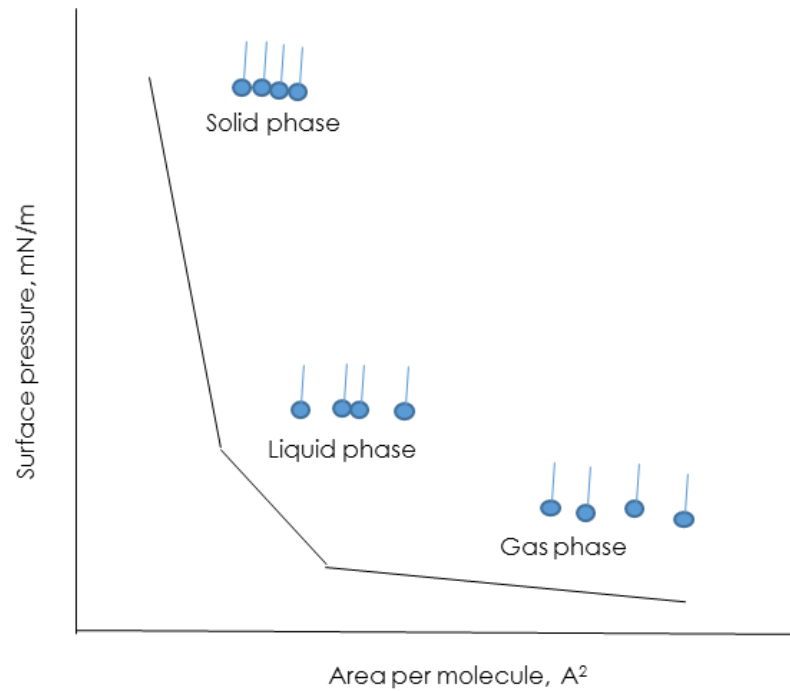
Figure 2.1: Schematic diagram of LB trough and a general isotherm curve of a Langmuir monolayer

Accordingly, a phase diagram of a surfactant can be easily extracted by measuring a surface pressure-area (π-a) isotherm, meaning that a relation curve regarding the pressure versus area per molecule is extracted while the temperature is balanced.

In a typical run, after the molecules have been dispersed on the surface and the carrier solvent has been left to evaporate, a 2D mobile interface is formed that is referred to as gas phase. This phase is created as a result of the large distances between the molecules. After the solvent has evaporated, the barrier can move to compress the molecules for as long as the surface pressure changes are observed. The π-a isotherm allowed Langmuir to prove the existence of different phase transitions for different systems.

In the gas phase, the area available per molecule is large. Therefore, the floating surfactant molecules can hardly interact with each other. Indeed, since every molecule has an energy kT (kT/2 per degree of freedom), this forces them to move and collide with other molecules, as well as on the wall of the container, as is the case with a perfect 2D gas. The pressure of this 2D gas can be estimated by the gas law equation (PV=NkT), where P is the pressure of the 2D gas, A is the total container area, N is the number of molecules, and kT is the Boltzmann constant multiplied by the temperature T. The gas law then becomes: PA=NkT.

The transition from gas to liquid can be observed during the barrier motion. This exists for surface area values estimated according to the size of the long axis of the molecules. Thus, the molecules are arranged in a coherent way, but they are still relatively closely packed. Further compression leads to the next phase transition, while the liquid turns into solid state. Under these conditions, the molecules are closely packed. The application of more pressure results in a sudden increase in the surface pressure, presenting the case of a 3D solid. Increasing the pressure and the compression leads to a monolayer 'collapse'[16-18].

The collapse can be noticed as a sharp breaking of the solid state (Fig. 2.2). Once it takes place, the pressure drops suddenly and then increases again. As a result, the reformation of the already created monolayer into a double or triple layer occurs, which turns into a micro crystallite. It is understandable that the increase in pressure of a well-defined and compact layer leads to the formation of cracks, while further compression results in the monolayers' collapse.
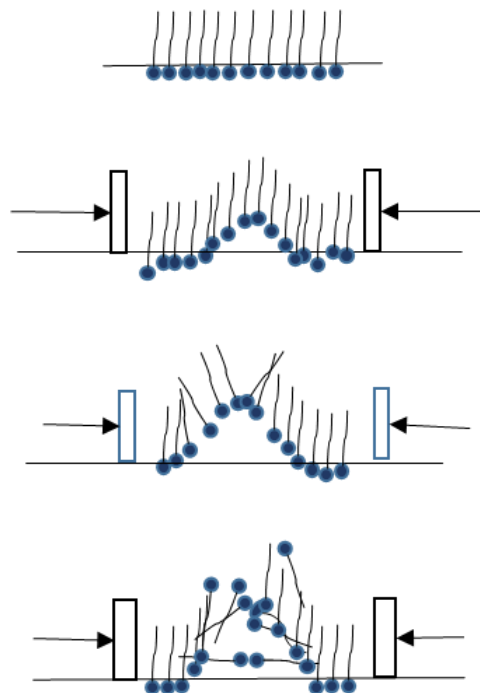
Figure 2.2: A schematic 'collapse' representation, further increase in the applied pressure might lead to overlapping and the formation of double or triple layer

To make a deposition, the chosen phase is usually the solid state. There are two deposition methods onto a solid substrate: The Langmuir–Blodgett (vertical deposition) and

the Langmuir–Schaefer (horizontal deposition), with the first being the most common (Fig. 2.3). A successful deposition needs a stable constant velocity transfer and a fine contact. When the transfer speed is slow, the orientation and packing of the single layer are preserved and stabilized during the deposition, allowing the adhesion onto the solid substrate. When the dipping speed is too fast, the monolayer is not successfully deposited. Consequently, its crystalline structure is not controlled in this limit[17].
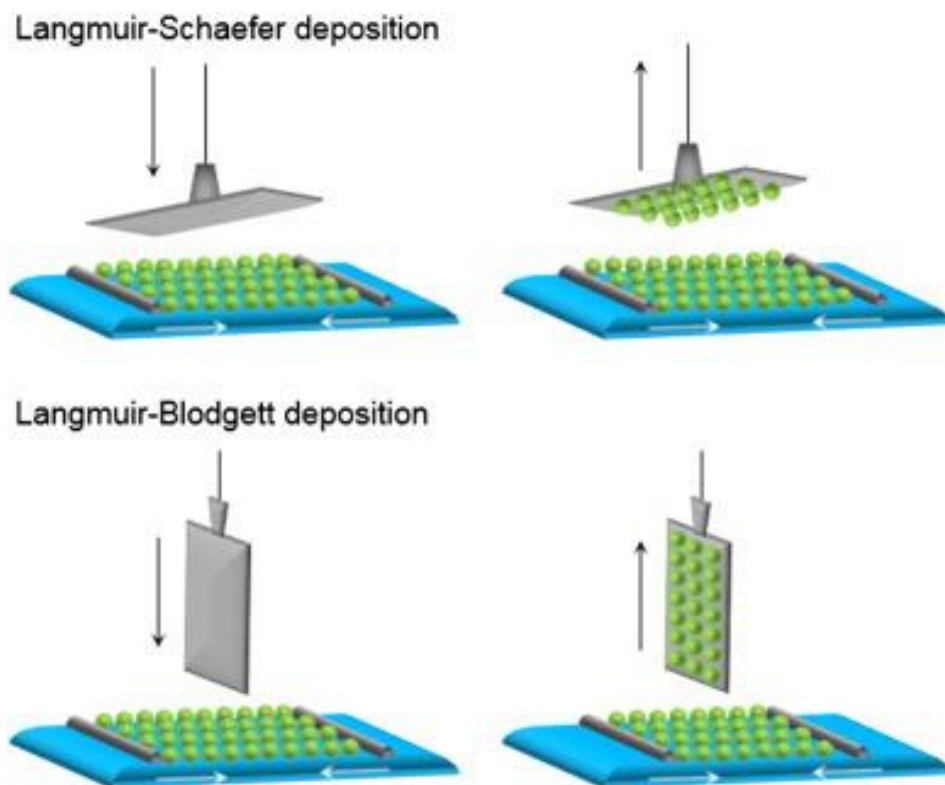
Figure 2.3: Vertical (LB) and horizontal (LS) deposition multilayer films transfer method. Figure adapted with permission from [19]

An immersion and an emersion of the solid substrate repeatedly lead to the formation of a single layer or multiple layers. There are three deposition types (Fig. 2.4). The Y-type consists of a sequence of surfactant layers with alternating hydrophobic–hydrophobic and hydrophilic–hydrophilic reactions. It is expected that this structure leads to the formation of the most stable films. Besides this method, X- and Z-type films can also be formed using only down-stroke or up-stroke moves to achieve deposition. The surfactants being used for this method consist of slightly hydrophilic head groups or polar-end alkyl chains.
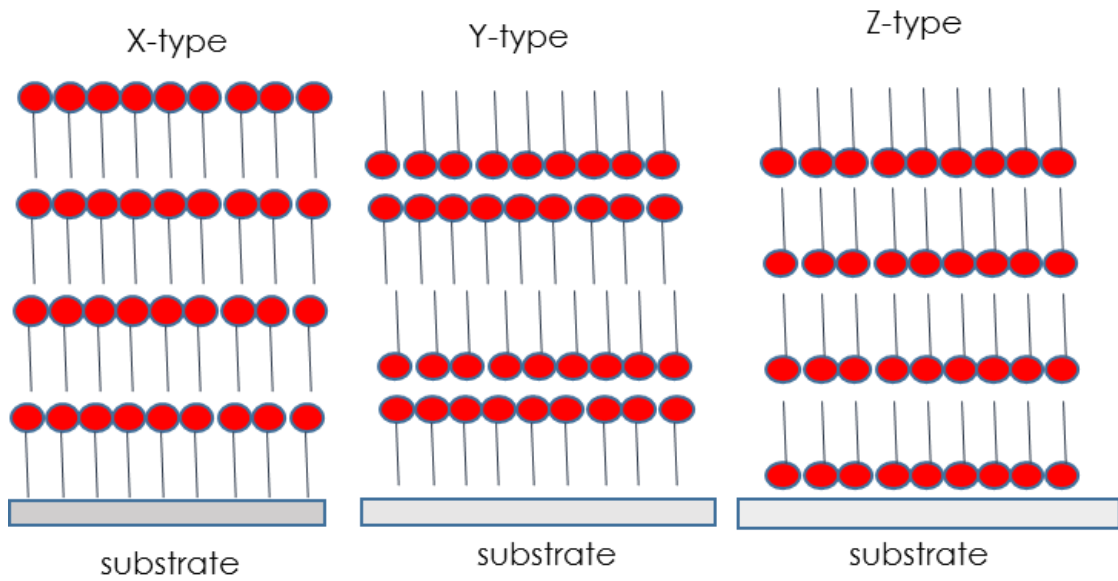
Figure 2.4: Y-, X-, and Z-type depositions of a multilayer film

In this thesis, the horizontal dipping method has been used, which is known as the Langmuir–Schaefer deposition method. It is a preferred method when dealing with rigid films. Accordingly, a rigid substrate is moved slowly at a speed of 2–4 mm/min towards the surface. This happens during the monolayer deposition and the lift-up speed is at 1–2 mm/min until the substrate no longer touches the water surface.

2.1.2 The knife-edge technique (blading)

Advancements in the synthesis and deposition of large-scale 2D nanomaterials have been a motivation for researchers to understand the ideal elementary unit for future devices. The challenge of putting these materials onto high performance devices and applications involves the production of large-area films without any loss of their uniform 2D nature[20]. There are various so-called 'knife-edge' or 'blading' techniques, including doctor blading, quartz slides, and blades as methods, while the differences between them are not defined extensively[21]. The principle of these techniques is that a solid substrate, the so-called 'knifes edge', is passing over a solution which is supplied by a syringe pump, leaving behind a uniform wet layer, where solvent evaporation can happen. This process can be executed manually or be mechanically controlled, which gives more precise control of the samples (Fig. 2.5). A difference between these blading techniques can be the exposure of the solution to the

ambient during coating, or various temperatures. The coating speed, the solution feed rate, as well as the blade–substrate distance, are key factors for the sample quality and characteristics.

Similar to other blading techniques[22-24] where a solution is coated on a substrate forced by the motion of a blade driving the droplet, in this method, a flat quartz slide plays the role of the coating blade to produce single crystalline thin films by slow solvent evaporation. The blade moves at speeds of 10 micrometres per second, while a solution droplet is provided to fill the gap between the vertical blade and the substrate. The solution droplet is continuously fed with fresh solution, so the volume stays constant. The substrate is mounted on a movable stage of a motor. A certain amount of the solution might be lost on the edges of the substrate, but the fraction is much smaller compared to other techniques (e.g. spin coating). Some of the advantages that the technique provides are large area coverage, relatively low waste of material, good uniformity, and, if monitored, precise thickness control. Additionally, it is a fast technique, although it is not so reliable when it comes to very thin films in the nanometre range.
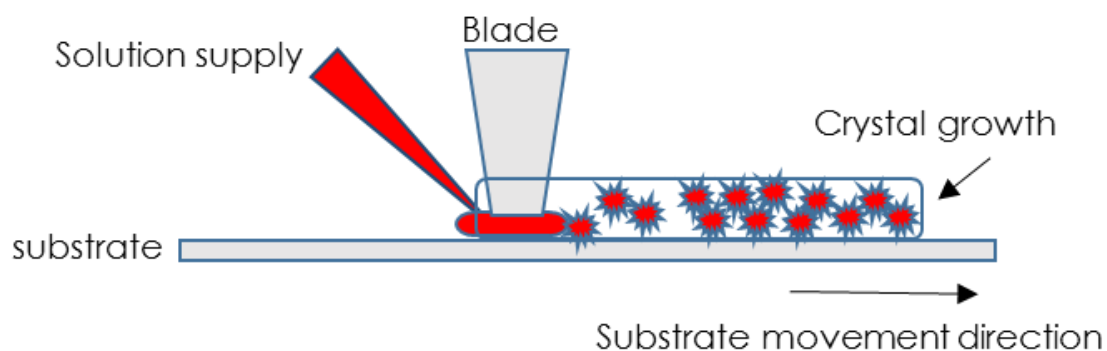
Figure 2.5: Schematic image of continuous crystal growth onto the substrate with the 'knife-edge' technique

2.1.3 Preparation of thin sections (cryo)-ultramicrotomy

Ultramicrotomy (and cryo-ultramicrotomy) are techniques used for slicing ultrathin or semi-thin sections or flat surfaces of various samples for further microscopic examination. Traditionally, ultramicrotomes are designed to cut ultrathin sections (10–100 nm) and ultrathin frozen sections (depending the mechanical properties of the material). This involves

soft materials such as biological/biomedical substances and polymers but has recently been extended to harder materials[25].

Using ultramicrotomes, the preparation of ultrathin sections is allowed, which can be further investigated via TEM and AFM. The sectioning can take place at room temperature or under cryogenic conditions depending on the mechanical properties of the material (e.g. hardness). Cryo devices are ideal for sectioning soft materials or water-soluble materials. During the procedure, both the knife and the specimen are cooled down by liquid nitrogen, where the sectioning temperature can cool down to -185 °C[26].

Both glass and diamond knives are used to obtain thin sections. Each type has advantages as well as disadvantages. The choice of the type of the knife depends on the cost and the nature of the candidate material. Glass knives are sharp-edged glass strips fabricated from special glass. Diamond knives are made of natural diamonds. A diamond knife has an angle of 45° or 35° (smaller compared to glass knives). This is an advantage because the bending and contraction of the sections can be reduced.

A microtome is a delicate and sensitive device. The apparatus consists of the microtome sample holder, which is moved towards the knife in a given and adjustable distance during every cycle (Fig. 2.6).
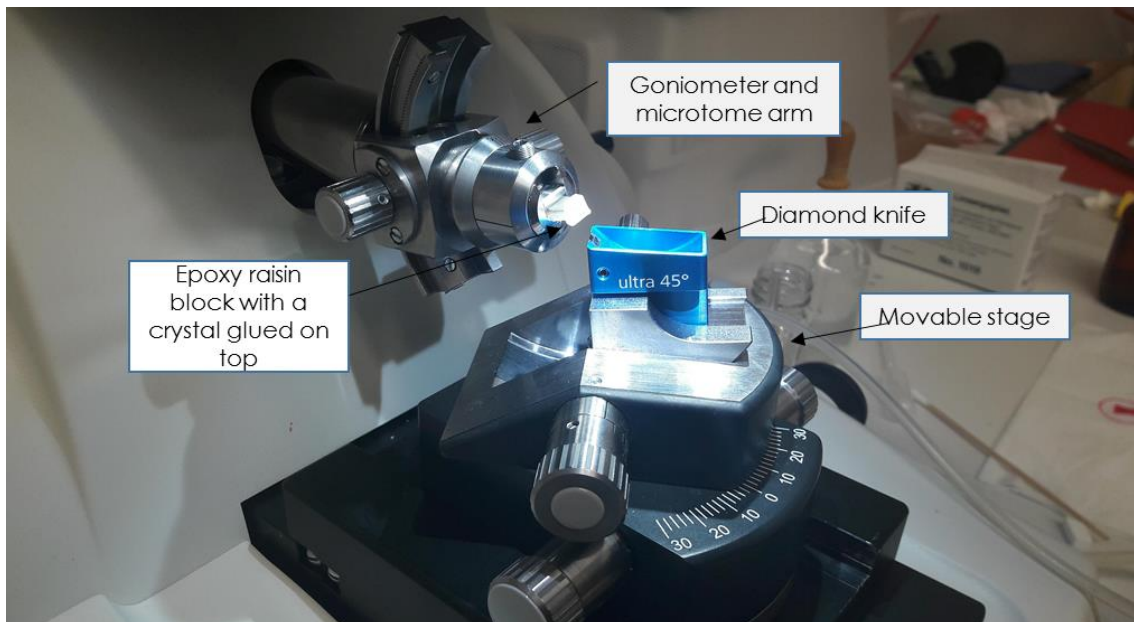
Figure 2.6: The principle of ultrathin sectioning

The sectioning is done following a vertical movement of the sample over the sharp blade of the chosen knife each time (diamond or glass). Attempting to remove the sections directly from the knife blade is tricky due to their thickness and adhesiveness. In general, the sections can float on a liquid phase on the knife boat and are thereafter collected with a loop and deposited on the chosen substrate. Although the microtome has a section-thickness control, an alternative way to determine a section thickness is from its interference colours. Upon white light reflection from the bottom and the top of the section, depending on the thickness of the section, the light will be differentially slowed down. The phase of the light will change. These wavelengths will interfere with the reflected water wavelengths and will give the sections a particular colour. The thickness of the sections can be determined using an interference card which gives a colour spectrum corresponding to a section thickness[27, 28].

Small samples, thin films, or powered materials cannot be mounted directly into the microtome specimen. In these cases, the sample should be embedded into a stable material that will not react with the sample. Materials that are most commonly used include epoxy resins, polyester resins, and methacrylates. The advantages that embedding offers include protection against any breakage and decomposition of the specimen. Another factor to be considered is the ease of sectioning, as well as the stability under high vacuum and the electron beam. A variation or existing recipes is being used based on the hardness of the epoxies[26].

After optimizing all the previous parameters, the sectioning conditions must be specified. There are wet and dry sectioning techniques, as well as ambient or cryo-temperature microtomy. We use the term 'wet sectioning' for the collection of sections performed in the presence of a floating liquid, while direct application on the knife surface is referred to as 'dry sectioning'. The choice of the technique depends on the environmental conditions. For sections prepared at room temperature, the wet method is preferred, while for cryo conditions, the dry technique seems more suitable. In most cases, room-temperature microtomy is suitable for samples that are hard enough. For very soft materials, cryo-sectioning is more appropriate because the samples can be hardened by cooling. To perform cryo-microtomy, a cryo-compartment must be available. Liquid nitrogen cools down the latter and any type of knife can be used. There are also special cryo-diamond knives suitable for this kind of sectioning.

2.1.4 Spin coating

One of the most common techniques for applying thin films onto substrates is spin coating. This method is used in a wide variety of industries and technologies because of its ability to quickly produce very uniform films within the scale from a few nanometres to a few microns in thickness[29].

In general, spin coating involves the application of a thin film smoothly across the surface of a substrate by coating a solution of a chosen material diluted in a solvent while the substrate is in rotation. It is best described as a multi-step process (Fig. 2.7). Initially, one has the deposition process where the solution is deposited on the substrate (deposition), and rotation is started at a certain acceleration (spin-up). Because of the centrifugal forces, the liquid is dispersed around horizontally and homogenously over the substrate. The reduction in the film thickness is a result of the material being dispersed outwards. At the same time, the viscosity of the material increases because of the evaporation of solvent which will stop the flow of the liquid (spin-off). Eventually, the thickness reduces slowly because of the evaporation of the solvent (evaporation)[30, 31].
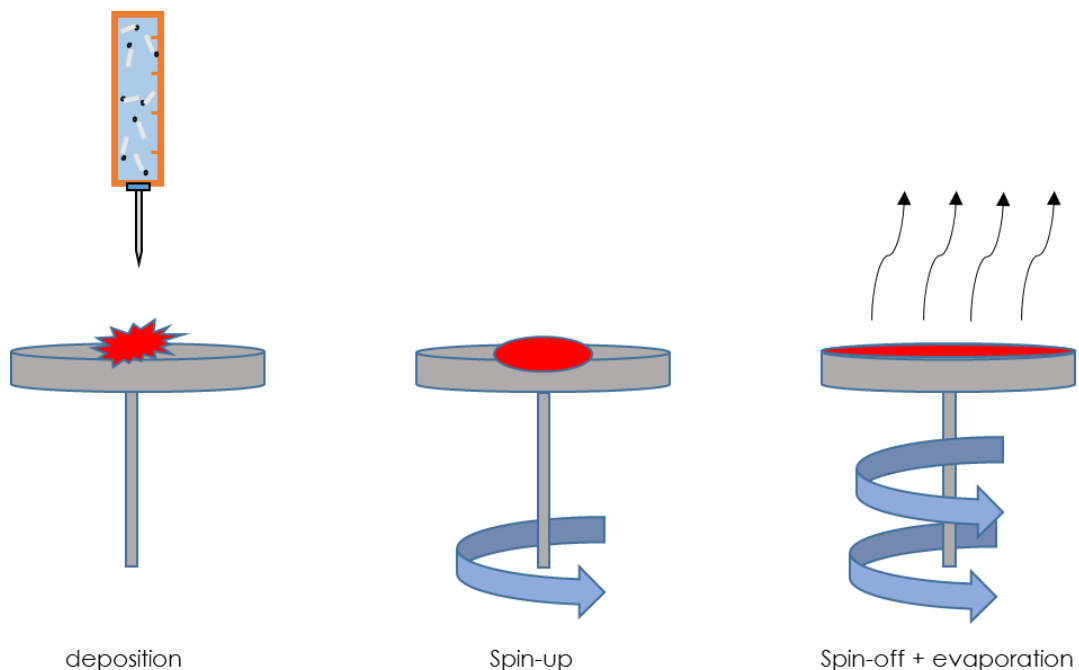
Figure 2.7: Schematic stages of the spin coating process

To estimate the thickness of a spin-coated film, Equation 2.1 holds as follows:

$$t \propto \frac{1}{\sqrt{\omega}}$$

This means that the thickness of a spin-coated film is proportional to the inverse of the spin speed squared as showed in the equation above, where t is the thickness and ω is the angular velocity. For example, if a film is spun four times, the angular speed will be half as thick. According to the equation, a spin curve can also be calculated (Fig. 2.8).
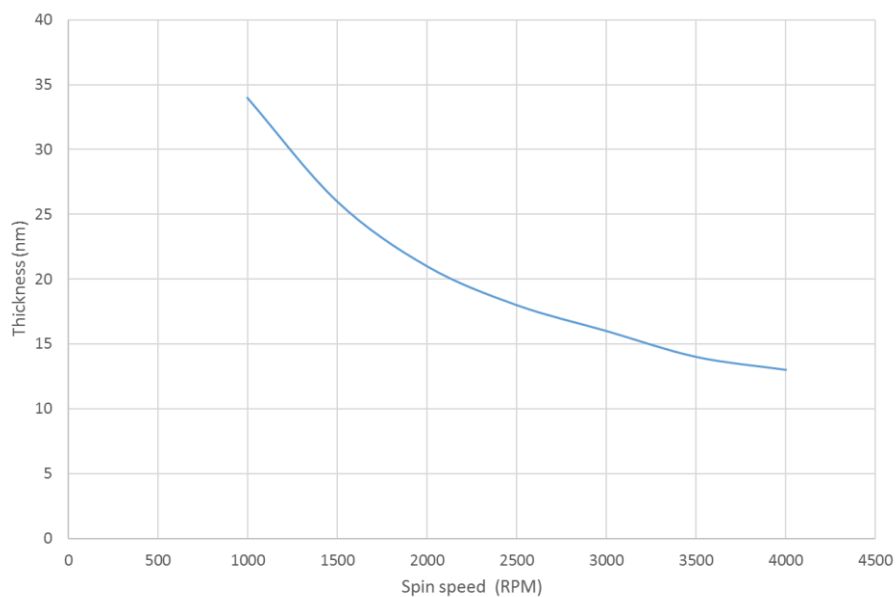
Figure 2.8: An example spin curve for a solution

The exact thickness of a film can be calculated from the material concentration and the solvent evaporation rate, and therefore the spin thickness curves are typically calculated empirically. Usually, a test film thickness is measured with techniques like AFM and surface profilometry, and the spin speed can be adjusted many times until it gives the desired film thickness[32].

One of the most crucial factors of the spin coating technique is the spin speed. The spin of the substrate (RPM) can influence the centrifugal force applied to the liquid resin, as well as the velocity and turbulence of the air above it. In general, the high spin speed step defines the final film thickness. In other words, the film thickness is a balance between the force applied to shear the fluid resin in the direction of the edge of the substrate and the drying

rate, affecting the viscosity of the resin. After the resin dries, the viscosity increases until the force of the spin process can no longer move the resin over the surface. Usually, all spin coating systems are fixed to be repeatable within ±5 RPM at all speeds[33].

For a standard spin coating technique, the aim is to keep the substrate spinning until the film is fully dry. This mostly depends on the boiling point and the vapour pressure of the solvent, as well as the humidity and the temperature at which the coating takes place. Eventually, what should be considered is which spin coating method will be used to disperse the solution—a static disperse or a dynamic disperse[29, 34, 35]. In a static disperse, the substrate is stable over the stationary, and the solution is dispersed over the whole substrate surface before the rotation begins. The spin coater then starts and is brought up to the desired speed as soon as possible. In a dynamic disperse, the substrate spinning comes first, reaching the desired speed, and the solution is then applied at the centre of the substrate. This serves to spread the solution over the substrate and can result in less waste of material, since it is not necessary to wet the entire surface of the substrate.

In conclusion, spin coating is an effective and important technique for making uniform thin films. The basic principles and parameters controlling the process are spin speed, spin time, acceleration, and fume exhaust. If these factors are considered, the spin coating process is a great tool for thin films creation.

2.2 MOF materials and experimental procedures

For the sample preparation of the metal organic frameworks, the following materials and the experimental procedures were used: Copper (II) chloride (>99.9%), copper (II) nitrate and benzene-1,3,5-tricarboxylic acid (95%) were procured from Carl Roth. Chloroform (>99.9%), acetone (>99.9%), ethanol (>99.8%), and N,N dimethylformamide (99.8%) were purchased from Sigma-Aldrich. In addition, ultrapure deionized water (18.2 MΩ) produced by a Purelab classic water purification system was used. All reagents were of analytical grade and were used without further purification.

2.2.1 LB-film creation

A commercial Langmuir Teflon trough, model 312D LS Nima Technology, with symmetric double-barrier compression, was used for the preparation and deposition of the monolayers and multilayers at ambient temperature. Before filling the trough with the subphase, it was cleaned thoroughly with chloroform using surfactant-free wipes.

An aqueous solution of $CuCl_2 \times H_2O$ (0,1M) and an aqueous solution of $[Cu(NO)_3]_2 \times 3H_2O$ (0,1M) were used as a subphase for the initial comparison experiments. Every time the surface of the subphase was carefully cleaned by mild surface-touch vacuuming. The assembly of the nanosheets was initiated by spreading a solution containing 1,3,5-Benzenetricarboxylic acid (H_3BTC) dissolved in a Dimethylformamide (DMF) solvent (0.2 mg/mL) one drop at a time with a microliter syringe onto the subphase surface. To encourage a smoother and slower reaction between the metal and the organic strut, a piece of quartz glass was partially immersed in the trough (shaped a 50° angle towards the horizontal axis) and the injection rate was kept at 10 µL/min. All the suspensions were stirred before film fabrication to ensure absolute homogeneity. Surface pressure (π-A) was monitored using a Wilhelmy paper, at a continuous pressing speed of 10 mm/min for the two barriers. After a waiting time of 20 minutes to allow solvent evaporation, the film compression was performed until maximum pressure was reached. Compression isotherms were registered at least three times to check the reproducibility of the results.

2.2.2 MOF monolayer transfer

For the deposition steps, two-dimensional (2D) arrays were fabricated at a surface pressure of 30 mN/m and were transferred onto substrates by the horizontal dipping (LS) method (the substrate surface is parallel to the subphase surface during dipping) at room temperature. The surface was slowly approached by the substrate at a speed of 0.5 mm/min, and then it was left to dry at room temperature without further treatment. To stack more layers, the 2D nanosheets on the subphase were deposited on top of the substrate following the same process. The transfer ratio can be shown in the scheme below (Fig. 2.9).
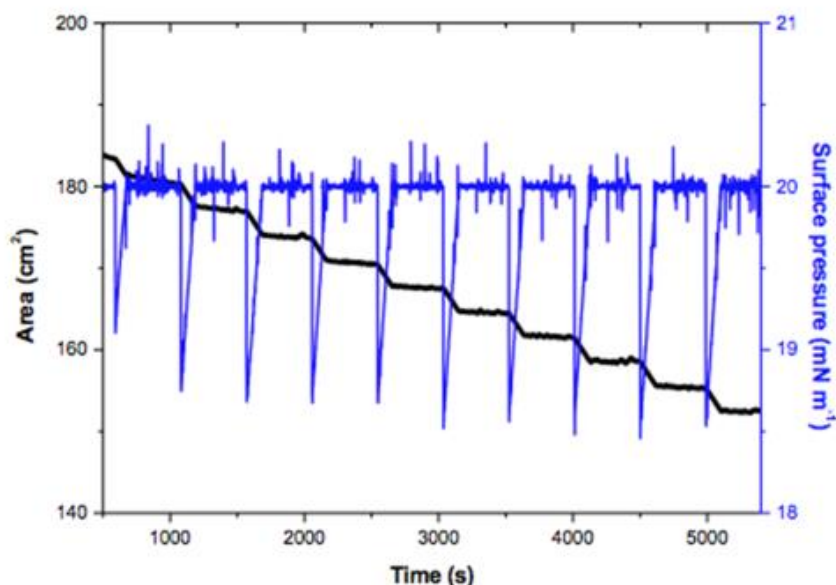
Figure 2.9: The total area of LB surface decreases linearly due to the transfer of the created layer of the air–water interface onto a solid substrate

Eventually, to ensure the successful molecule interaction at the air–water interface, the Langmuir–Blodgett films were transferred onto different substrates for further characterization.

2.2.3 MOF characterization methods

X-ray photoelectron Spectroscopy (XPS) measurements were carried out using a high resolution 2D delay line detector. A monochromatic Al K a x-ray source (photon energy 1486.6 eV, anode operating at 15 kV) was used as incident irradiation. XPS were recorded in fixed transmission mode. A band pass energy of 20 eV was chosen, resulting in an overall energy resolution better than 0.4 eV. Charging effects were compensated by using a flood gun. The binding energies were calibrated based on the graphitic carbon 1 s peak at 284.8 eV and all data collected at room temperature. The film depositions were on silicon wafer substrates with a single dip.

Same as above, for the AFM measurements, the Langmuir–Schaefer films were deposited on silicon wafer substrates (1 cm x 1 cm) via a single dip. Three measurements were taken for each sample with a scanning area 50 μm x 50 μm and 5μm x 5 μm. The resolution for scan sizes 50 μm x 50 μm and 5μm x 5 μm with the chosen value of 512 for sample/line were 97,65 nm and 9.76 nm, respectively.

For the ultraviolet-visible absorption spectroscopic measurements, the depositions were made on a quartz slide. The slides were prepared with a chloroform–ethanol treatment for 30 min in an ultrasonic bath prior to their use, and the spectra were measured at room temperature with a Shimatzu UV-2600 spectrometer.

TEM images were collected at room temperature on a JEOL JEM-2100 TEM operating at 200 kV acceleration voltage. The exposure time was limited to 100 milliseconds for diffraction images and to 1 second for the real space images. The single-layer copper-BTC (Cu-BTC, HKUST-1) films were deposited on silicon nitride TEM grids with 5 nm thin windows as well as lacey carbon support films for TEM. The diffraction pattern of amorphous silicon nitride substrates is known to show diffuse rings. The camera length calibration was performed using a polycrystalline gold sample.

2.3 Sample preparation of Dithienylethenes (DTEs)

For the sample preparation of DTEs, all isotherm studies were prepared on a Nima technology 312D LS trough. Before the preparation of the monolayers, the trough was cleaned with chloroform using surfactant-free wipes. As a subphase, pure Milli-Q water was used for all experiments. The surface of the subphase was carefully cleaned by mild surface-touch vacuuming to minimize any interruptions on the surface. Stock solutions of **1–3** (Figure 2.10) (0.15 mg/mL) were prepared in chloroform (**o** stands for the open ring form and **c** stands for the close ring form).

1o–3o   **1c–3c**

1: X = CH; R^1= CCPh; R^2= H; R^3= $(CH_2)_{12}N^+(CH_3)_3$ I^-
2: X = CH; R^1= CCPh; R^2= H; R^3= $(CH_2)_6N^+(CH_3)_3$ I^-
3: X = $N^+(CH_3)$ TfO^-; R^1= R^2= CH_3; R^3= $CH((CH_2)_{14}CH_3)(CH_2)_{15}CH_3$
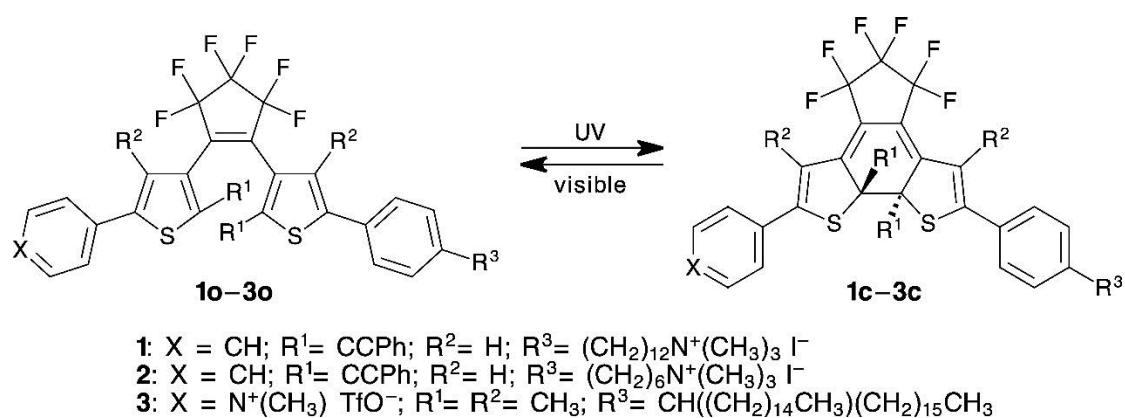
Figure 2.10: Structure formation of the examined dithienylethene photoisomers **1**-**3**. Figure adapted with permission from [36]

A quartz glass was immersed in the trough and set at an angle of about 50° with respect to the air–water interface (Fig. 2.11). This technique provides better control of the sample transfer[37]. For UV-irradiated solutions, the non-irradiated stock solutions were exposed to a UV light source (6 W UVA lamp, λ=365 nm) for 6 min. For visible irradiated solutions, the UV-irradiated stock solutions were exposed to a visible light source (53 W halogen lamp) for 2 min. A small quantity of these solutions was transferred onto the surface of the subphase with a Hamilton syringe, and the system was left to rest for 15 min before compression so that the chloroform could evaporate. The films were compressed at a rate of 10 cm²/min. For further investigation, all depositions followed the LS deposition method (horizontal deposition) at a surface pressure of 30 mN/m.

Step 1: Transfer of DTE stock solution

Step 2: Compression of DTE patches

Step 3: Formation of DTE Langmuir film

Figure 2.11: A schematic illustration of a typical DTE monolayer formation on LB trough. Figure adapted with permission from [36]

2.3.1 DTE characterization methods

Multilayer thin film depositions of **1–3** were prepared using the horizontal (LS) deposition method and the monolayers were transferred onto Eppendorf cuvette cells for the LS absorption study. The surface pressure was set to 30 mN/m and the procedure was repeated to produce LS films composed of a specific number of depositions (10, 30, and 40 deposition cycles).

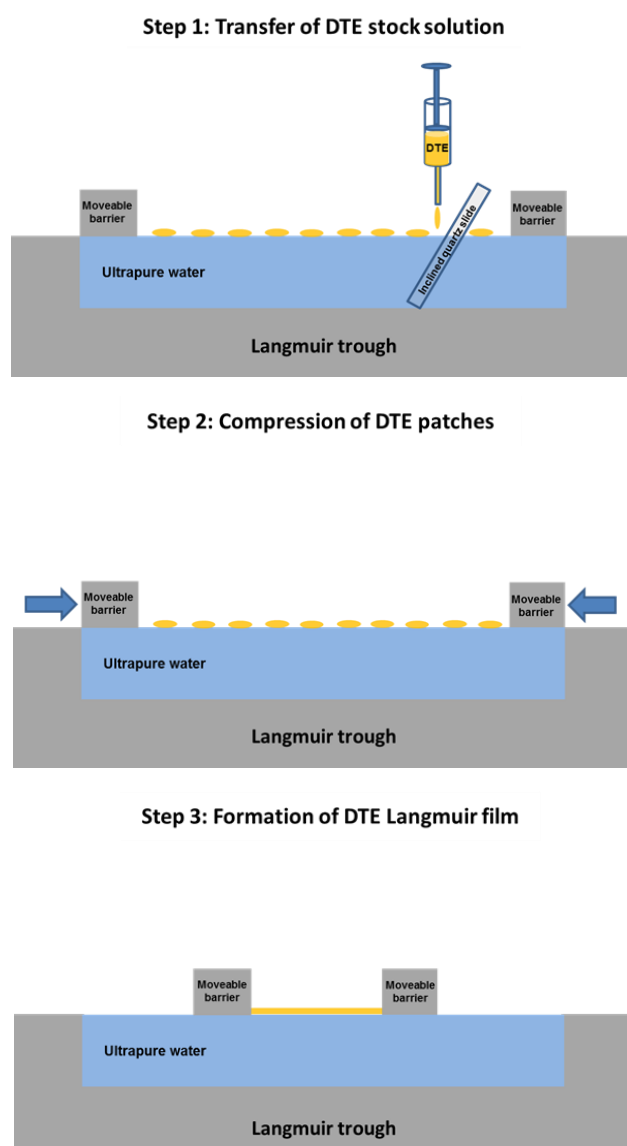Atomic force microscopy (AFM) was used to qualitatively examine the structure of these molecular assemblies. Single-layer depositions of all derivatives during all the irradiation stages were made on silicon wafers (1 cm x 1 cm) (Ultrasil Corporation) with the LS method at a standard surface pressure of 30 mN/m.

Transmission electron microscopy (TEM) studies were performed on a single-layer transferred onto silicon nitride substrates (Si_3N_4) for real space imaging and selected area diffraction (SAED) studies.

2.4 Crystallization techniques of vitamin B12

2.4.1 'knife-edge' crystallization process

For the cyanocobalamin thin film creation, a home-built knife-edge device was used. It had a motorized stage on which the substrate was placed. An adjustable stage fitted with a micrometre screw was used to control the height of the slide from the substrate. The solution was delivered by a syringe pump and controlled the droplet rate supplied under the blade edge.

To determine the optimum conditions for crystallization using the knife-edge technique, we had to test different parameters and compare the crystal quality and thickness. The essential parameters considered to control the crystallization were the speed of the blade, the solution concentration, the flow rate at which the protein solution was supplied, and finally the edge height. The thickness of the crystals is a crucial factor to estimate their crystallinity for electron diffraction. During our initial experiments, the supposed thickness was estimated approximately by eye, in accordance with the light transmission through the sample and optical absorbance. In our first 'knife-edge' crystallization attempts, microscopic slides were used as substrates, taking advantage of the surface flatness and transparency. A

microscopic slide edge was used instead of a blade edge, allowing us to keep a better control of the shape and the droplet of the solution under the edge. The concept was based on the work of Soeda et al.[23], from which we derived our apparatus (Fig. 2.12). Figure 2.13 shows different crystallization zones created for comparison on a microscope slide.
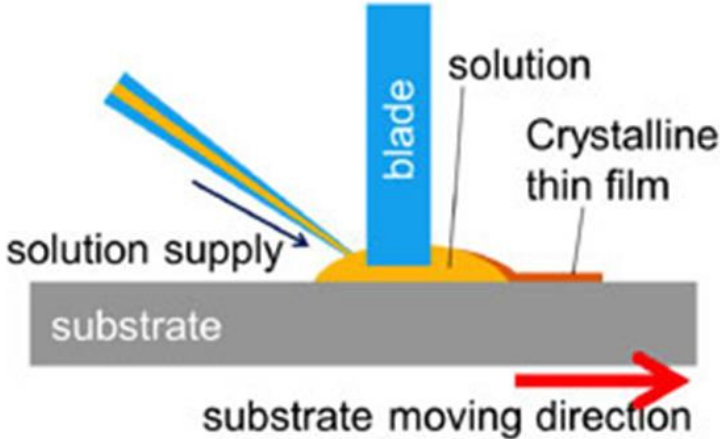

Figure 2.12: Knife-edge apparatus illustration for thin film creation. Figure adapted with permission from [23]

Figure 2.13: Crystallization on the edge with a water solution 5 mg/mL and a constant solution supply rate held at 0.03 mL/hour

The fact that faster substrate speeds result in thinner crystals was also reported in a technique called 'solution shearing'[38]. It is much like the knife-edge crystallization technique, where faster shearing rates led to thinner films with a smaller average size of deposited crystals. Similarly, the crystals we obtained turned out to be of reduced size compared to those obtained from slow substrate rates. An explanation could be that slower stage speeds result in the solution being deposited as a thinner layer, while the solvent evaporation yields the crystals. This would be expected to lead to reduced crystal size because there is less solvent for the crystal formation. The pyramid-like shapes shown in figure 2.13 (more detailed in Table 5.1) and noticed in the knife-edge crystallization were observed in solution shearing as well[38].

The nucleation happens where the curvature of the contact lines has the most concentration solution. This could be explained as a pattern left by a pond of a full droplet liquid after it evaporates, as a coffee droplet would do. As an example, the edges of a coffee drop spilled on a table or a piece of paper are pinned to the surface. This means that when the water evaporates, the droplet cannot shrink in the perimeter but flattens out. The flattening motion then pushes water and anything attached to it, like coffee particles, to its edges. When the drop is fully evaporated is the point at which most of the particles have reached the edge and are deposited on the surface, forming a dark ring. This is the so-called 'coffee-ring effect'[39]. The knife-edge technique ends the formation of a circular typical droplet, but an influence line still exists and is affected by the coffee ring effect. Instead, the 'rings' are formed parallel to the edges of the slide.

2.4.2 Sample transfer after the crystallization procedure on copper foil

After the crystallization process, another problem is the substrate transfer. Therefore, the idea to create a crystalline film on a movable substrate looked appealing. For this purpose, a copper foil sheet (0.025 mm thick) was folded around a glass slide and on top of the foil a PMMA layer (5% w/v in toluene) was spin-coated. To minimize the thickness of the final film, the spin-coated PMMA layer was 100 nm thick. Thereafter, the knife-edge crystallization took place using the optimal parameters, and another PMMA layer was spin-coated (1000 rpm for 5 min) on top after the crystallization procedure was accomplished[34, 35, 40]. The aim was to protect the B_{12} crystals within the PMMA sandwich and remove the copper foil by etching it (using a strong etching $FeCl_3$ solution (Sigma-Aldrich)).
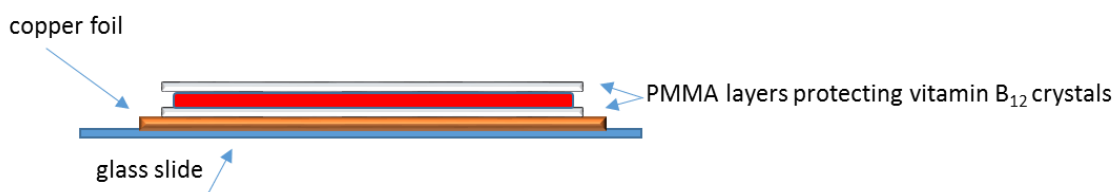
Figure 2.14: a schematic representation of the PMMA/B$_{12}$ 'sandwiched' film created on top of a copper foil before the copper etching procedure

The next step was to dispose the copper and place the crystallized film onto different substrates for further characterization. Due to the big area coverage, the transfer procedure had to be done methodically. Figure 2.15 shows a schematic representation of the created film on top of the substrate. Under the microscope the areas of interest were isolated by cutting the copper foil into small pieces with a diamond cutter to make the etching procedure straightforward.
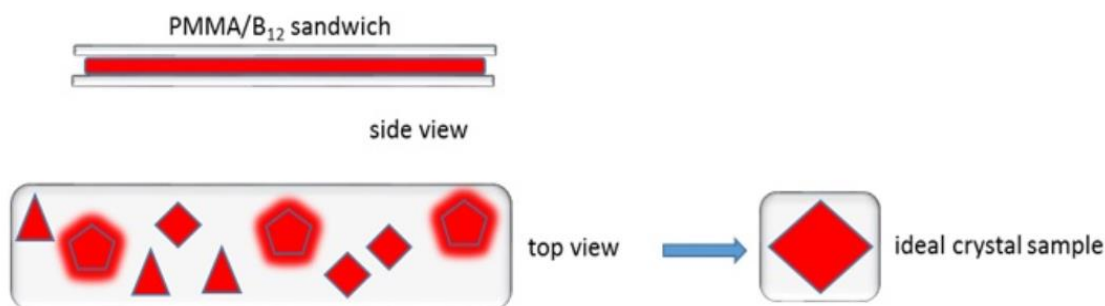
Figure 2.15: Schematic illustration of the ideal created film. The vitamin B$_{12}$ crystals are depicted in red colour and the PMMA layer with grey

All pieces were placed carefully in a strong FeCl$_3$ etching solution for about 30 min. The copper was directly in contact with the etchant and therefore were corroded. The etching started from the corners and slowly moved into the centre of each section leaving the PMMA membrane floating. After inspecting the samples for any copper traces left, the cleaning procedure was the next step. Distilled water added drop by drop into the etching solution to dilute it. The reason was to avoid contaminating the crystals and clean them before the transfer. The last step was the crystal deposition onto different substrates.

2.4.3 LB monolayers studies of vitamin B$_{12}$

For the LB monolayer studies, distilled and deionized water was used as a subphase surface in the monolayer experiment (using a Milli-Q Purelab Classic). All reactants (99+%, Sigma-Aldrich) and organic solvents were used without any further purification. Dipalmitoyphosphatidycholine (DPPC) and vitamin B$_{12}$ (cyanocobalamin) (>98%), (>96%) were obtained from Sigma-Aldrich and Carl Roth, respectively, and were used without any further purification. Prior to the preparation of monolayer films, the trough was thoroughly cleaned with chloroform and filled with ultrapure water. As a spreading solvent, a benzene/ethanol (80/20 v/v) solution containing 10 mg of vitamin B$_{12}$ and 5 mg of a DPPC lipid was used (**1**). The trough barriers were wide open at 400 mm, and 100 µL of the mixed solution was spread. The barrier compression started about 10 min after the spreading at a rate of 10 mm^2/s. The subphase was kept at ambient temperature and the surface pressure was measured by a Wilhelmy plate at a surface pressure of 25 mN/m. The Wilhelmy plate had been calibrated with the transition pressure of an arachidic acid (CH$_3$(CH$_2$)$_{18}$COOH) monolayer, and the isotherms were recorded at least 3 times to ensure the reproducibility.

A pure solution had a benzene/ethanol (80/20 v/v) mixture, and 5 mg of the DPPC (**2**) lipid was also spread on the pure water subphase for comparison. The same waiting time and barrier speed were maintained to record the isotherm.

2.5 Characterization methods

2.5.1 Atomic force microscopy (AFM)

The atomic force microscope belongs to the category of scanning probe microscopes invented in the late 1980s. AFM generates images almost at the level of the atomic resolution, by measuring the surface of the sample[41-43]. In an AFM setup, a laser beam is pointed onto the back side of a cantilever and reflected to a quadrant photo detector (Fig. 2.16).
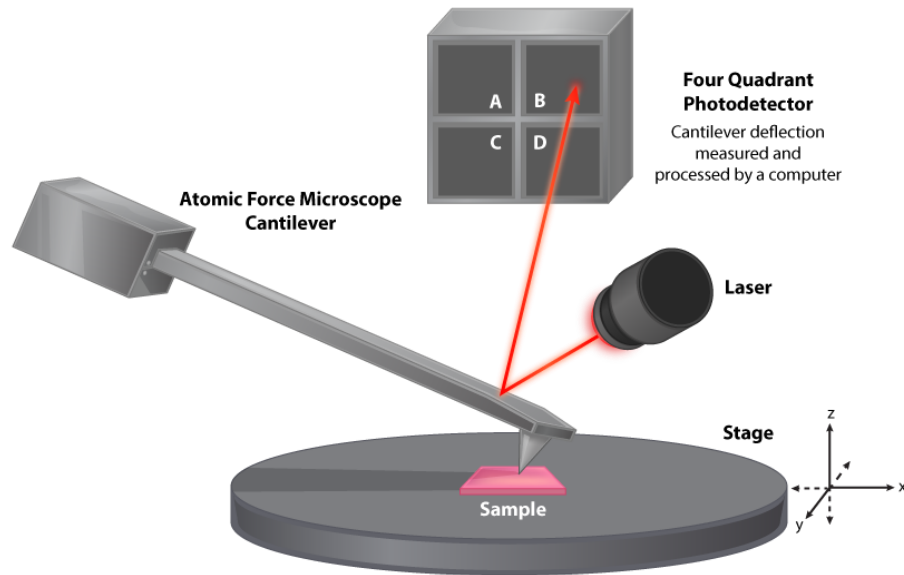
Figure 2.16: A schematic illustration of an Atomic force microscope. Figure adapted with permission from [44]

The principle is that the sample is scanned by a tip mounted to a cantilever spring. During the scanning process, the force between the tip and the sample is measured by monitoring the deflection of the cantilever. A topographic image of the sample is collected by plotting the cantilever deflection in relation to its position on the sample. Another way is by plotting the height position of the translation stage. This height is controlled by a feedback loop that maintains a continuous force between the tip and the sample.

Many AFM modes have been developed for special purposes during the last decades. Some of the most commonly used techniques are the contact mode, non-contact mode, and tapping mode. They are characterized according to different operating force ranges. Contact and tapping modes are the two most widely used AFM modes when it comes to ambient conditions. The non-contact mode usually applies in vacuum. In this thesis, only the contact mode and the tapping mode were used.

In the contact mode, the AFM tip is in actual contact with the sample surface under repulsive force. During the scan of a topographic image of a sample, the height position of the translation stage, which controls the up–down movement of the AFM tip, is controlled by a feedback loop. This loop supplies a constant force between the tip and the sample. When it comes to soft samples, the contact mode is the ideal tool because of its ability to choose between softer cantilevers. Owing to the contact mode scanning, we can get a topological

map of the surface as well as a friction image. The latter can be applied as a chemical force microscopy providing nanoscale information about the chemical groups on a sample surface, determining the friction, adhesion, and compliance of a surface at a molecular scale[45-47].

The tapping mode is referred to as the mode solving the problem of having high lateral forces among the surface and the cantilever, whereas the induced lateral resolution can be solved by having the tip touching the surface only for a short time. At the same time, it avoids the issue of lateral forces and drags across the surface. A typical tapping mode operation is carried out by using an amplitude modulation detection with a lock-in amplifier[48] (Fig. 2.17). In the tapping mode, direct forces are not measured.
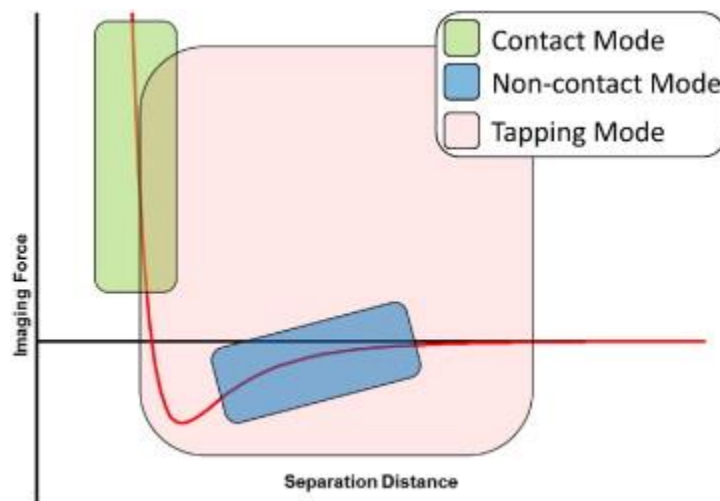
Figure 2.17: Representation of the force regimes under which the three basic AFM imaging modes occur: contact mode occurs in the repulsive regime where hard contact is maintained between the imaging tip and the sample, intermittent contact repeatedly engages and disengages with the sample surface, but maintaining lower interaction forces with the surface; non-contact mode operates in the attractive regime, feeling the attractive van der Waals forces between tip and sample, enabling profiling of the surface with minimal surface deformations. Adapted with permission from reference[49].

2.5.2 Transmission electron microscopy (TEM) and cryo-EM

Transmission electron microscopy (TEM) images electrons which are transmitted through a sample. An electron gun provides the electrons, requiring a high accelerating voltage (typically 80–300 keV), and since electrons interact strongly with matter, there is a

requirement that the sample to be tested should be within the nanometre range (< 100–200 nm). TEM is a powerful tool for material science and provides a very high resolution, being able to image micro- and nano-crystallites, voids, dislocations, grain boundaries, and even single rows of atoms. It can perform chemical spectral analysis within the nanometre scale resolution, and analyse the quality, shape, size, and density of quantum wells, wires, and dots.

The basic principles on which TEM operates are the same as the light microscope, using electrons instead of light. Since the wavelength of electrons is smaller than that of light, the optimum resolution we can get from TEM images can be in the Angstrom range. Figure 2.18 depicts a cross section of a typical TEM instrument[50, 51].
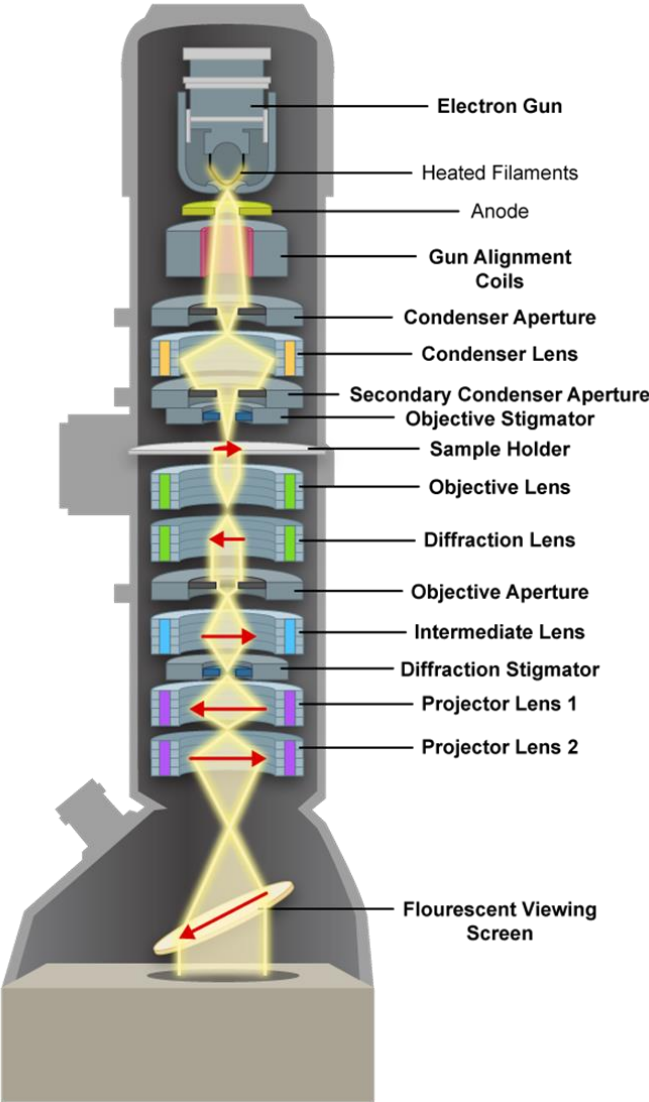

Figure 2.18: Transmission electron microscope. Figure adapted with permission from [44]

During the illumination beam shaping, the electrons coming from the gun are forced into a small, thin, coherent beam passing through condenser lenses. The beam is then scattered according to the sample thickness and scattering potential of the atoms (depending on Z value). Also, there are phase changes in the electron wave, which can produce interference contrasts in the image. The transmitted electron signal is magnified by the objective lens and projector lens system and is captured by a camera such as a scintillator-coupled CMOS detector. Objective apertures can be used to increase the contrast by blocking out electrons that are scattered to high angles where the electron scattering is higher in the case of the scattering/phase contrast. Therefore, darker regions are produced where there is negative interference caused by scattered and unscattered electron waves[51, 52].

A diffraction pattern can be generated by adjusting the magnetic lenses. When the crystalline sample is thin, the produced image forms a pattern with dots in case of a single crystal, a ring series for polycrystalline material, or a continuous radial distribution when there are amorphous solid materials. For a single crystal, the diffraction pattern depends on the specimen orientation and the sample structure. The diffraction pattern can provide information about the space group symmetries within the crystal and the crystal's orientation to the beam path. This information can be obtained according to the position where the diffraction spots and the image symmetries appear.

TEM samples must be thin enough to transmit enough electrons while avoiding excessive multiple scattering. For this reason, the sample preparation is especially important for the TEM analysis. Some materials such as biomolecules are not compatible with the high vacuum conditions and suffer radiation damage from interaction with the electron beam.

For these samples, cryo-electron microscopy (cryo-EM) is used, employing vitrified samples held at cryogenic temperatures in the column. The cryogenic conditions preserve the specimen in the vacuum and reduce radiation damage. Nonetheless, to obtain high resolution, low electron doses and high-sensitivity detectors are needed.

2.5.3 Ultraviolet-visible absorption spectrometry (Uv-vis)

Every chemical compound can absorb, transmit, or reflect light (electromagnetic radiation) up to a certain range of wavelengths. Spectrometry is a measurement of how much a chemical substance absorbs or transmits, and the spectrometer measures the amount of the light absorbed after it passes through a sample (usually a solution). A UV-visible spectrometer

uses light over the ultraviolet range (185–400 nm) and a visible range (400–700 nm) of electromagnetic radiation spectrum[53].

Ultra-violet (UV) spectroscopy is a key tool in analytical chemistry. Spectroscopy is related to the interaction of light with matter. When a chemical compound absorbs visible or ultraviolet light, a specific spectrum is transmitted. The description of the light transmitted through the sample can be described by the Beer–Lambert law, which is expressed through Equation 2.2 as follows:

$$A = \log\left(\frac{Io}{I}\right) = ECI$$

Here, A is the absorbance, I_o is the intensity of light over a sample cell, I is the intensity of light leaving the sample cell, E is the molar absorptivity coefficient of the material, C is the concentration of the absorbing species, and l is the length through the sample cell[54].
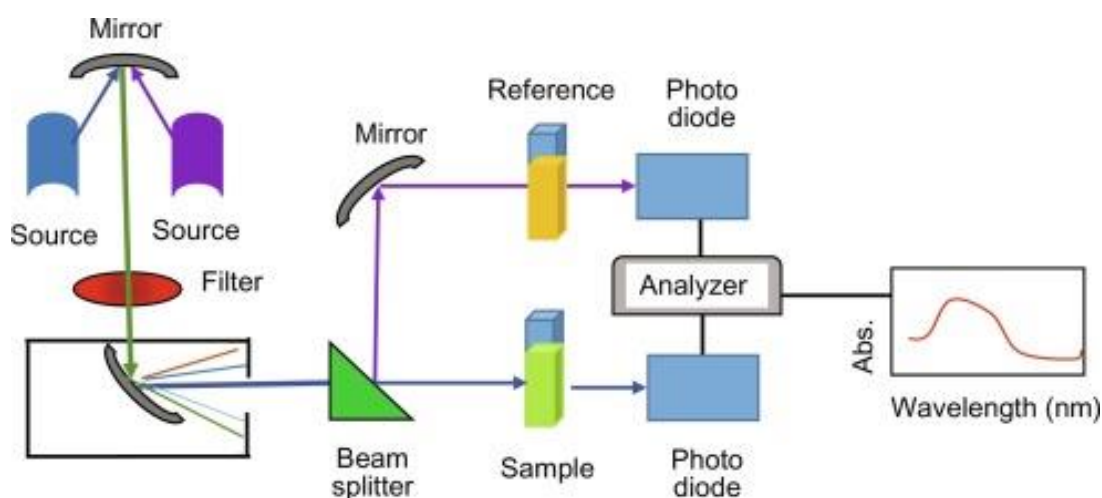
Figure 2.19: A schematic illustration of UV-visible spectrometer. Figure adapted with permission from [55]

The samples used for UV-vis spectrometry are usually liquids, and in some cases gases or even solids. The sample holder is a transparent cell (cuvette). Cuvettes have a rectangular shape with an internal width of 1 cm (the path length in the Beer–Lambert law). The element of the sample container should allow radiation to pass over the spectral region of importance. Most used cuvettes are made of quartz glass or high-quality fused silica, because they are transparent over the UV, visible, and near infrared regions. The plastic and glass cuvettes

absorb in the UV as well, but their use is not so common when it comes to visible wavelengths[53, 54, 56].

2.5.4 X-ray photoelectron spectroscopy (XPS)

X-ray photoelectron spectroscopy (XPS), known as well as electron spectroscopy for chemical analysis (ESCA), is a technique for analysing the surface chemistry of a material. This technique is used to analyse the elements making up the sample surface, its composition, and chemical bonding state (Fig. 2.20).
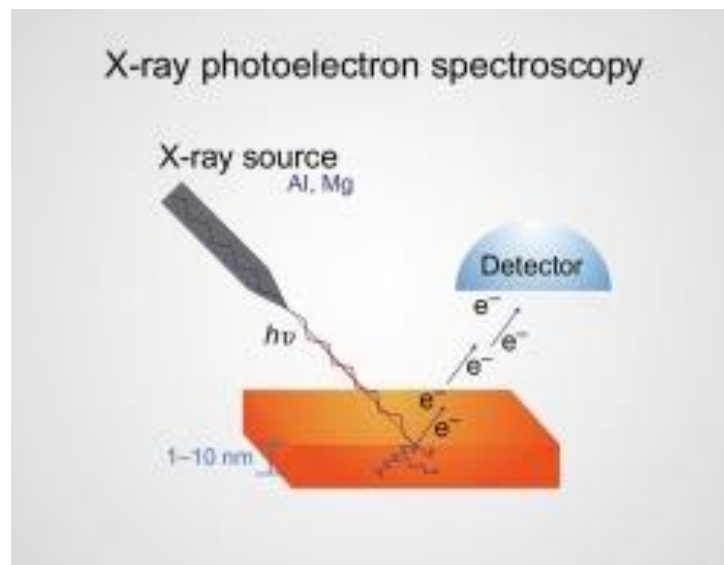

Figure 2.20: Depiction of a monochromatic XPS system. Figure adapted with permission from [57]

A surface layer, depending on the material, can be up to three atomic layers thick (~1 nm). Layers that are about 10 nm are considered ultra-thin films, while layers with a thickness of about 1 μm are thin films. The remaining solid form is referred to as bulk material.

In XPS, the signal is generated by a special form of photoemission—electron ejection from a core level by an x-ray photon energy hv. The energy of the photo-emitted electrons is analysed using the electron spectrometer. The kinetic energy (E_k) of the electron is the quantity measured by the spectrometer, and the binding energy of the electron (E_B) is the parameter that identifies the electron as originating from a specific atomic energy level of a parent element. The relation between the parameters is shown in Equation 2.3:

$$E_B = hv - E_K - W$$

where hv is the photon energy, E_K is the kinetic energy of the electron, and W is the spectrometer work function[58]. This equation is a conservative version of energy equation. The work function term is an adjustable instrumental correction factor accounting for the few eV of kinetic energy given by a photoelectron, while it is absorbed by the instrument detector[58].

The photoemission process is shown below (Fig. 2.21) where an electron is ejected from an atom. The photoelectron spectrum will reproduce the electronic structure of an element precisely because all electrons with less binding energy than the photon will be featured in the spectrum. In Figure 2.22, the XPS spectrum of lead is imposed on a representation of the electron orbitals.
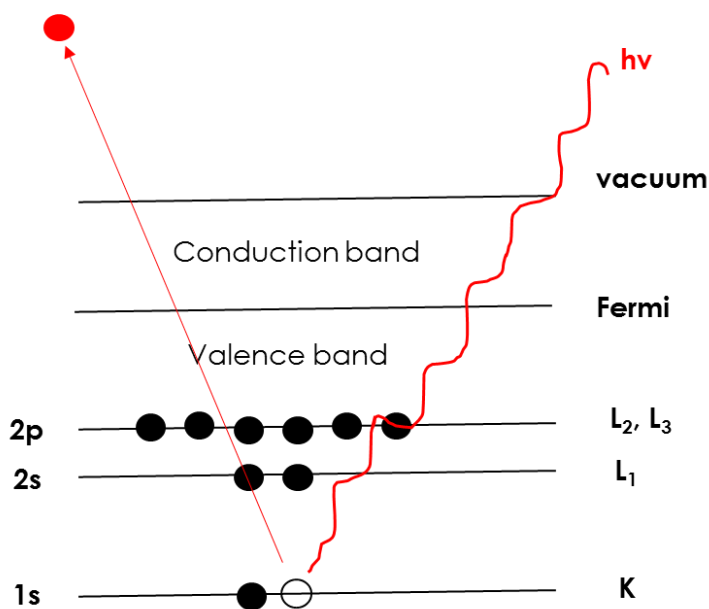

Figure 2.21: A diagram of the XPS process, representing the photoionization of an atom by the ejection of a 1s electron

The excited electrons that can escape without energy loss assist to the characteristic spectrum peaks. The ones that undergo inelastic scattering and undergo energy loss contribute to the background of the spectrum.

3. The challenge of a metal organic framework

3.1 A brief introduction

Metal organic frameworks (MOFs) are molecular structures that can be constructed through the assembly of two essential building blocks. These can be different metal clusters/ions (inorganic units) and organic ligands/struts. As shown in Figure 3.1, metal nodes act as connecting points, and organic ligands connect the molecules forming a 3D network. The resulting high porosity and large surface areas of the MOFs are ideal for trapping guest molecules and even 'forcing' them to participate in chemical reactions[59-61]. The flexibility of their composition, properties, and architecture had a major impact on the fields of catalysis[62-65], gas separation[60, 66-68], optoelectronics[69], drug delivery[64, 67, 70, 71], sensors[69, 72, 73], electrochemistry[74-77], and gas storage[60, 78-80].

Metal Ions or Clusters + Organic Linkers or Struts = Metal-Organic Framework (MOF)
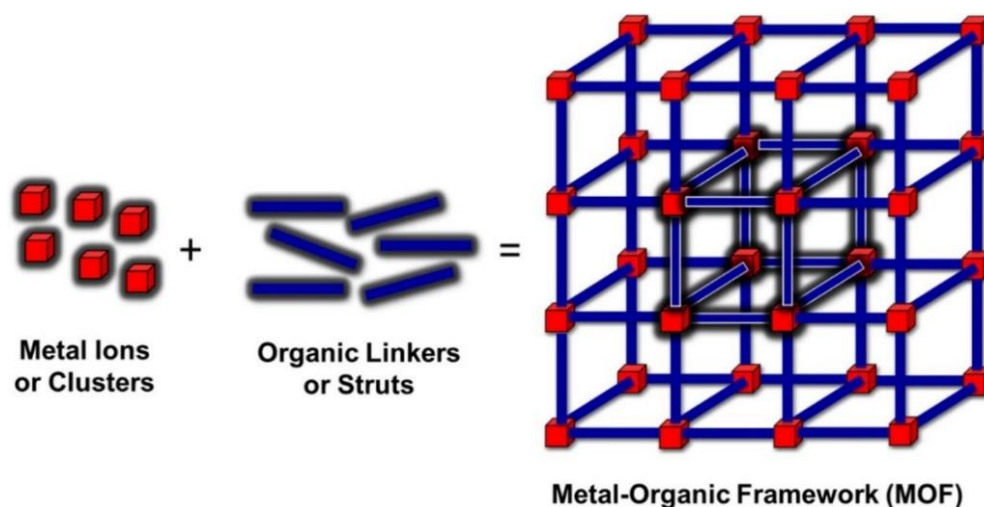
Figure 3.1: Representation of a metal–organic framework (MOF) showing organic linkers and metal ions. Figure adapted with permission form [81].

The work described in this chapter is focused on the creation of a low-dimensional system for atomically resolved dynamic studies. Some MOFs exhibit extensive flexibility when exposed to a certain type of guest molecules and show reversible structural dynamics following absorption/desorption processes (breathing effects)[82]. Furthermore, the structural dynamics of MOFs can be triggered by the insertion or removal of solvent molecules[82]. For example, a well-known phenomenon is the extensive structural response

on water insertion and removal. The removal of water from metal sources leads to changes from closed-pore to large-pore form, which involves an atomic displacement[83]. Furthermore, their crystalline architectures make them perfect candidates for molecular movies.

3.2 Synthesis of Cu-BTC surface-mounted metal–organic framework (SURMOF)
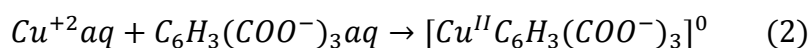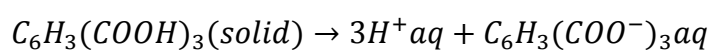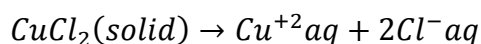
The term 'surface-anchored metal–organic frameworks' (SURMOFs) refers to MOF thin films which are homogenous and perfectly aligned in at least one direction of the growth. Their thickness is normally in the nanometre range, and the orientation of the growth substrates can be controlled by functionalizing the applicable substrate. In this project, the aim was to combine the MOF crystallinity and the LB/LS deposition technique to create a large-area crystalline organic thin film that could be transferred on a substrate. A set of imaging and spectroscopic tools would reveal the film information such as thickness, homogeneity, and crystallinity. The prior characterization is critical to evaluate the sample suitability for femtosecond electron diffraction studies.

To reduce the MOF's dimensionality and bring it into the 2D world, a reliable protocol for producing free-standing large area sheets had to be developed. Consequently, it was assumed that using any organic ligand (trimesic acid, oxalic acid) of planar geometry would lead to a well-defined planar MOF structure, considered as a 2D monolayer. Therefore, metal source copper chloride ($CuCl_2$ x $2H_2O$) was combined with trimesic acid ($C_6H_3(COOH)_3$ or H_3BTC). In a simple approach, it might be expected that the obtained MOF should produce structures with atoms within the 2D in-plane format, and thereby maintain the same square setup as is the case for a 3D MOF network. However, it needs also to be considered that there might be some out-of-plane buckling where the planar square crystal scenario maximizes the metal–metal distance. This is consistent with the repulsive coulombic forces between the charged metal ions. Additionally, the organic acid used as linker in the present work is known to take planar geometries in crystal structures. The synthesis of the Cu-BTC MOFs designed in this study should follow a classic Lewis acid-base reaction via the slow mixing of the two solutions:

$$q[R(COO^-)_x]^{p-}(Lewis\ base) + pA^{q+}aq(Lewis\ acid) \rightarrow \{A_p[R(COO^-)_x]^0_q(solid) \quad (1)$$
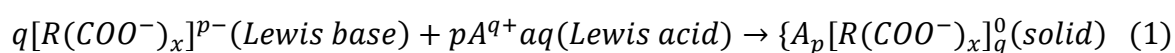
Equation 3.1 was applied, hypothesizing that the planar geometry of H$_3$BTC would force the formed solid to maintain the same planar structure. Accordingly, R(COOH)$_X$ in Equation 3.1 was chosen to be H$_3$BTC and (A) was chosen to be copper (II), so that the metal would occupy the positions which were previously occupied by the acidic hydrogen atoms. Thus, we expect the final reaction:

$$CuCl_2(solid) \rightarrow Cu^{+2}aq + 2Cl^-aq$$

$$C_6H_3(COOH)_3(solid) \rightarrow 3H^+aq + C_6H_3(COO^-)_3aq$$

$$Cu^{+2}aq + C_6H_3(COO^-)_3aq \rightarrow [Cu^{II}C_6H_3(COO^-)_3]^0 \qquad (2)$$

Based on this, the structure of the 2D-MOF can be anticipated as follows: the Cu$_3$(BTC)$_2$ MOF (also labelled Cu-BTC), which exhibits a cubic framework structure, has an open 3D pore system and is one of the archetypal stable MOFs obtained by linking copper(II) paddlewheel dimers and 1,3,5-benzenetricarboxylic acid ligands[84]. Cu-BTC has Lewis acid Cu sites, which are available for molecules. Some major advantages of the LB method are the flat and uniform surface on a large length scale, the availability of the water subphase as a pool of reagents, the straightforward preparation and facile isolation of single sheets by transfer to supports and the ease of performing synthesis at ambient temperatures. Prior to the Cu-SURMOF fabrication, many preliminary tests were done until we met the final conditions. Other than the synthesis routes, the process parameters such as type of solvent, reaction times, and temperature can strongly influence the crystal growth rates. As already mentioned, additives were used to efficiently adjust the crystal growth[85]. With the proposed research, it is expected to grow large-area crystalline thin films, fully characterized with a set of imaging and spectroscopic tools. This chemical information is critical to completely understand the film dynamics.

3.3 Air-liquid interface studies

To the extent of our knowledge, we chose both CuCl$_2$ and Cu(NO$_3$)$_2$ as metal sources. Copper nitrate is the most common chemical used for Cu-BTC synthesis, and copper chloride was chosen for chemical synthesis/reaction comparison. Some experimental trials and data comparison showed that copper chloride reacted better. Trimesic acid (H$_3$BTC) was the organic ligand.

Various solvent systems were tested to understand their reaction on MOF film formation. Batches of the ligand dissolved in four different solvents were prepared. The solvent comparison took place on a pure water subphase. The obtained π-A isotherms (Fig. 3.2) show the differences between the possible molecular packing on the surface and the possible dissolution according to the different combinations for each case.
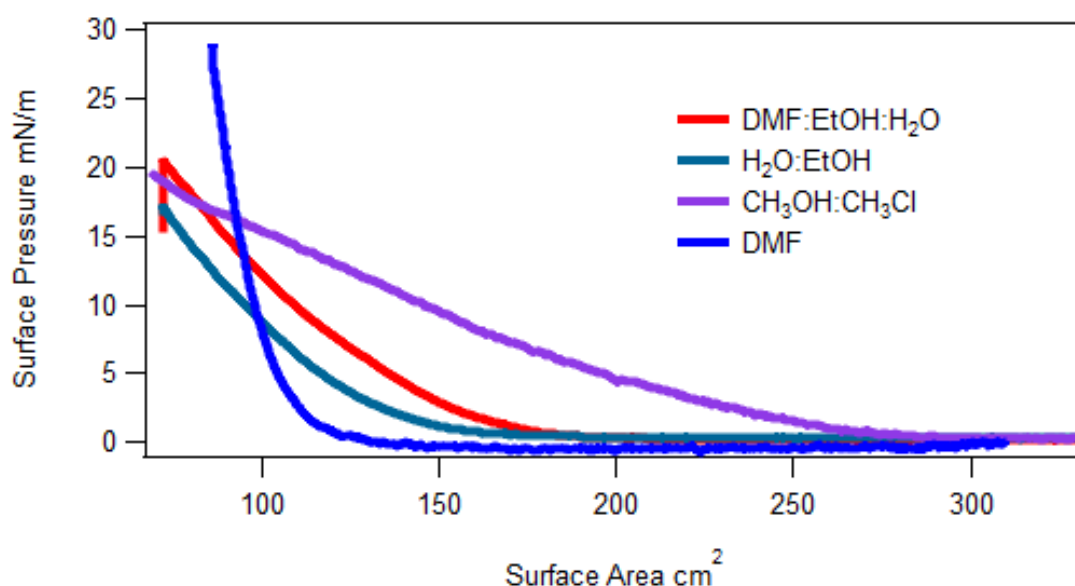

Figure 3.2: Surface pressure-area (π-A) isotherms to determine the proper solvent solution combination for the chosen organic ligand (BTC)

A wise choice of reaction solvents is crucial for the synthesis of MOFs. This is because they have a direct or indirect impact on the coordination behaviour between the metal and the ligand[86]. Even though there are still many unanswered questions regarding the solvent choice for each synthesis, a few examples of MOF syntheses show that each solvent plays a role in regulating the formation of different coordination environments[86]. For these experiments, four different combinations were tested to find the one giving better molecular packing according to the isotherms, as well as exhibiting proper reactions with the metal

sources. Additionally, the appropriate selection of solvent for spreading the solution is not to be neglected, because it should not be mixed with the subphase solution and is highly volatile. The effect of the solvent combination on the formation of the floating film can be seen over the isotherms. The combinations to dissolve the H_3BTC molecules were a solution of DMF:EtOH:H_2O with a mixing ratio of 2:2:4 (v/v). Some other tested combinations included H_2O:EtOH with a mixing ratio 1:1 (v/v), CH_3OH:CH_3Cl with a mixing ratio 3:1 (v/v), and pure DMF. A larger surface area indicates the formation of an early layer existence. On the other hand, a smaller surface area means that the molecules are closely packed, and the molecules show a higher degree of organization. To assure the consistency of the results, the same isotherms were repeated at least three times. A pure DMF solution was sufficient as there was no film assembly with the other solutions or the formation of crystalline films was of low quality. After defining these parameters, a typical fabrication process of large area sheets followed.

When compression begins, the surface pressure is almost zero in large areas, because there is no molecule interaction on the surface. Upon more compression, the surface pressure rises significantly and reaches 60 mN/m.
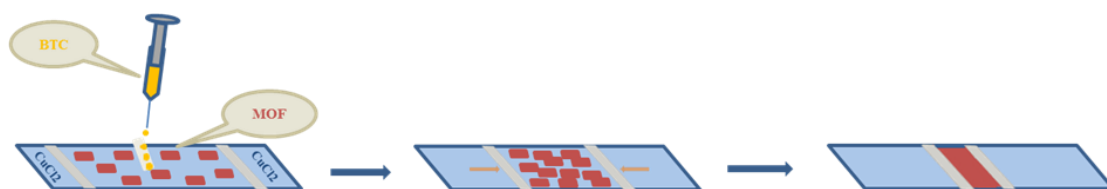
Figure 3.3: A model illustration of the Langmuir–Blodgett film network process. Figure adapted with permission form [87]

The same solution spread onto a pure water subphase, with the same speed during the barrier's compression, was used for comparison. For the pure water subphase, the smaller molecular area indicates that the H_3BTC molecules are packed more closely, though without confirming if their orientation is horizontal or vertical on the water surface (Fig. 3.4).

Figure 3.4: Surface pressure-area (π-A) isotherms for the Cu-BTC nanosheet and for the H_3BTC building unit collected on pure water as a subphase
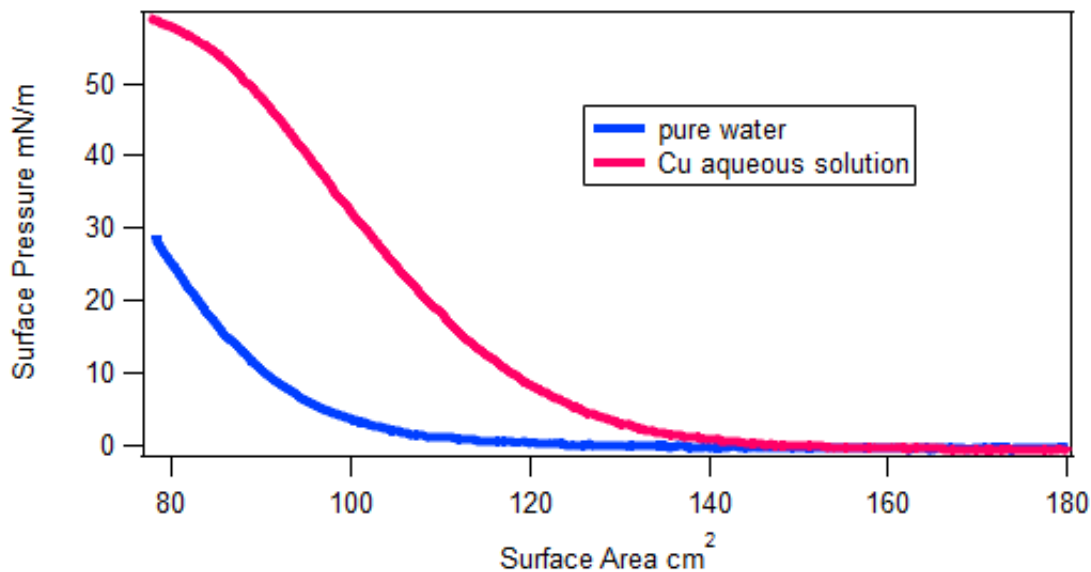
3.4 X-ray photoelectron spectroscopy

To verify the elemental composition of the sheets, X-ray photoelectron spectroscopy (XPS) was implemented. A wide XPS survey scan of the sample confirmed the existence of different elements. With Si 2p coming from the substrate, C 1s, O 1s, H, and Cu 2p signatures from the 2D-MOF layer confirm the successful formation of a SURMOF network (Fig. 3.5). No chlorine peak was detected in the XPS spectra, confirming the lack of untreated copper chloride on the air–water interface. Exclusively, the oxidation state of Cu cations was elucidated by XPS studies. Copper-, oxygen-, and carbon-related peaks can be seen in a zoomed-in scale in Fig. 3.5. The Cu 2p peaks in the XP spectrum are dominated by two spin-orbit components of Cu 2p 3/2 and Cu 2p ½. A doublet is clearly resolved at 934.2 and 954.3 eV, which is assigned to the Cu II species (Fig. 3.5). Analogous satellite peaks were observed earlier in CuO, indicating that Cu in the MOF is in the divalent form. The Cu-MOF structure was further characterized by the intense hydrocarbon C 1s peak at 285.0 eV and the carboxylate (-COO) C 1s peak at 286.6 and 288.7 eV. Being the only feature detected in the O 1s spectrum, the O 1s peak at 532 eV guarantees the existence of the carboxylate species. Particularly, based on the O 1s data, the presence of any oxide impurities is excluded. These results are in good agreement with previously reported results[88].
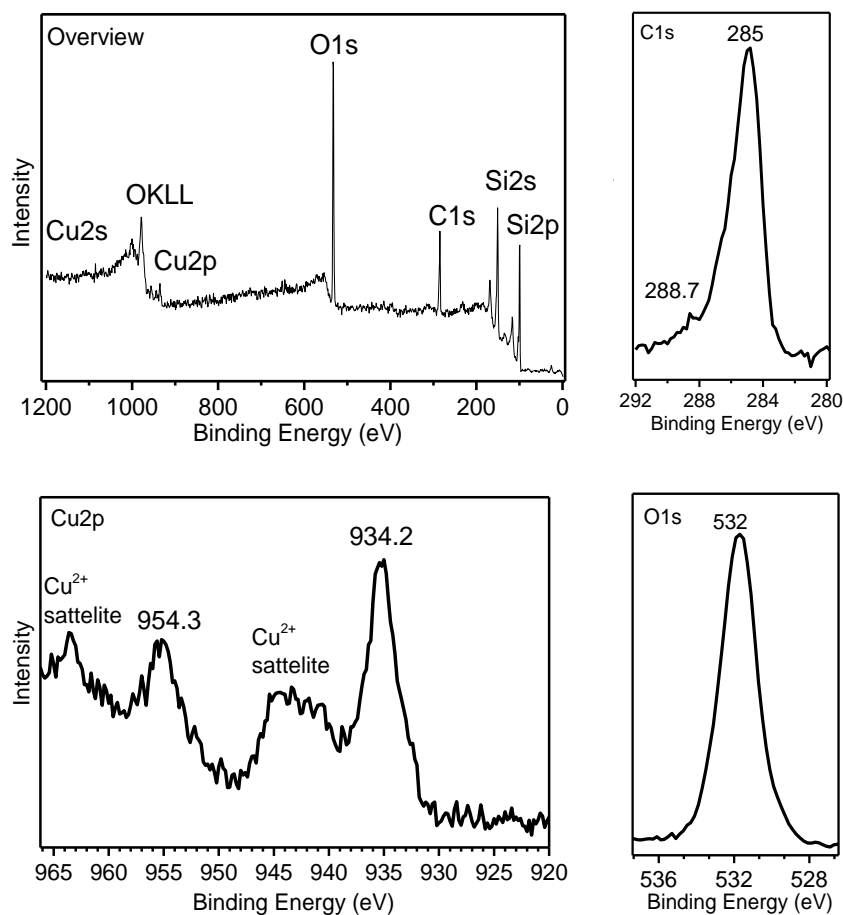
Figure 3.5: Survey scan of XPS spectra of 2D Cu-MOF and deconvoluted XP spectra of 2D Cu-MOF for Cu 2p, C 1s (upper scan) and O 1s regions (lower scan)

The isotherm studies and XPS data analysis give strong evidence of successful MOF film creation. The following chapters present characterization about surface homogeneity, film thickness, and crystallinity.

3.5 Topographic characterization with atomic force microscopy

As mentioned in Chapter 1, a major obstacle to successful sample preparation for femtosecond electron diffraction studies is forming large-area crystalline films. The desired film has to be continuous and have uniform crystalline orientation. To accurately determine these parameters, the AFM technique was used for the morphology and thickness analysis.

Since the silicon substrate used for SURMOFs preparation would not affect the morphology of the Cu-BTC single layer, it was first characterized as a reference for identifying

changes during the film adhesion. As Fig. 3.6 shows, the surface of the silicon substrate consists of a homogenous distribution of small grains that provide a relatively smooth surface.
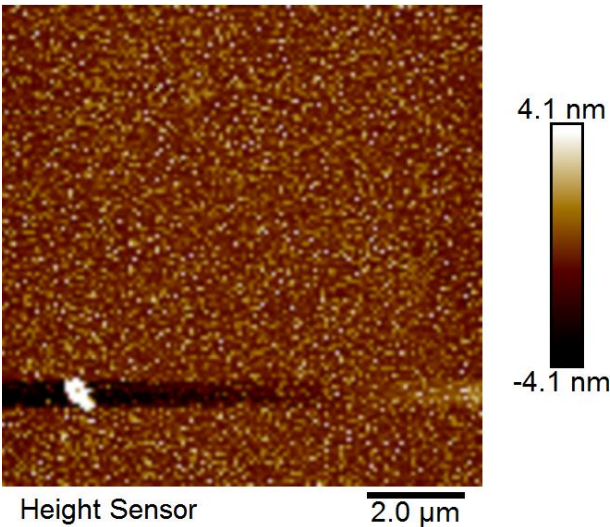

Figure 3.6: Topographic AFM image of silicon wafer substrate ((100) surface plane) taken as a reference for the SURMOF experiments

Fig. 3.7 shows the morphology of the Cu-BTC layer. Sheet domains of 20–180 nm come together to form flakes with a diameter in the range of 500 nm–1.5 μm. There are homogenously distributed MOF flakes on the surface; however, the average height of the flakes implies that the sheets are not monomolecular but composed of several layers. Ultimately, the desired MOF films would be homogenously distributed on a large surface area and have a uniform crystal orientation.
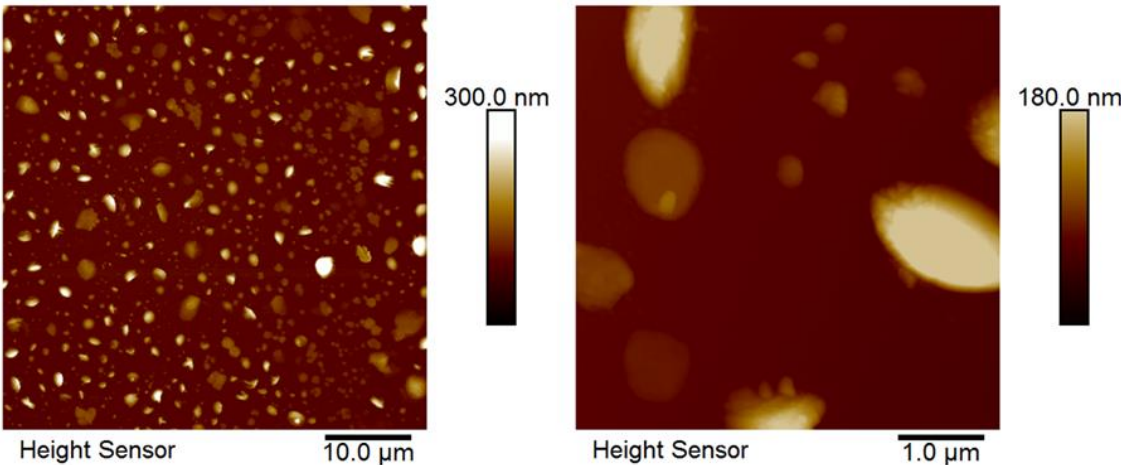

Figure 3.7: AFM height images of one deposition layer. The films were formed at a surface pressure of 30 mN/m and transferred onto silicon substrates

Because it is difficult to understand whether fracture and crumbling happen during the film transfer or during drying, Figure 3.8 gives a possible explanation of the deformity of the MOF film growth.
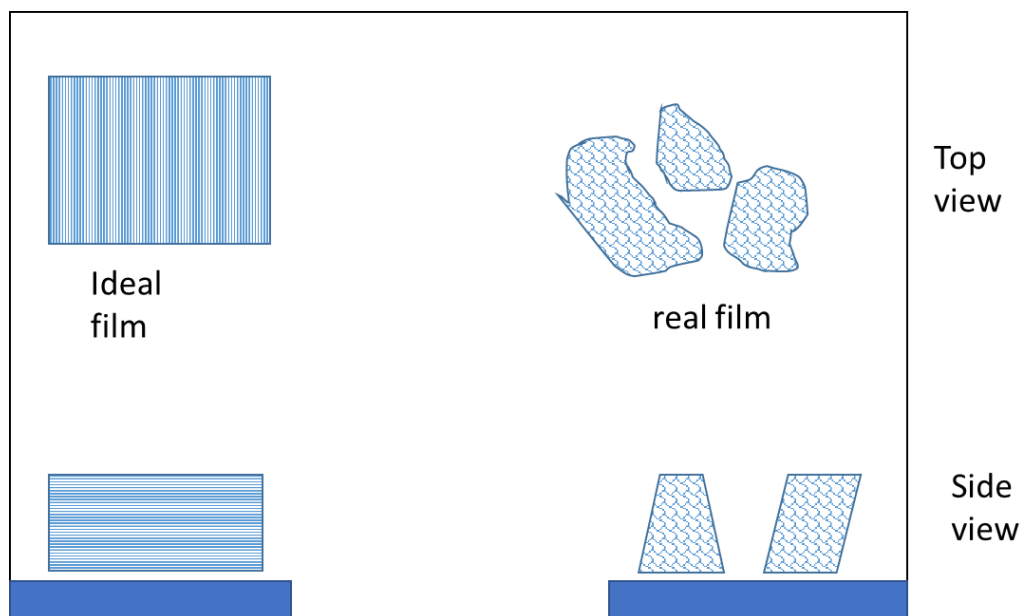

Figure 3.8: The ideal MOF film versus the state-of-the-art MOF thin film

The most likely scenario involves the formation of flakes that look like small 'islands'. For a continuous film to be formed, the LB is compressed and the 'islands' come closer into a large film. To understand the mechanism involved, the reaction between the individual islands has to be explained. A lack of interaction and reaction between the islands is a possible explanation and/or the creation of several layers could led these 'islands' to overlap during the compression. Since there was no collapse according to the isotherm studies, the surface coverage was sufficient. Usually in the best-case scenario when the 'islands' coalesce, small voids will be left behind. These voids will probably create defects on the film homogeneity. In our case, there were voids left behind, and the created MOF islands were overlapping. The resulted film defects can be expected from the small-area coverage and a lack in film homogeneity. A second scenario deals with the transfer or drying procedure. If the sheets do not strongly adhere on the substrate during drying, they most likely dehydrate and shrink.

3.6 Absorption spectroscopy studies

Selected absorption spectra for different numbers of depositions are shown in Fig. 3.9, and the successive deposition cycles can be confirmed by the evolution of the absorption spectra. A linear increase in absorbance with an increasing number of deposition layers signifies that, during each deposition cycle, the substrate surface is well covered with the Cu-BTC monolayer. The dependence of the absorbance on the number of depositions at a certain wavelength is displayed in the inset of Fig. 3.9. The multilayer samples appear to absorb mostly at a low wavelength (230–300 nm). Particularly, the general absorption features of the spectra appear not to depend on the number of deposition cycles, leading to the conclusion that the stacked monolayers retain their 2D nature.

These results prove that sequential deposition of 2D-MOF is possible and can therefore offer control of film thickness. The layer-by-layer modules on a 2D base to form 3D complex structures should be of interest in future strategies[15]. This could be optimized depending on the MOF application, where the fabrication of ultrathin films containing MOF structures could be used for adsorption studies or biological uses[89-94]. For our applications, this approach provides a useful tool for preparing samples for femtosecond electron diffraction studies. It consists of a possible method to functionalize such MOF networks as heterostructured SURMOFs, where the surface relies on growing layers of different but structurally related MOFs on top of each other[95]. Guest–host MOF molecules would be attractive candidates too, as they would reveal the chemical MOF behaviour and the dynamics triggered by these reactions.
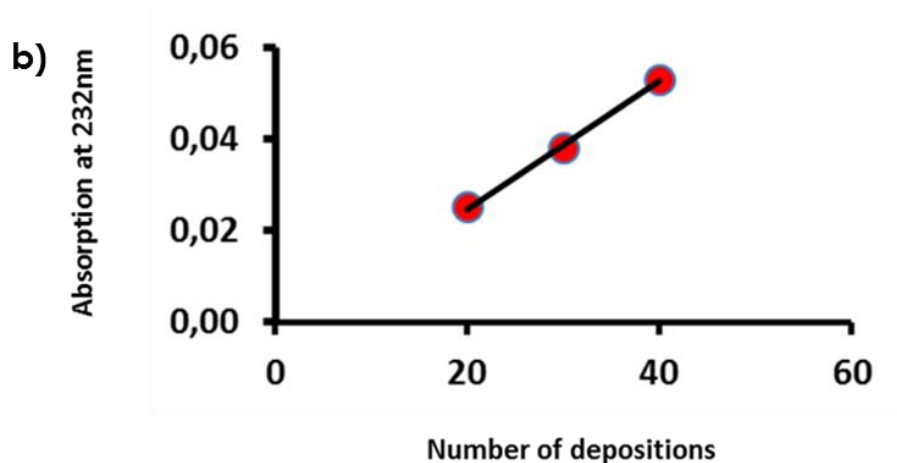
b)
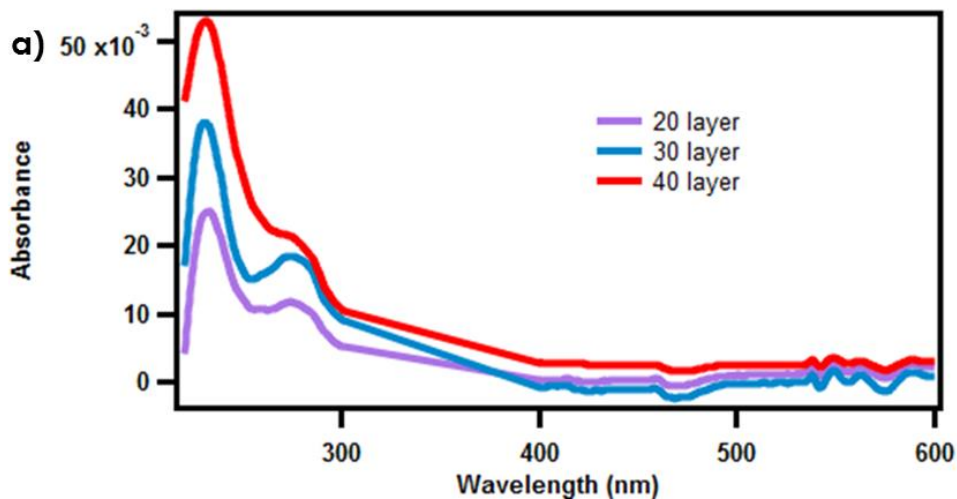
Figure 3.9: (a) Layer-by-layer film growth, followed by ultraviolet-visible absorption spectroscopy. The following deposition layers are 20 (purple), 30 (blue), and 40 (red) at a surface pressure of 30 mN/m. (b) The inset shows the absorption at 232 nm as a function of the deposition numbers.

3.7 Transmission electron microscopy measurements

After the surface area characterization, transmission electron microscopy (TEM) was used for a primary crystallinity check. However, there are some restraints when it comes to MOF stability. Their instability under the electron beam can lead to the loss of information. Thus far, only a few MOFs had been imaged in their intact form, and even fewer SURMOFs had been studied with this technique.

The crystals of the Cu-BTC revealed flake-like shapes (islands) (Fig. 3.10). The diameter of the flakes ranges from 100 nm to 500 nm, and the round plate shape as well as the diameter range is in agreement with the AFM topological images. Although a single deposition cycle was performed, the morphology revealed the creation of a bilayer. The background features suggest that the whole TEM window surface was covered with material. The MOF flake overlap could be a result of the high pressure or the deposition cycle preparation. It is possible that the sheets tended to shrink during the transfer process, but they were stable enough to attach more structures.
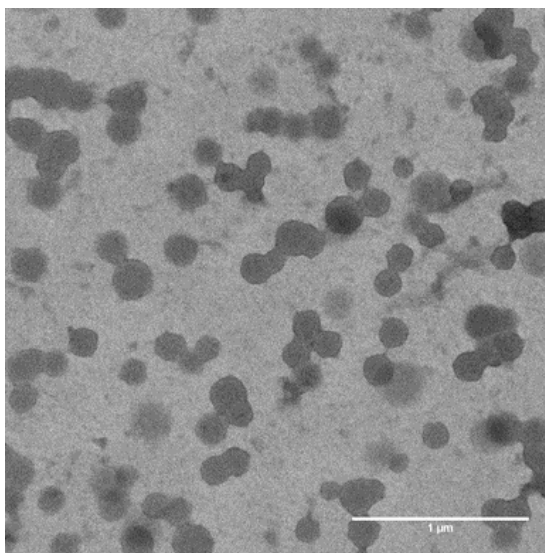
Figure 3.10: TEM image of Cu-BTC single deposition MOF with the LS deposition method and surface pressure 30 mN/m

Fig. 3.11 and 3.12 shows a typical SAED pattern of the Cu-BTC MOF monolayer. It is a representative pattern formed by a nanoparticle diffraction in a size range of 200–500nm (bright field image Fig. 3.11) with a minor partial overlap. The broad diffuse rings are indicative of the scattering from the silicon nitride window, and the sharp peaks confirm the single-crystal nature of the flakes. To further evaluate the MOF stability under the electron beam irradiation a time series of SAED patterns was acquired to monitor the structural degradation. From the authors experience the reflections of a MOF can vanish within seconds or minutes.
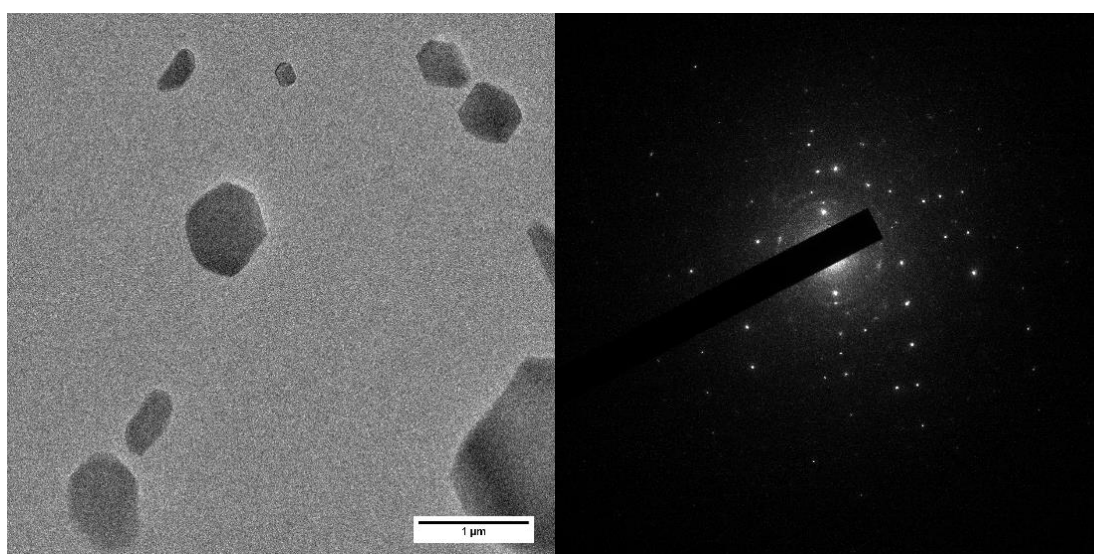

Figure 3.11: TEM (left) and SAED (right) of Cu-BTC MOF for single-cycle depositions on Si_3N_4 at surface pressure 30 mN/m
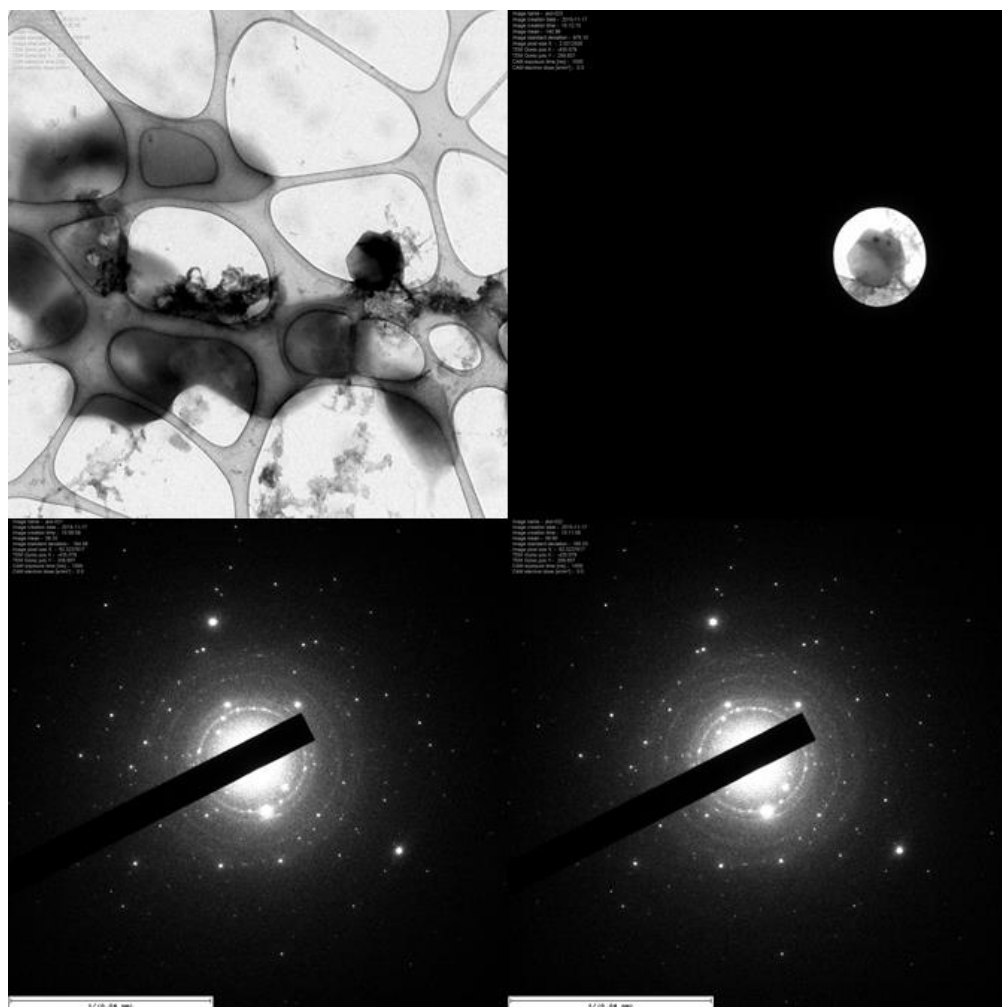
Figure 3.12: TEM (top) and SAED (bottom) of Cu-BTC MOF for single-cycle depositions on Lacey carbon films on copper TEM grids at surface pressure 30 mN/m

Despite MOF materials being known to be highly unstable under electron irradiation, TEM images have proven crucial for many MOF applications. The ability to study the size and morphology, as well as to observe embedded nanoparticles as guest molecules, has led to many discussions[96]. A defined crystal shape derived from TEM images can be connected to the crystal structure, assuming that the images are combined with electron diffraction[96, 97]. Large-area single crystals would be the ideal product of the film growth efforts. Still, the results of this work are promising as they presented a straightforward approach to a 2D structure. These MOFs have the potential for a better structure self-growth monolayer, and some modifications will eventually allow for a better control of the film size.

4. Dithienylethene (DTE) derivatives

4.1 Synthesis of thin films of photochromic dithienylethenes

DTEs are a family of photochromic compounds that undergo photoinduced reversible isomerization in both the solution and the crystal phase. In this thesis, i report a series of amphiphilic DTEs in the bilayer membrane of lipid vesicles. The objective was thin film creation and thus the study of three different photochromic amphiphilic dithienylethenes for femtosecond electron diffraction. The ultimate goal is to directly resolve the atomic motions involved in the ring closing/opening reaction induced in a photochromic single crystal as in reference [98] but under 2D boundary conditions[98].

Systems of low dimensionality have received a lot of attention due to advancements in technological fields that require these nanostructures[99]. Furthermore, systems that are prepared from responsive molecules can be used as examples of programmable soft matter. In particular, materials that can be switched between well-defined states with light have promising 'smart' applications such as the development of high-capacity optical data storage devices. Photochromic materials based on the dithienylethene molecular switch are apt for such applications[99].

Langmuir–Blodgett/Schaefer (LB/LS) films of three different photochromic amphiphilic dithienylethenes were used for the preparation and evaluation of 2D photoresponsive materials. Similar LB films incorporating azobenzene and spiropyran have been examined, but since they are thermally reversible, their potential applications are limited. In contrast, only a few instances of DTEs in LB films have been reported[100, 101].

To investigate the photochromism of amphiphilic DTEs in organized assemblies, and thus to expand their application to 2D materials, the objective of this thesis in the following chapters is to assess the spreading behaviour and stability of Langmuir films of DTE-**1**, DTE-**2**, and DTE-**3** amphiphilic DTEs as single components. The photochromism and the nanostructure of multilayer LS films were examined using different characterization techniques such as UV-vis, AFM, and TEM. A successful film fabrication would be the future material for a more in-depth observation and a potential molecular movie creation.
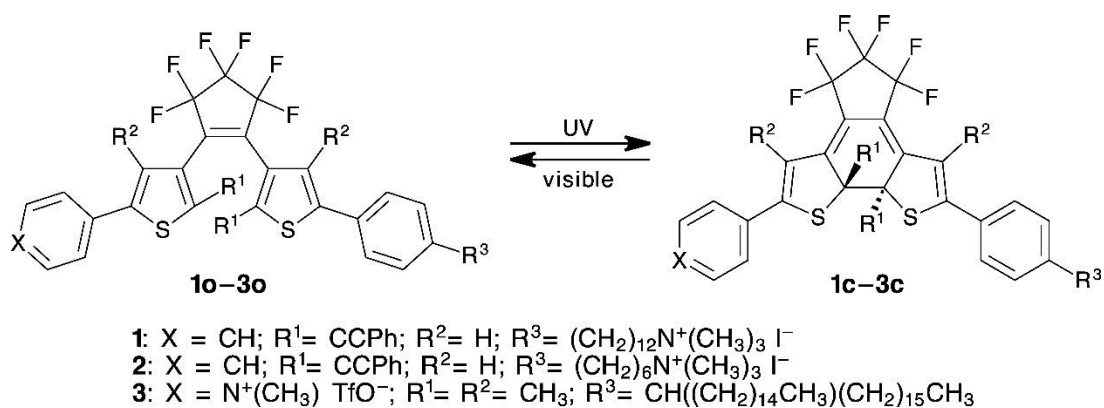
Figure 4.1: Structure formation of the examined dithienylethene photoisomers DTEs **1–3**. Figure adapted with permission from [36]

4.2 Langmuir–Blodgett monolayer studies

The surface pressure-area isotherms of the DTEs **1–3** were formed at the air–water interface, which led to the characteristic surface pressure-area isotherms. The prime reason for using this technique is to qualitatively assess differences in the packing arrangements of DTE isomers (open-ring and close-ring forms) as Langmuir films. It is assumed that the assembly of DTE isomers depends on their molecular structure (mean molecular area). The structure differences are expressed by relative differences in the surface pressure-area isotherms. Close-packed monolayers formed as large patches of ultrathin solid material were compressed. No changes have been observed in surface pressure when the trough area was above 120 cm^2, whereas the maximum surface pressure was reached when the area was 75–85 cm^2. In addition, for stock solution volumes less than 120 μL, there were no changes on the surface pressure during compression, indicating that the total area of the transferred material was less than 75 cm^2. For a volume greater than 120 μL, an irreversible collapse of the Langmuir film was observed. This technique allows us to assess the approximate differences in the packing arrangements of DTE isomers (open-ring and closed-ring forms) as molecular monolayers. We hypothesize that the assembly of DTE isomers depends on their molecular structure (mean molecular area). Any differences in structure are expressed as differences in the surface pressure-area isotherms and changes in the final surface pressures. Prior to these measurements, the mechanical stability of the Langmuir films was tested by performing five sequential compression and decompression cycles. The fact that there was no significant loss of material observed during these cycles suggests that these Langmuir films are reversible and stable. In Fig. 4.2, three sets of isotherms are shown for DTEs **1–3** on an ultrapure water

subphase surface. Each set represents three separate transfers from the same DTE stock solution under different irradiation conditions (no irradiation, UV light irradiation, and visible light irradiation). Within each set, the final surface pressure observed for an isotherm was qualitatively correlated to the relative area a monolayer of DTE isomers (or mixture of isomers) occupies, as the total number of molecules deposited was constant.
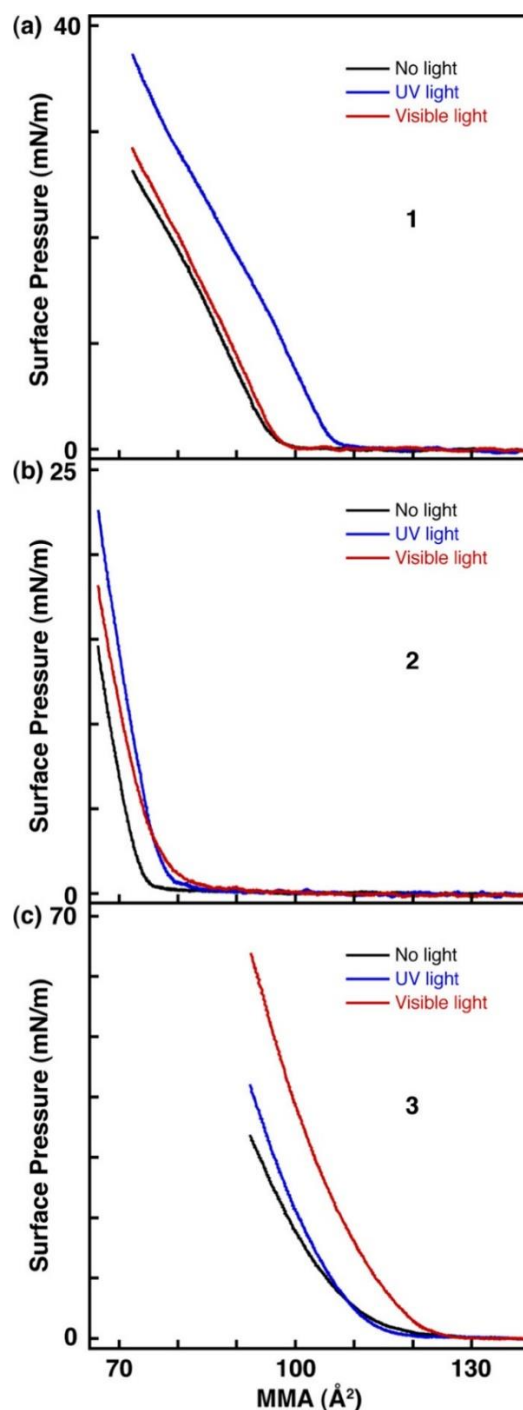

Figure 4.2: Surface pressure-area isotherms of (a) DTE-**1**, (b) DTE-**2**, and (c) DTE-**3** on a pure water subphase surface. Each plot contains three isotherms that represent Langmuir films

prepared from the same DTE stock solution under three different irradiation conditions: no irradiation (black), UV light irradiation (blue, 6 W UVA lamp, λ=365 nm, 6 min), and visible light irradiation (red, 53 W halogen lamp, 2 min). For each isotherm, the deposited volumes were 120 μL and the concentrations were 0.15 mg/ml

By composing the isotherms for DTE-**1** and DTE-**2**, we can see an increase in the final surface pressure of the monolayers that is created from the UV-irradiated solutions at the photostationary state compared to the monolayers created from the non-irradiated solutions. This suggests that the intermolecular organization between the closed-ring isomers of DTE-**1** and DTE-**2** derivatives needs an area that is larger than a monolayer of their analogous open-ring isomers at the air–water interface. This can be explained with reference to previous studies that show that the closed-ring isomers of DTEs having phenylethynyl groups at the reactive carbon sites have a larger molecular volume than the open-ring isomers[102]. The surface-pressure changes were also reversible for monolayers prepared from DTE-**1** and DTE-**2** solutions irradiated with visible light. The final surface pressures were, however, lower than the ones obtained from the UV-irradiated samples. For derivative DTE-**1**, reversibility was almost quantitative, whereas, for derivative DTE-**2,** the switching was not complete, and the final surface pressure was still higher than the non-irradiated sample pressure. This difference in the extent of the reversibility is possibly due to the difference in cycloreversion quantum yields as DTE-**1** is more than 2-fold greater than DTE-**2**. For comparison, some tests were done using a direct UV or visible irradiation process to the monolayers created on the trough, but this did not produce any surface pressure changes. This could be because the close-packed structures do not have space for large changes in the molecular volume that can come along with the photoisomerization of DTE-**1** and DTE-**2**. As a reference, the parent nonamphiphilic derivative does not undergo photoisomerization in the crystalline state[102]. Remarkably, the same differences in the final surface pressure for the DTE-**1** and DTE-**2** derivatives and the corresponding photochromic reaction in ring-closed and ring-open isomers have been reported in the literature with azobenzene derivative systems behaving the same way[103].

For derivative DTE-**3**, the same behaviour was observed for monolayers created from UV irradiated samples. There was an increase in the final surface pressure, which could also suggest that the assembly of the closed-ring isomers occupies a larger surface area than that of the open-ring isomers. Interestingly, the relative magnitude of the final surface pressures

was significantly higher for DTE-**3** than those observed for DTE-**1** and DTE-**2**. This could mean that the effective molecular area of DTE-**3** is packed differently and occupies larger spaces on the air–water interface, considering that the spread volume and concentrations of all comparative DTE solutions were the same. This would suggest that the branched-alkyl chains of DTE-**3** occupy a larger area within a monolayer than the photochromic parts of DTE-**1** and DTE-**2** do. After the visible light irradiation, the spread solution of DTE-**3** was compressed to a monolayer, an increase in the surface pressure was observed. The irreversibility of derivative DTE-**3** was not expected because it was reversible in solution. To better understand the reason behind the observed Langmuir film expansion for DTE-**3** following visible irradiation, AFM and TEM were used, which are described in the following chapters to examine LS films of DTE-**3** under different irradiation conditions. The crystallinity and surface area coverage of DTE-**1** and DTE-**2** were also examined.

4.3 Langmuir–Schaefer film absorption studies

Absorption spectroscopy was used to examine the photochromism of the resulting LS films. At first, films were prepared for all DTEs from non-irradiated stock solutions and the absorption spectra were similar to those observed in the solution. However, only derivative DTE-**3** exhibited reversible photoisomerization as an LS film. This, in turn, is encouraging. The major change in the molecular volume accompanying the photoisomerization of DTE-**1** and DTE-**2** seems to be shape-limited when it comes to film formation where derivatives like DTE-**3** (non-amphiphilic) are photochromic in the crystalline state. Relating to our solution studies, UV irradiation of DTE-**3o** derivative as a film prepared from 50-layer sequential depositions shows an increase in absorbance in the visible region with a corresponding decrease in the UV region (Fig. 4.3). These changes clearly suggest the formation of closed-ring isomer DTE-**3c** in a multi-layer film and are confirmed by the UV-vis spectra on the open-to-closed-ring reaction for analogous systems[104-108].
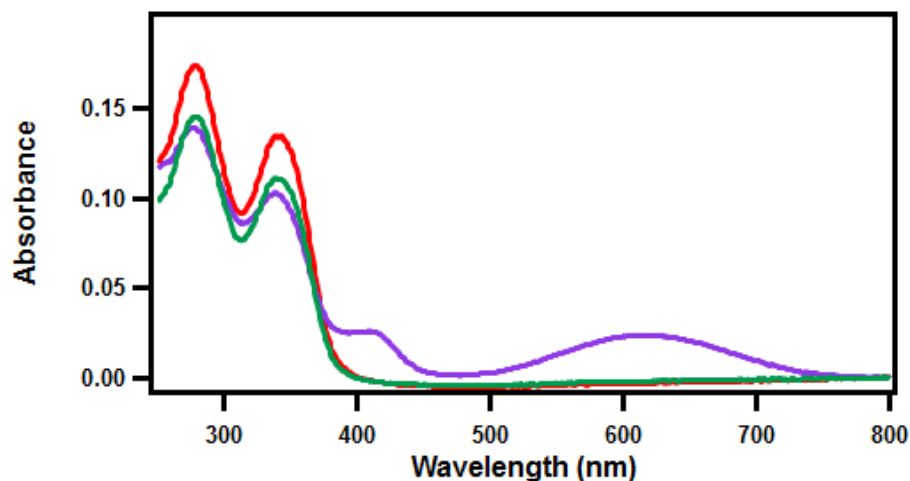
Figure 4.3: Absorption spectra of a 50-layer deposition of DTE-**3o** form in solution without UV irradiation (red), UV irradiation (purple), visible light irradiation (green)

To test the reversibility of derivative DTE-**3** in LS film form and confirm any possible change in absorption, another 50-layer LS film of DTE-**3c** form derivative was made. Upon irradiation with visible light, the absorbance of the DTE-**3c** form decreased within the visible region (Fig. 4.4). The degree of change in absorbance was less than what was observed during the solution phase for the same irradiation times, which was expected according to the LB isotherm studies. Still, the photoisomerization of the DTE-**3c** form derivative was reversible upon multilayer thin film formation.
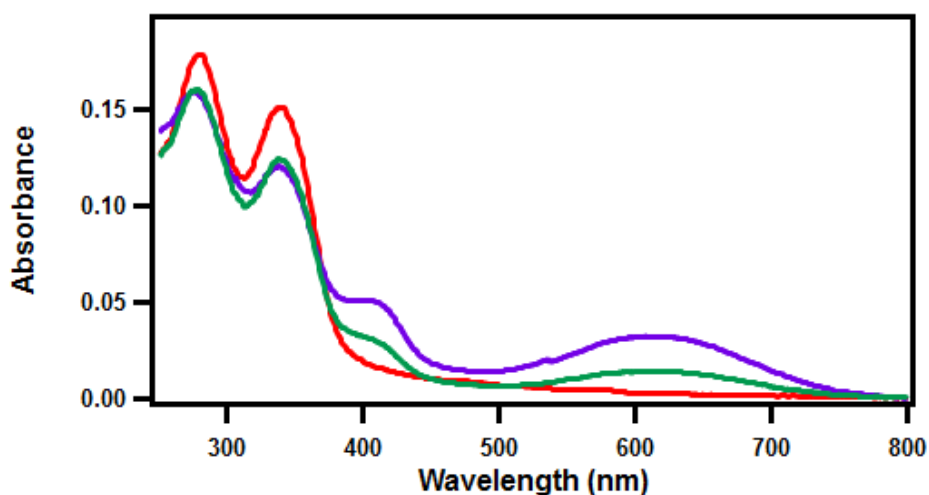

Figure 4.4: Absorption spectra of a 50-layer deposition of the DTE-**3c** form on solid UV and visible light irradiation. No light irradiation (red), UV light irradiation (purple), visible light irradiation (green)

It is important to note that the shape of the absorption spectra is independent of the number of depositions because the monolayers within a multilayer structure retain their 2D structures (Fig. 4.5). In addition, a linear correlation is observed between the intensity of the absorption bands and the number of depositions. This constitutes a proof that the same amount of material is transferred within each deposition cycle. Taking advantage of this behaviour, a multilayer deposition of DTE derivatives can be used for the creation of LS films with a relatively high precision over film thickness.
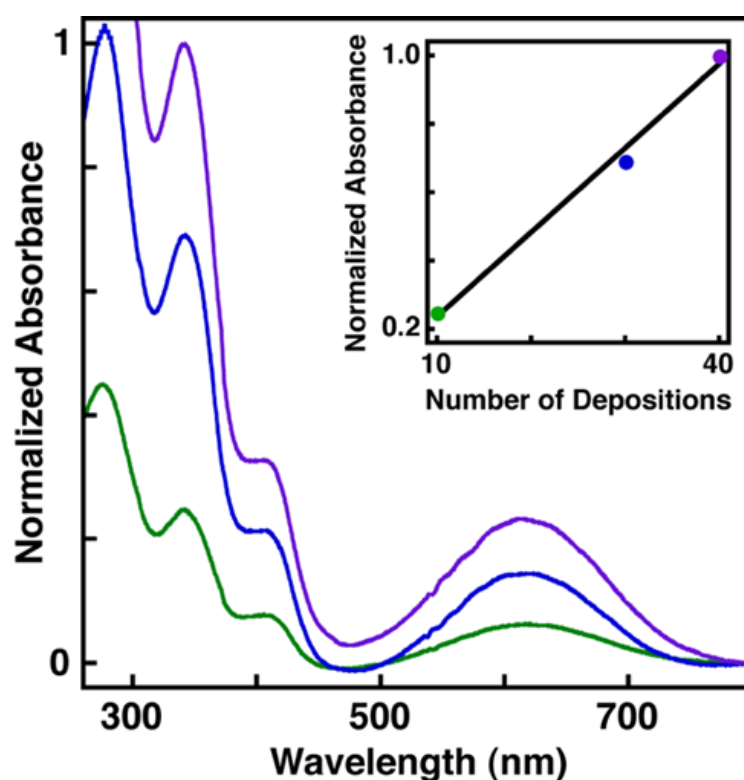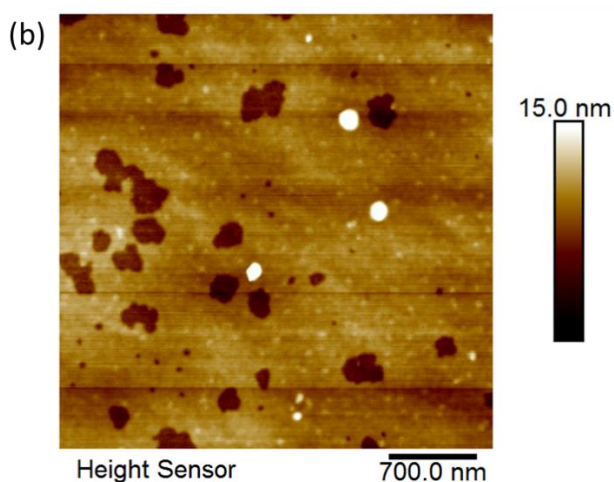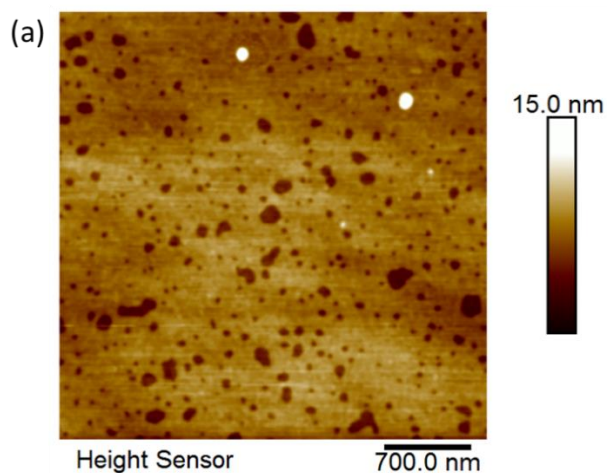

Figure 4.5: Normalized absorption spectra of the DTE-**3c**-form derivative as LS films prepared from 10 (green), 30 (blue), and 40 (purple) sequential layer depositions. A linear relationship between the normalized absorbance at 605 nm within the number of depositions is shown in the inset

4.4 Atomic force microscopy studies

For the LS films prepared for derivative DTE-**1**, there is a structure change between small spheres with no light irradiation to large agglomerates after UV light irradiation, and a reverse into the initial shape following the visible light irradiation (Fig. 4.6). An image description could be that spheres are distributed into agglomerates after the light irradiation

and come back to their initial shapes after being irradiated with visible light. This could explain the increase in surface pressure from lower surface pressure when there is no light irradiation to higher surface pressure after the sample is irradiated. Following a visible light irradiation, the morphology is almost completely reversible, a fact that matches the surface pressure decrease. Every irradiation procedure was a different experiment, which can explain the dissimilar covered area and the molecule population. Nevertheless, the sphere shapes were always the same after repeating the measurements and the experiment a few times. Gaining an insight into the morphology of the sample, we tried to explain the different molecule packing, and the homogeneity of the film and the void's existence. The film thickness is within the optimal nanometre range.
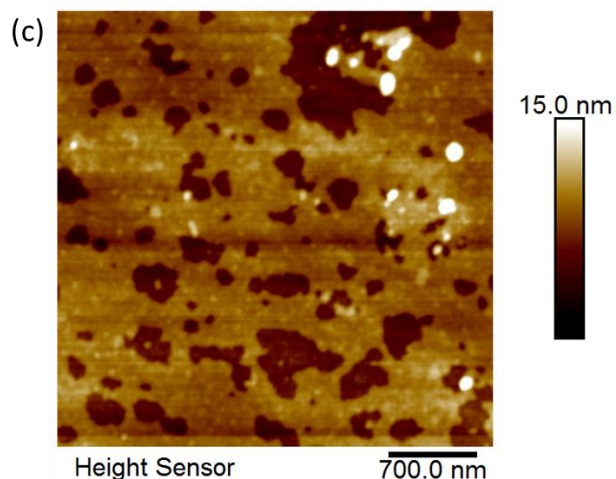
(a)

15.0 nm

Height Sensor   700.0 nm

(b)

15.0 nm

Height Sensor   700.0 nm

(c)

15.0 nm

Height Sensor   700.0 nm

Figure 4.6: AFM images of a single-layer deposition of derivative DTE-**1**. The images correspond to (a) no light irradiation, (b) UV light irradiation (6 W UVA lamp, λ=365 nm, 6 min), and (c) visible light irradiation (53 W halogen lamp)

For derivative DTE-**2,** the same procedure was followed. Here, what we had expected to see was partial reversibility, according to the surface pressure results. A different packing after UV irradiation was observed. As with derivative DTE-**1**, the small aggregate structures turn into bigger agglomerates after the UV irradiation time and switch back to the initial form under visible irradiation times. Figure 4.7 shows the monolayer morphology onto the silicon substrate during the different irradiation phases. As mentioned above, there is an agreement with the Langmuir isotherms and the results were reproducible after every experimental procedure.
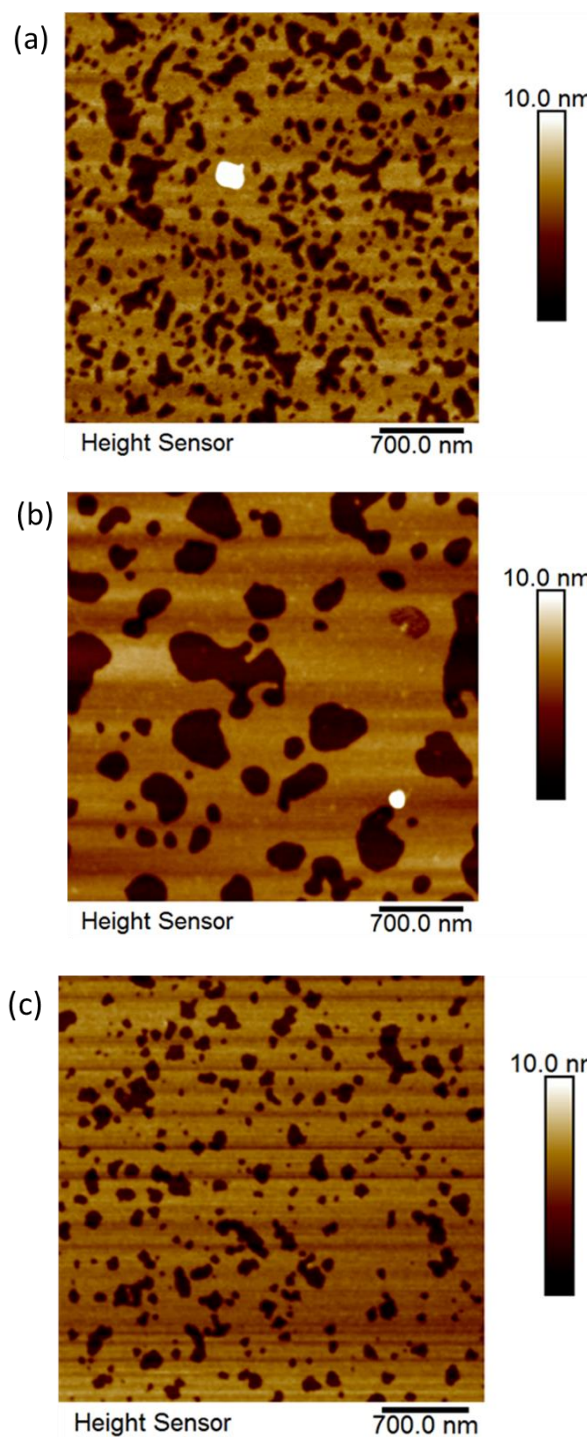
Figure 4.7: AFM images of a single-layer deposition of derivative DTE-**2**. The images correspond to (a) no light irradiation, (b) UV light irradiation (6 W UVA lamp, λ=365 nm, 6 min), and (c) visible light irradiation (53 W halogen lamp)

To better understand the unexpected expansion observed for derivative DTE-**3**, the same qualitative examination of the structure was used. Following the previous Langmuir film

transfer steps, a single deposition to silicon substrates was made. According to the surface pressure isotherms, an irreversible behaviour was anticipated. As expected, aggregated structures with spherical shapes were formed prior to any irradiation process. Unlike the previous morphologies, this derivative showed a different behaviour, under different irradiation conditions. In particular, an LS film prepared from a solution of DTE-**3o** shows aggregate structures with slightly round shapes, with an average diameter of about 70 nm. This suggests that the DTE-**3o** forms multimolecular aggregates during the formation of a Langmuir film or during the preparation of an LS film. There is a precedent for the former, as the aggregations of amphiphilic azobenzenes[109, 110] and spiropyrans[111-113] have been observed in Langmuir films at low surface pressures. Although amphiphilic DTEs have never been examined as a single component in Langmuir films, the aggregation of amphiphilic DTEs in an aqueous solution and photoinduced changes in the morphology of these aggregates have been reported[114-117]. After UV irradiation of DTE-**3o** (DTE-**3c** at the photostationary state), the morphology turned into large continuous structures with random shapes, suggesting a batch comprising the smaller aggregated structures of DTE-**3o**. This photoinduced aggregation suggests a change in morphology for these self-assembled structures on the water subphase. This is an outcome deriving from intermolecular packing between photoisomers within these aggregated structures. It is known that the rigid closed-ring isomers form more planar aggregates than flexile open-ring isomers do. A recent report confirmed the same behaviour for an amphiphilic DTE with oligo (ethylene glycol) side chains in water[115]. It was shown to undergo a reversible photoinduced morphological change in water among colourless microspheres and coloured fibres. After visible light irradiation, a further coalescence can be observed, producing larger continuous aggregates. We hypothesize that these large aggregates and the large void spaces between them are most likely responsible for the significant increase in the surface pressure recorded for the compression isotherm of DTE-**3c** following visible irradiation.

Although stock solutions of DTE-**3c** in chloroform were irradiated with visible light for appropriate stretches of time, it appears that even a small amount of DTE-**3c** hinders the formation of smaller circular structures observed for DTE-**3o** and favours the formation of large irregular aggregated structures.
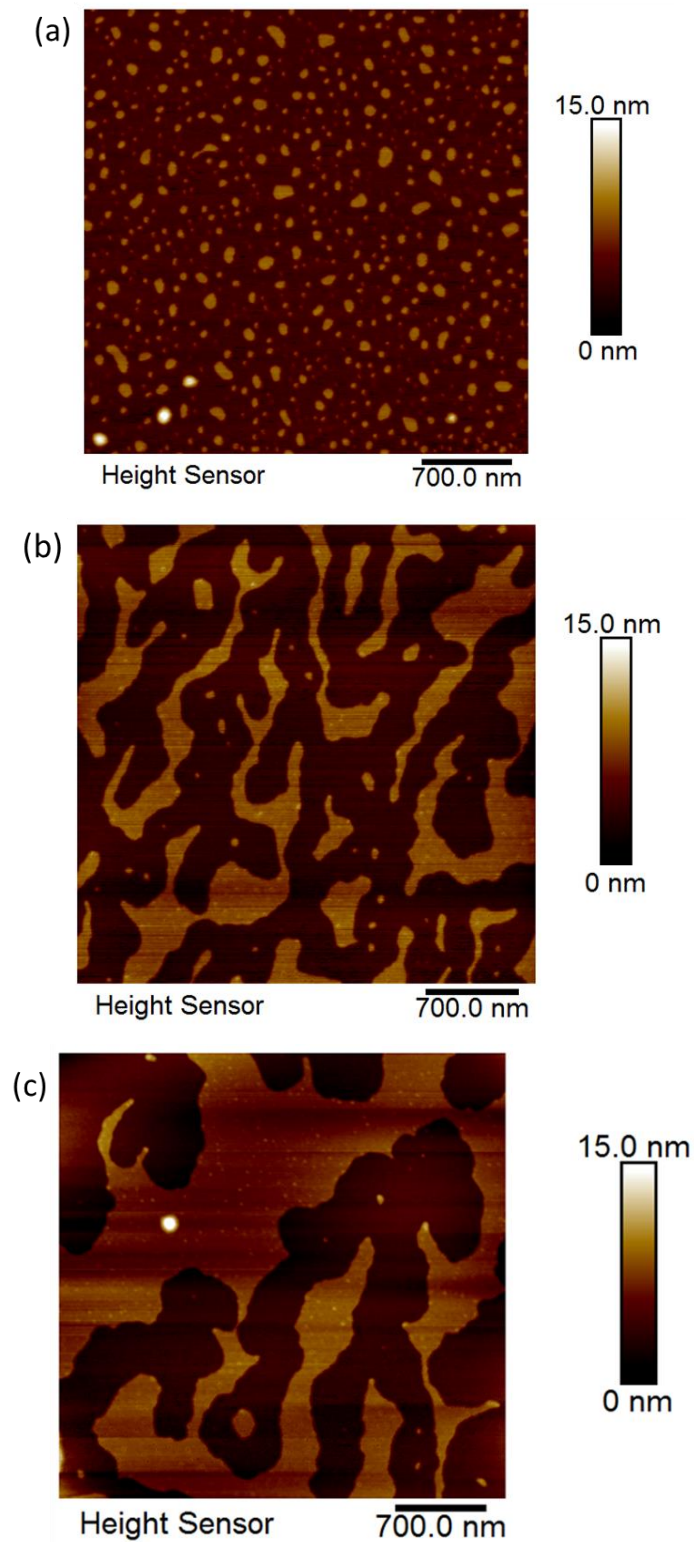
Figure 4.8: AFM images of a single-layer deposition of derivative DTE-**3**. The images correspond to (a) no light irradiation, (b) UV light irradiation (6 W UVA lamp, λ=365 nm, 6 min), and (c) visible light irradiation (53 W halogen lamp, 2 min)

However, upon UV irradiation, these DTE-**1c** and DTE-**2c** films become more uniform with fewer but larger void spaces. For all DTEs, the LS film has an average thickness of 4 nm, introducing that the compounds of the aggregated structures are not solely composed of a single monolayer. The hypothesis behind this is that the monolayers are partially disrupted by bilayer or multilayer contractions, which are possibly formed during the deposition. These defects can cause disruptions in the film homogeneity. Besides the comparison study, the film coverage was not sufficient to better understand these behaviours in action. Further information about the crystallinity of the films is presented in the following chapter.

4.5 Transmission electron microscopy studies

While derivatives DTE-**1** and DTE-**2** diffracted well, derivative DTE-**3** did not show any diffraction. To further support the photoinduced morphological changes observed for DTE-**3,** it was examined in all stages after irradiation, but derivatives DTE-**1** and DTE-**2** were examined only before and after UV irradiation.

More specifically, real space imaging for derivative DTE-**1** showed morphology resembling small spheres, which were trapped on a thin membrane layer without any light irradiation. After UV light irradiation, the conglomerates turned amorphous. Owing to the surface compression, more than a single layer was transferred onto the substrate and the lipid molecules overlapped. In Figure 4.9, real space images (a and b) and the additional diffraction patterns reveal the differences in the structure evolution of lipid DTE-**1** before and after UV irradiation. The molecule transformation after light irradiation gives insight into molecule packing on the water surface and molecule aggregation after light triggering.
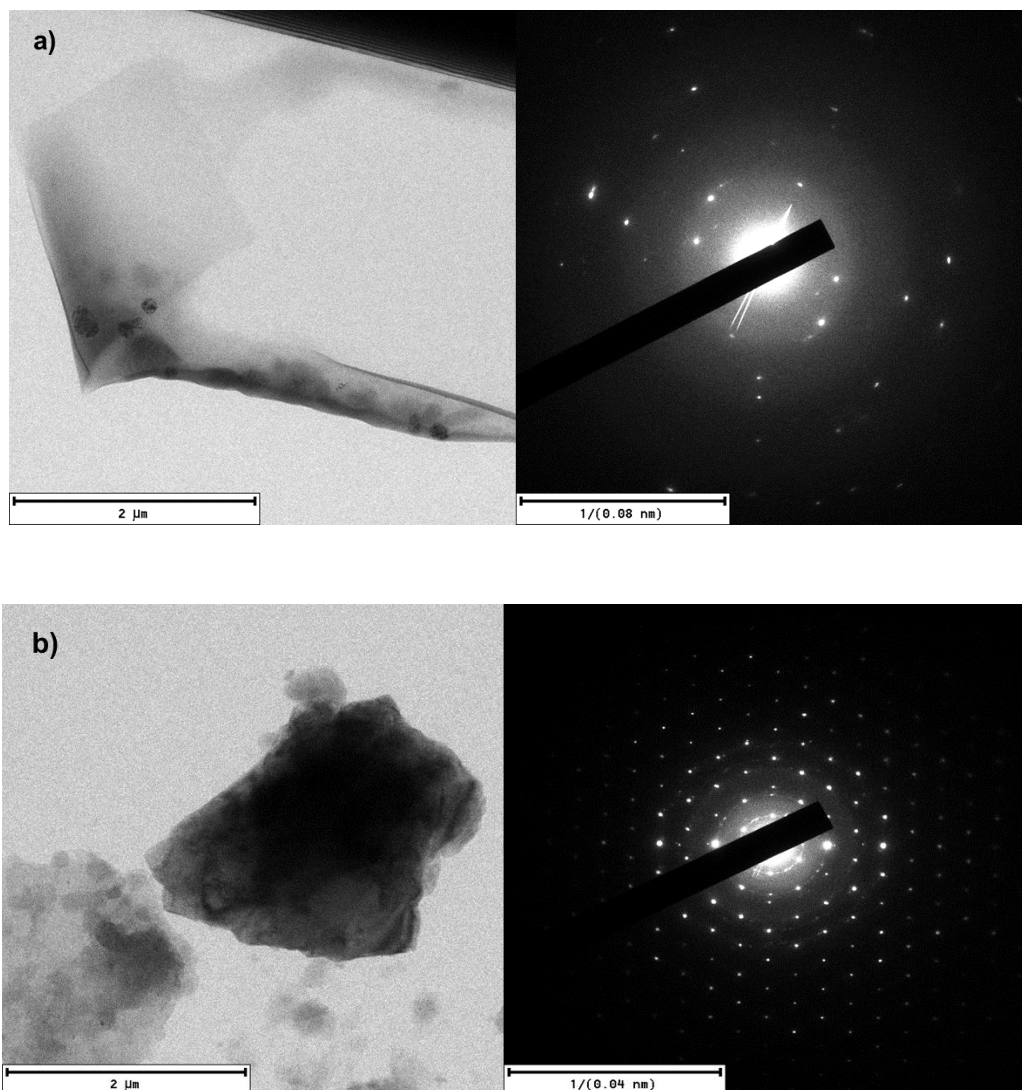
Figure 4.9: a) Derivative DTE-**1** prior to light irradiation and b) after UV light irradiation. A molecule agglomerate is noticeable, and the diffraction patterns prove the single crystalline nature of the product

Same studies were performed on a single-layer sample of derivative DTE-**2**. The particle formation was slightly different and disfigured, and so was the particle aggregation after UV light irradiation. No membrane formation could be seen here; however, the diffraction patterns were similar to the ones for derivative DTE-**1**. The representative images can be seen in Figure 4.10.
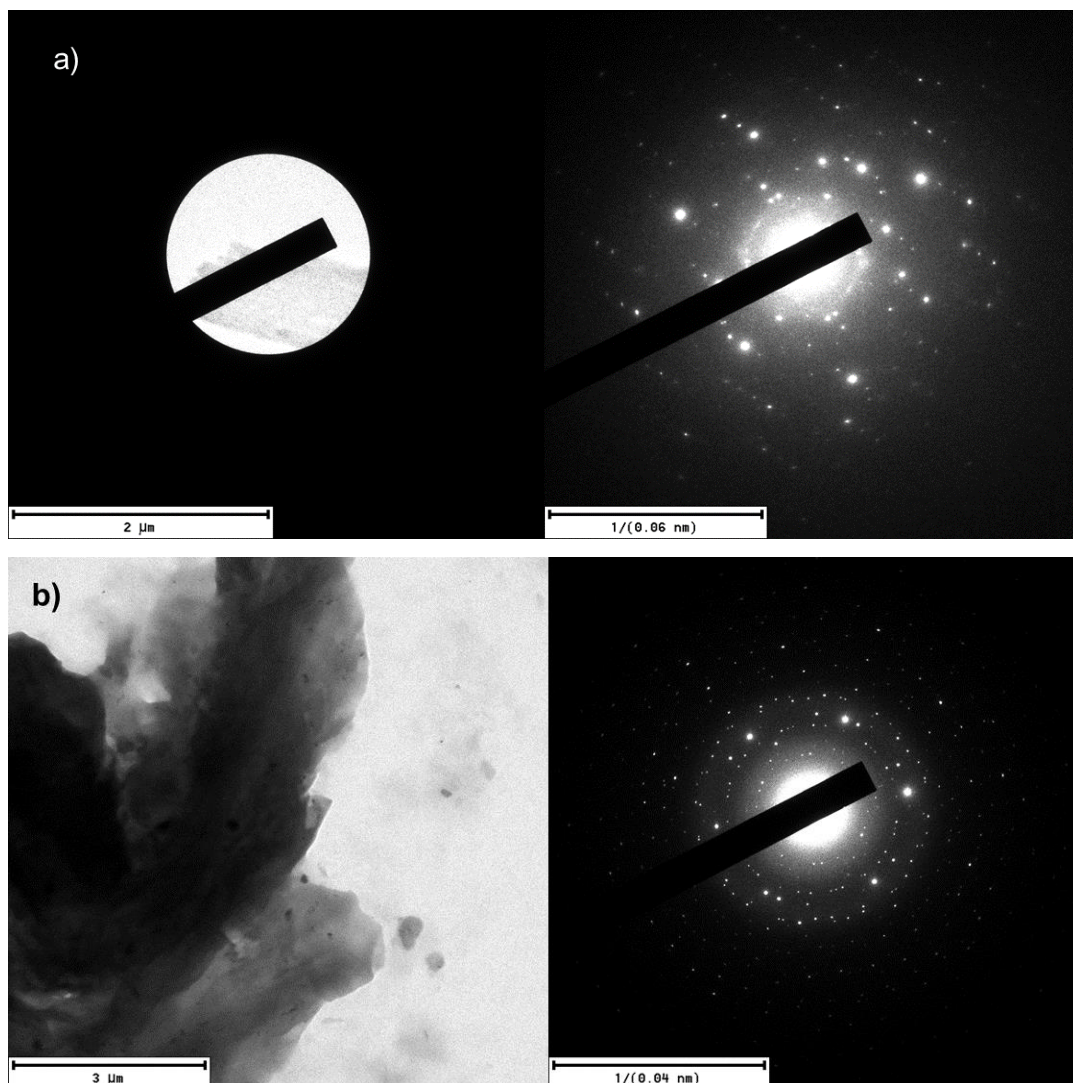
Figure 4.10: a) Derivative DTE-**2** prior to any light irradiation and b) after UV light irradiation. A mass molecule aggregation is noticeable, with the diffraction patterns indicating the single-crystalline nature of the product

In contrast to the previous derivatives, derivative DTE-**3** did not show any diffraction signals. An LS film of DTE-**3o** shows well-defined circular structures, whereas following irradiation with UV light these structures coalesce into irregular wormlike structures (Fig. 4.11 (a), (b)). Unlike the photochromism observed in LS films via absorption spectroscopy, this photoinduced change in morphology is not readily reversible. In Figure 4.11 (c), the image of the same stock solution clearly shows the reappearance of well-defined circular structures which are not visible by AFM. Although photoinduced morphological changes are not completely reversible for these aggregated structures, the photochromism of DTE-**3** is completely conserved in multilayer LS films.
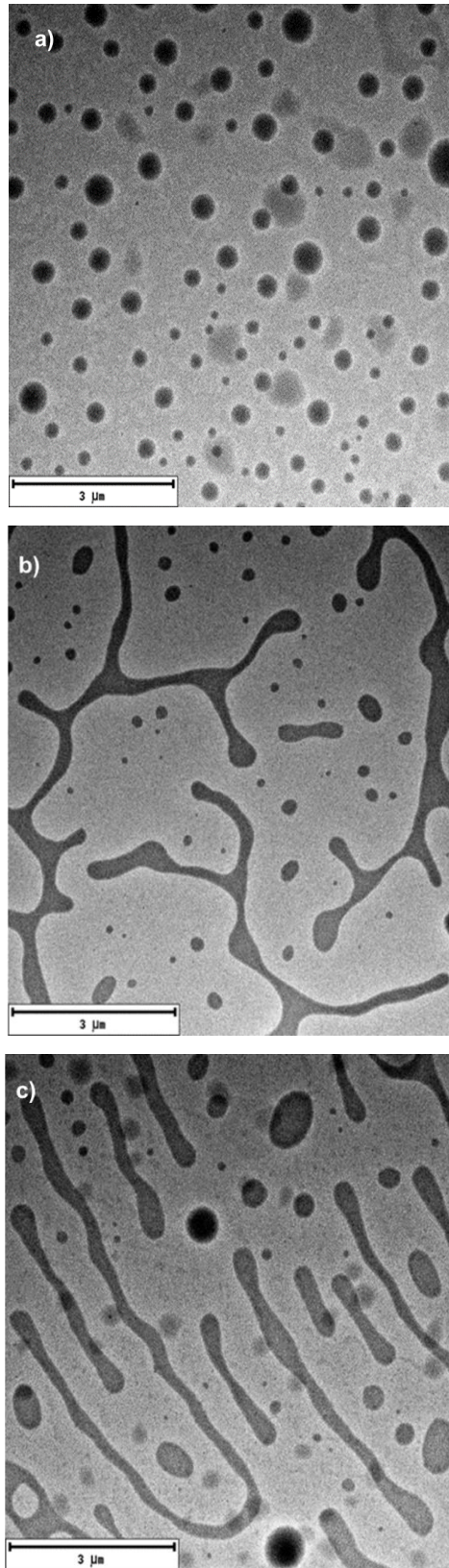
Figure 4.11: TEM images of LS films of DTE-**3** a) before any light irradiation, b) UV light irradiation (6 W UVA lamp, λ=365 nm, 6 min), and c) visible light irradiation (53 W halogen lamp, 2 min)

The resulted film formation from all DTEs was not suitable for further femtosecond electron diffraction studies. Despite the interesting behaviour of the DTEs after an on-solid irradiation, a further study of that mechanism did not occur. The proof of thin film formation as a mono- and multilayer did not meet our requirements. The insufficient sample area coverage and partial film homogeneity allowed us to study the photochromic behaviour but was not sufficient quality to explore making a molecular movie of the ring opening/closing dynamics. There was no way to control film creation on the air–water interface which resulted in void spaces and bilayer structures.

5. Vitamin B$_{12}$ (Cyanocobalamin)

5.1 Introducing vitamin B$_{12}$

Vitamin B$_{12,}$ also called cobalamin, is a water-soluble vitamin involved in the metabolism of every cell in the human body. Vitamin B$_{12}$ is the only water-soluble vitamin that can be stored by the human body for any sufficient time, with the liver being the basic storage site. It is a cofactor in DNA synthesis, as well as fatty acid and amino acid metabolism[118-121].

Vitamin B$_{12}$ belongs to a family of eight B vitamins and is the largest and the most structurally complex vitamin. The structures of vitamin B$_{12}$ and coenzyme B$_{12}$ were established using X-ray crystallography in the laboratory by DC Hodgkin[122]. The molecule structure of cobalamin is simple but contains a lot of different varieties and complexes (Fig. 5.1).
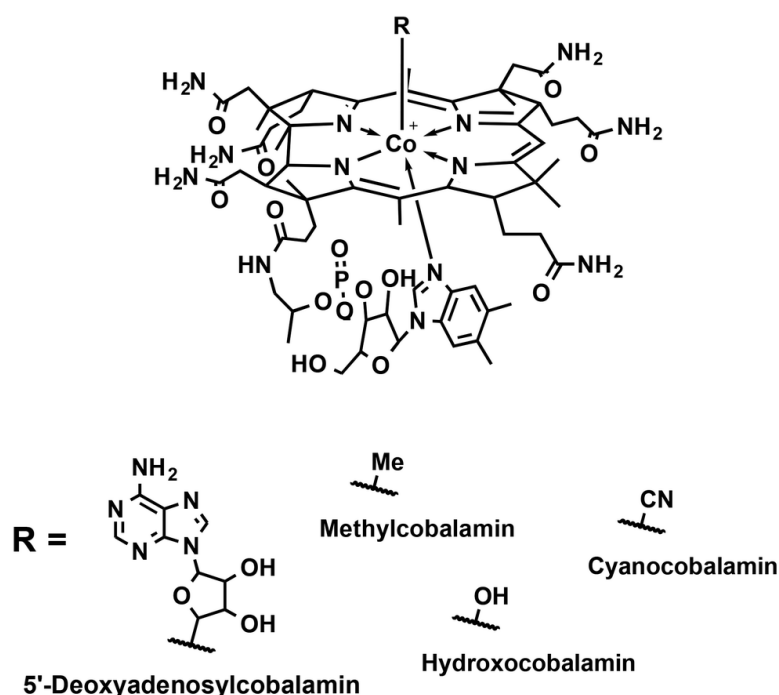

Figure 5.1: The chemical structure of vitamin B$_{12}$ (cobalamin). Figure adapted with permission form [123]

Vitamers of vitamin B$_{12}$ are good candidates for ultrafast femtosecond electron diffraction studies because of their photochemical properties. The biological functions for cobalamins include light-activated gene regulation triggered by the photolysis of the unique

Co-C bond[124]. Cyanocobalamin is known for its sensitivity to light of short wavelengths which reduces the Co^{3+} metal center[125]. Cobalamins have interesting photochemistry which is significant for the improvement of photoactivated molecular devices. This is associated with drug delivery and the enhancement of photoactive proteins dependent on vitamin B_{12} activation[126]. The C-Co bond and the corrin ring are the chemically important parts of vitamin B_{12}. The vitamer cyanocobalamin is photostable under visible light irradiation but might undergo photoaquation where the cyano ligand is replaced by water[127]. By having the opportunity to make the 'molecular movie', we would be able to observe the molecular transformations controlling the cobalamin reactivity and deactivation. However, the high solubility of cobalamin in water prevents the use of standard wet ultramicrotomy methodology in preparation of thin samples, necessitating the exploration of alternative approaches. In the first place, to minimize the dissolution of the cut sections into water, the trough solution was composed of a saturated vitamin B_{12} solution. The crystallization began on the blade, and the samples that were collected vanished or were damaged. Therefore, dry or cryo microtomy were the next tools.

In this chapter, different attempts, with different techniques for thin film sample preparation are presented. The results, with the advantages and disadvantages of each technique, will follow. The sample preparation was pursued with both 'bottom-up' and 'top-down' approaches, beginning with the compound in solution and crystalline forms, respectively. The thin film fabrication techniques used are the knife-edge technique, the spin-coating technique, dry- and cryo-ultramicrotomy, and the LB technique. The crystal softness and sensitivity, as well as the water-solubility of cyanocobalamin, brought up some technical problems that we were challenged to overcome.
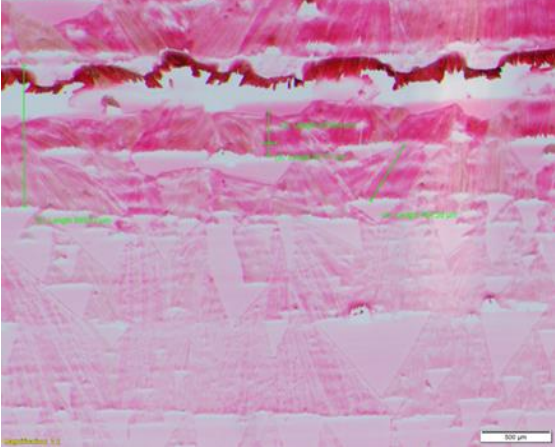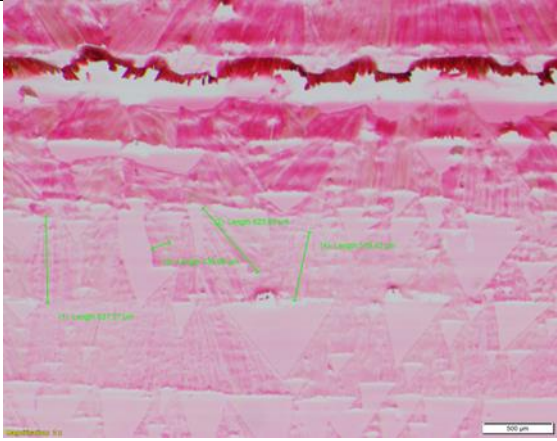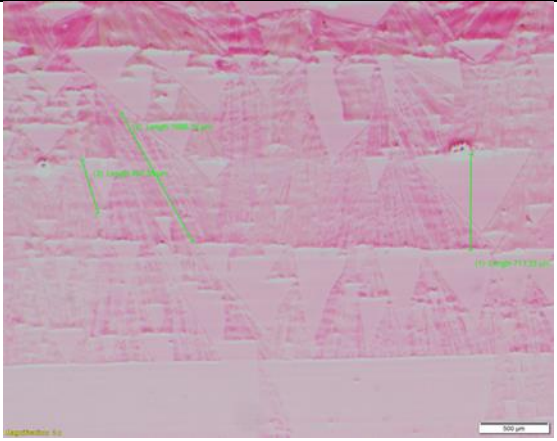
5.2 The 'knife-edge' crystallization challenges
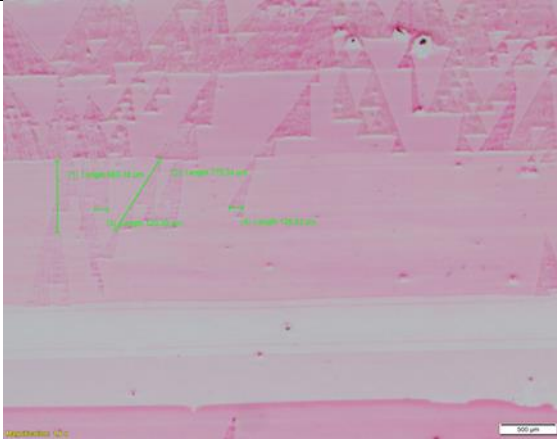
5.2.1 introduction

A major criterion for ultrafast electron diffraction is to have thin crystal films (<200 nm) in order to prevent a multiple scattering and a sufficient large area (100um x 100um) to get sufficient signal. However, there are two main difficulties along the way, the crystallization conditions and the sample transfer onto a substrate. In this chapter, the crystallization conditions as well as the sample transfer processes are described in detail.

5.2.2 Optimization of the crystallization procedure and optical characterization

The experimental conditions analysed in this chapter were already described in chapter 2.3. Table 5.1 gives a comparison of the obtained crystals' quality by varying the speed of the blade and the slide-edge height. The vitamin B_{12} concentration was chosen as 5 mg/mL and the flow rate changed occasionally (in the range of 30–60 min). High-resolution images were taken for the best possible comparison of the optimal settings. After a few attempts it turned out that, to finalize the experimental conditions, what worked the best was a preparation of a fresh solution of vitamin B_{12} in deionized water with a concentration of 5 mg/mL, stage motion speed of 1.0 µm/second, and a solution flow rate of 0.030–0.040 mL/hour. By using these conditions, there was a balance between the number of the nucleation sites and the thickness of the crystal samples. For stage speeds greater than 1.0 µm/second, the number of nucleation sites decreased, whereas for lower speeds the samples were getting thicker as measured by their light transmittance. After the conditions were set, they were kept constant for all following trials. Initially, glass slides were used as substrates but were eventually substituted by copper-coated substrates, because lifting off the glass slide was difficult without breaking the crystals.

Slide edge distance from the substrate (µm)	Speed of the motorized stage (µm/sec)	High-resolution images of crystallized B_{12}
100	0.3	

100	0.5	
100	1.0	
100	1.5	
100	2.0	

100	3.0	
150	3.0-1.0	

Table 5.1: Optical microscopy showing crystal dimensions from the knife-edge crystallization employing different stage speeds and slide-edge heights. The concentration of vitamin B_{12} was kept constant at 5 mg/mL

5.2.3 Optical characterization with atomic force microscopy

A closer look at the quality of the crystals on the glass substrate was achieved via the AFM technique. To be precise about the PMMA-B_{12} crystal thickness, the glass substrate was brought for AFM studies. In Figure 5.2, the crystal formation within the PMMA layer can be seen. The AFM height sensor (Fig. 5.3), however, revealed a thickness of a few μm, which is not within the desired thickness values.
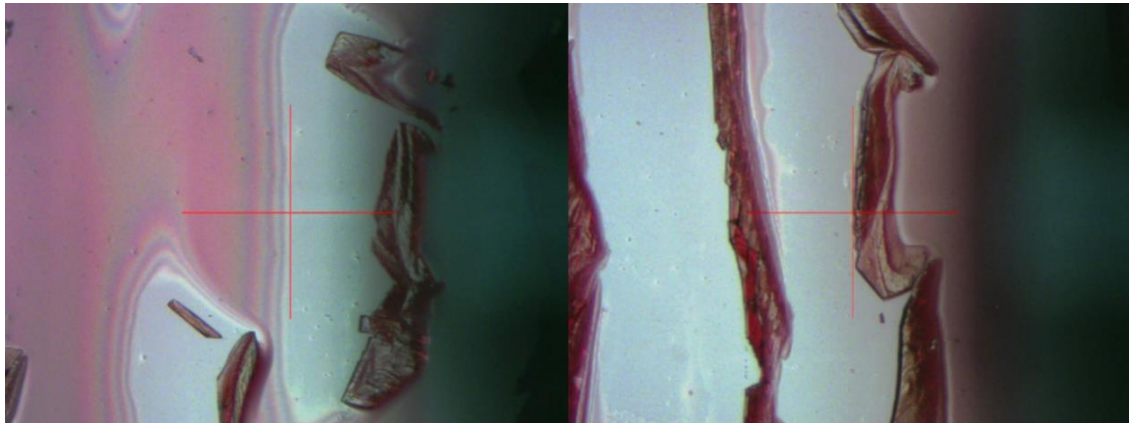
Figure 5.2: optical images of the region used in AFM. created by knife-edge crystallization with the PMMA-B_{12} sandwich on a glass substrate

Figure 5.3: AFM images revealing the film height and formation on a glass substrate

The optimum conditions were determined to be as follows: 5 mg/mL vitamin B_{12} solution in deionized water, a substrate movement speed of 1 μm/second, and a solution flow rate of 0.03–0.04 mL/hour. These were used for all consecutive trials that will be described in

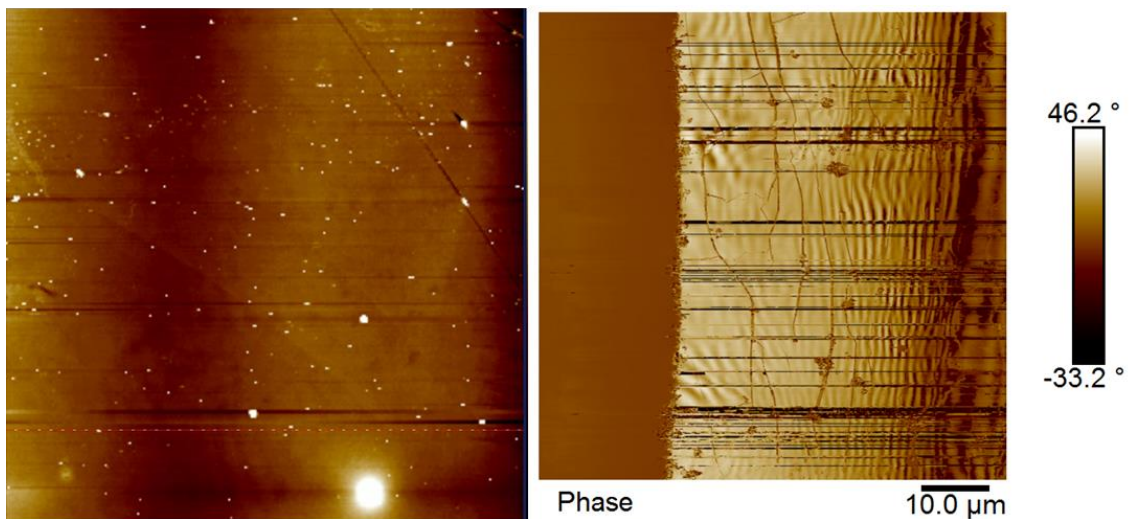this chapter. By implementing these conditions, a balance between the number of nucleation sites and apparent thickness of the crystal samples was achieved. With higher substrate speeds, the number of nucleation sites declined, while lower substrate speeds resulted in thicker samples, which were determined by the amount of light transmittance through the samples. Since the deposition on the glass substrate did not allow any further studies because the substrate did not fit into other setups or allow lift off of the crystals from its surface, an attempt to 'sandwich' B_{12} has been made which will be described in the following chapter.

5.2.4 Crystallization on the copper substrate

The idea here is to 'trap' the B_{12} crystals between PMMA layers, deposited on a movable and flexible substrate. Therefore, copper foil was used as the deposition area. The crystallization of the 'sandwiched' crystals was on top of the copper foil and then we could dispose of the substrate at any time. Although the crystal formation on top of the polymer, the dissolving of selective areas and the transfer onto the desired substrates looked easy, the removal process was a lot more difficult than expected. Therefore, the copper foil was separated carefully from the glass slide and the areas of interest were selected under the microscope. The foil was cut into small pieces with a diamond cutter and then placed carefully on the surface of the etching solution. After a waiting time of 30 minutes, the copper foil was dissolved, and only vitamin B_{12}, encapsulated by the PMMA, was floating on the surface. Prior to this step, the etching solution had to be removed to avoid contaminating the floating samples, thus making their detection more difficult (Fig. 5.4).

Step 1: A thin film created on a copper foil layer
trapped within PMMA
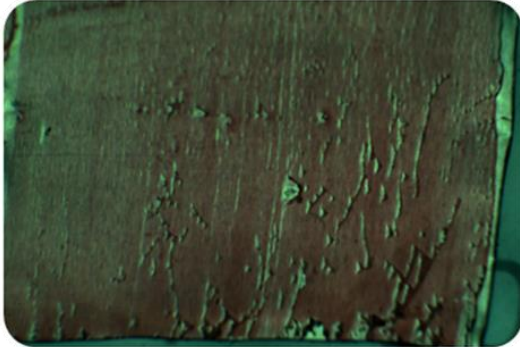
Step 2: under the optical microscope we choose the section with the optimum crystallization
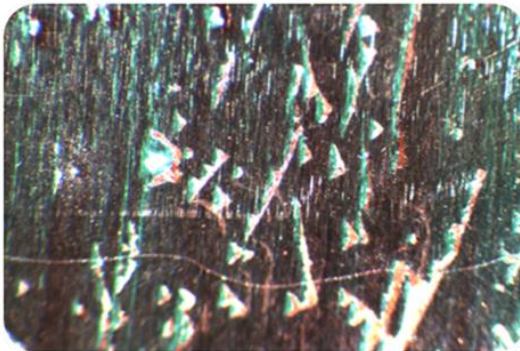
Step 3: The last step is to find the focal point and ward off the non interesting area

Step 4: All pieces are soaked into a copper etching solution ($FeCl_3$)

Step 5: After the copper is etched, we purposely dilute the solution, in order to be able to lift-off with the proper substrate the desirable section

Step 6: The lift-off operation is under the microscope for a better control

Figure 5.4: Step-by-step presentation of the sample treatment and preparation after using the knife-edge technique

5.2.4.1 Characterization with transmission electron microscopy

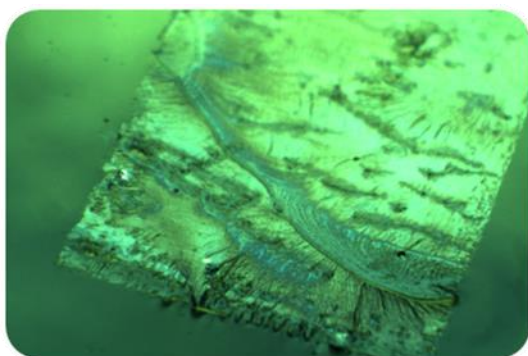In Figure 5.5, the floating membrane is visible under the light microscope before transferring it onto a TEM grid. During the transfer procedure, the TEM grid was carefully immersed into the solution in order to lift-off the membrane with the crystal. The membrane size was bigger than the size of the TEM grids so after lifting it we had to carefully dispose the part that was hanging around the grid without damaging the crystal.
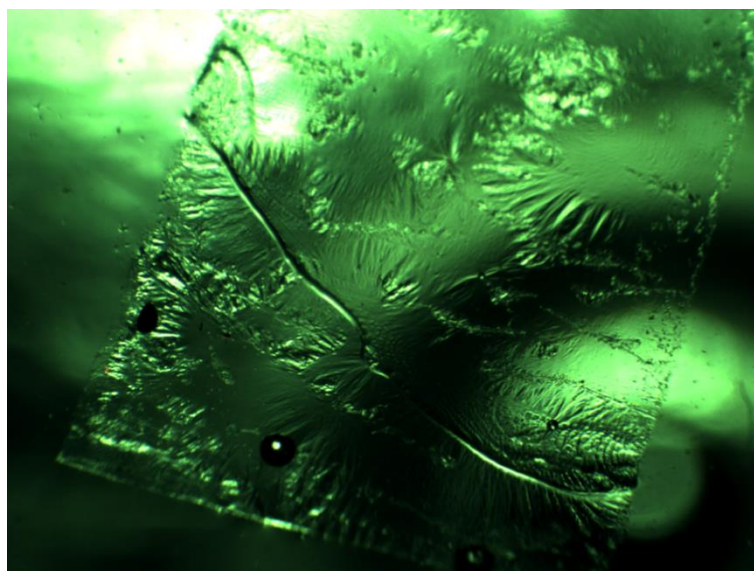

Figure 5.5: Vitamin B_{12} protected by the PMMA membrane floating on the diluted copper etchant solution right before being transferred onto a TEM grid using the 'fishing technique'

The transfer onto a TEM grid is a necessary step to further characterize the samples. Via TEM characterization, we can investigate the crystal quality of each sample.

After transferring the membrane onto a TEM grid, some real space images were collected. Unfortunately, the created film was ripped, but the two PMMA protection layers were clearly visible (Fig. 5.6). Vitamin B_{12} can be seen as small spots dispersed within the PMMA membrane layers. Electron diffraction patterns were not collected, as the sample thickness did not allow any electrons to penetrate. This was expected since the optimum PMMA thickness was 100 nm for each layer, plus 100 nm the thickness of the cyanocobalamin, which is a thick film for SAED experiments. In another case scenario, assuming that our layers are thin enough to allow electron diffraction the spots are left over from etching. This is a possibility in case our PMMA layer was not homogenously distributed and had some defects, or we created them during the whole procedure. We conclude that the knife-edge crystallization on a disposed substrate might not be the right technique for this purpose.
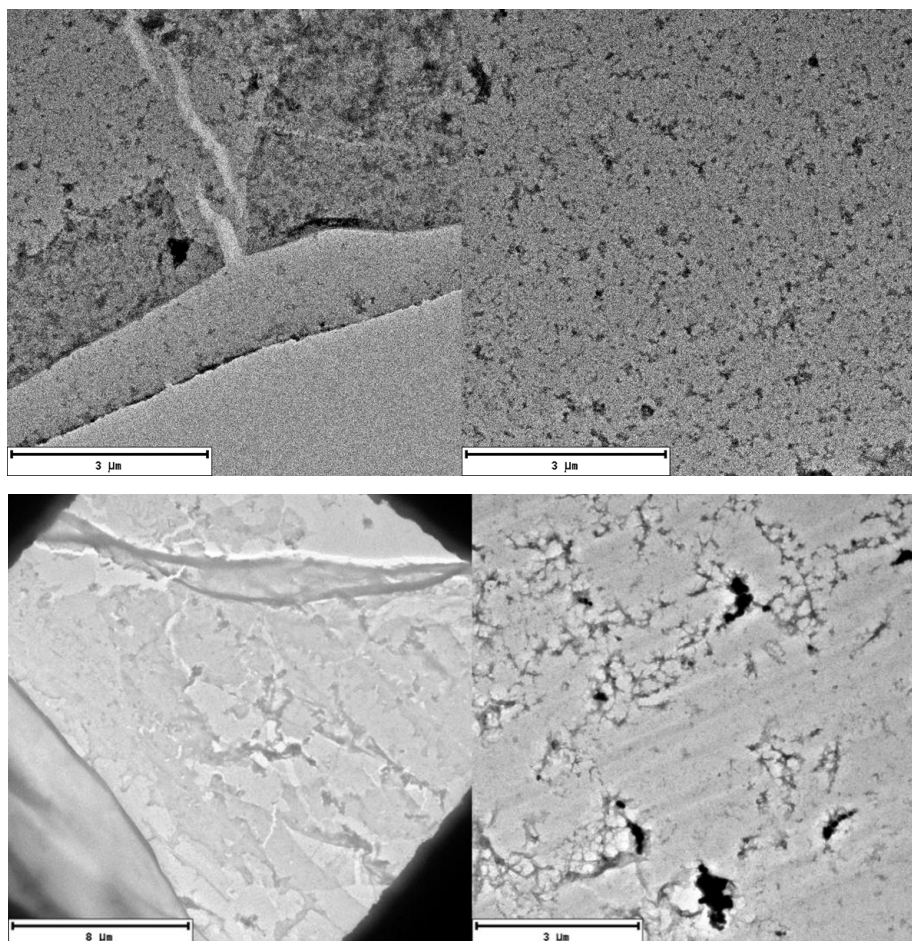

Figure 5.6: TEM real space images. Vitamin B_{12} crystals can be seen with a PMMA layer at the bottom as well as on top. SAED images were not to be obtained due to the high sample thickness

5.2.5 'Knife-edge' crystallization directly on different substrates

As described above, sample preparation on a copper-coated substrate did not bring the desired results. Hence, the next attempt was directly on the TEM substrates. During this procedure, the PMMA coverage was not necessary considering that the crystals would not need to be removed. Knife-edge crystallization was developed directly onto several types of TEM grids as well as graphene-coated layers under the optimum parameters which were previously decided. The purpose was direct crystallization on the TEM windows or the graphene-coated copper layers, thus avoiding the cumbersome and costly procedure of spin coating and copper etching. A special home-built, multi-TEM grid-holder base was kindly provided by the SSU team. The special base had grid holes on top, where the TEM grids were deposited and the crystallization took place under slow evaporation. However, none of the procedures was fruitful, as the crystals created on the TEM windows and formed under slow evaporation turned out to be very thick, making the sample unsuitable for further investigation. Comparing the differences between this and the earlier knife-edge experiment, we awaited thinner B_{12} layers due to the lack of PMMA and the absence of any chemical solutions. Concerning the graphene-coated layers, it was impossible to securely attach them onto the moving stage. Figure 5.7 shows the stage setup with the TEM substrates ready for the knife-edge crystallization. Similarly, Figure 5.8 shows the graphene-coated substrate after a crystallization process.
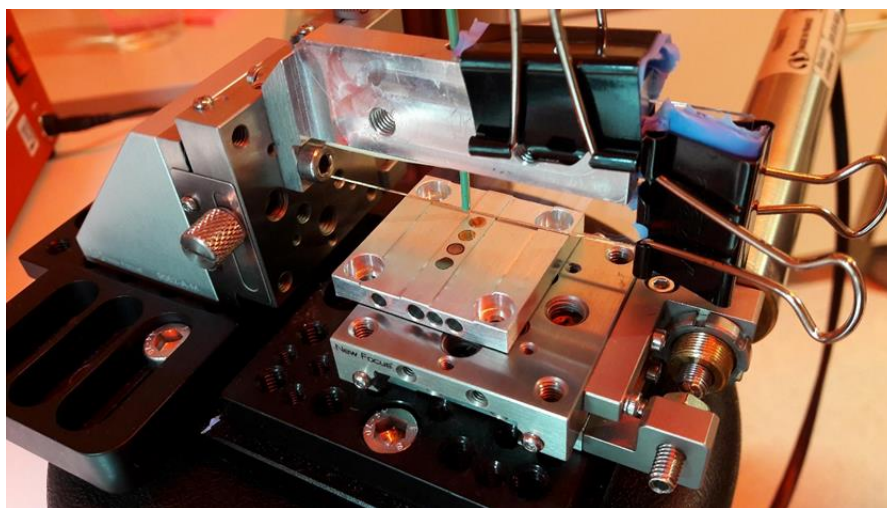

Figure 5.7: The knife-edge stage suitable for direct deposition onto TEM grids, different substrates before and after the crystallization. The obtained samples were not suitable for further characterization due to the thickness of the layer
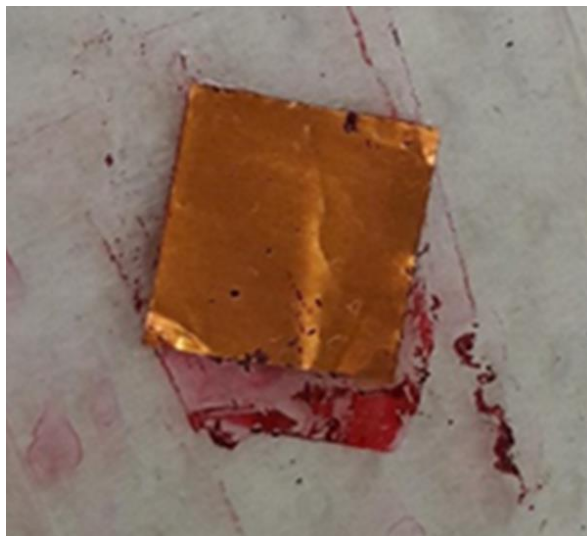
Figure 5.8: Graphene-coated substrate with a direct B$_{12}$ crystallization on top. Most of the crystallization took place around the substrate rather than on top, while during the detach procedure from the stage, the substrate got crinkled due to thickness and softness, making it inappropriate for further treatment

Despite the technique directly allowing on surface crystallization and the large area coverage, a defect of this method was the sample thickness and the substrate inflexibility. Large area coverage was successful but difficult to transfer, while the small area coverage did not allow any further characterization studies due to crystal thickness.

5.3 Dry and cryo-ultramicrotomy and characterization of B$_{12}$ crystals

Vitamin B$_{12}$ crystals prepared in-house for ultramicrotomy were used. Dry microtomy was tried first. A major advantage of dry microtomy is that it does not need a trough solution, so the sections are not dissolved. The cut sections were stuck on the knife blade, so the TEM grid needed to be attached directly on the blade, where the crystals were collected. Sections having a thickness of 100 nm cut, though they were not deposited plainly onto the grid. Probably the crystals were not strong enough to withstand the pressure of the knife. Looking for an alternative frozen sections appeared appealing and promising.

Cryomicrotomy is a widely used tool for biological and histological samples, which are softer, fragile, and difficult to cut under ambient conditions. Thin sections of 100 and 150 nm thick were cut under liquid nitrogen (LN) flow at -140 °C. The section quality was slightly better

than those derived from dry microtomy according to optical characterization under the microscope. Instead of the loop, carbon-coated grids were gently touching the knife blade for a direct sample deposition. The grids were kept under frigid conditions (-20 °C) to avoid sample fatigue coming from a thermal shock. The deposited samples were then allowed to warm up to ambient temperature but due to the softness of the crystal, the sections were sticking to each other (Fig. 5.9). Each section crinkled, making the deposition effort more difficult. However, the obtained sections were thin enough to allow some data collection. TEM patterns were collected under ambient conditions without cryo cooling or cryo transferring the samples, even though the samples were stored at -20 °C.

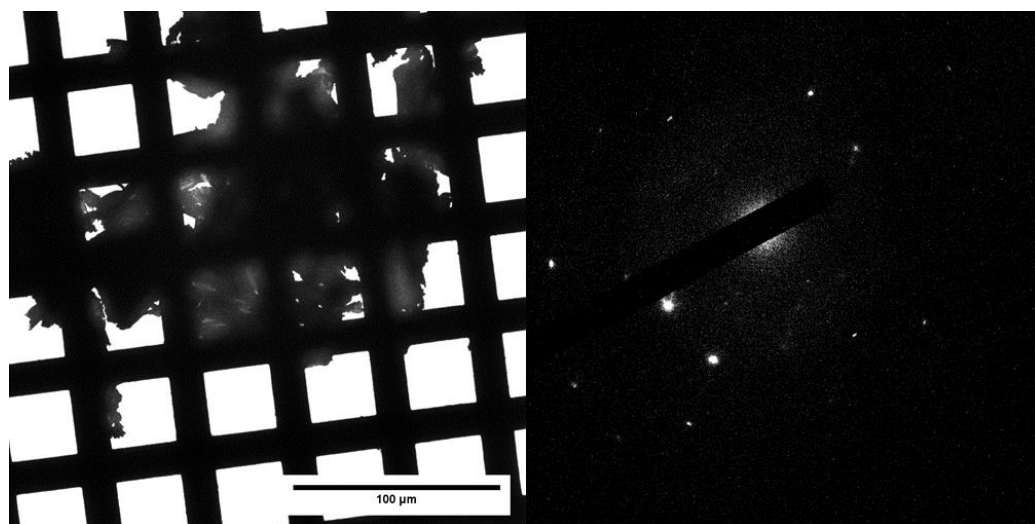Figure 5.9: Vitamin B_{12} sections after cryomicrotomy onto a copper TEM grid (left), and the corresponding diffraction pattern (right)

Nevertheless, the sample thickness could be easily controlled with the ultramicrotomy technique, but the deposition and the large area coverage on the substrate were not easy to control. The crystal softness made them easily damaged and there was a structural distortion in the dry-cut thin-films.

5.4 Langmuir films of vitamin B$_{12}$

As previously reported, vitamin B$_{12}$ derivatives are hydrophilic. Furthermore, the stable preservation of the vitamin B$_{12}$ derivatives in lipid assemblies is essential to achieve successful catalysis. Incorporation of the vitamin B$_{12}$ derivatives from the aqueous phase to lipid bilayers has been investigated by gel-filtration chromatography and electronic spectroscopy[128, 129]. Even though the obtained information is crucial for stable immobilization of the vitamin B$_{12}$ derivatives in the hydrophilic environment formed by the artificial bilayers, the partition experiments give only information about the total amount of the incorporation.

The common methods involve the formation of B$_{12}$ derivatives after the functionalization of the vitamin molecules with different treatment procedures while mixing them with DPPC lipids. As a result, their floating on the air–water interface creates mono- or bi-layers of lipids, with B$_{12}$ molecules embedded as a stable LB film. In a different approach of reduced dimensionality, the Langmuir–Blodgett technique was implemented to bring B$_{12}$ into a bi-dimensional frame. Therefore, the mixing behaviour and the transfer properties on a solid support of Vitamin B$_{12}$ without any further functionalization into a Langmuir monolayer of dipalmitoylphosphatidylcholine (DPPC)[130, 131] were investigated (Fig. 5.10).
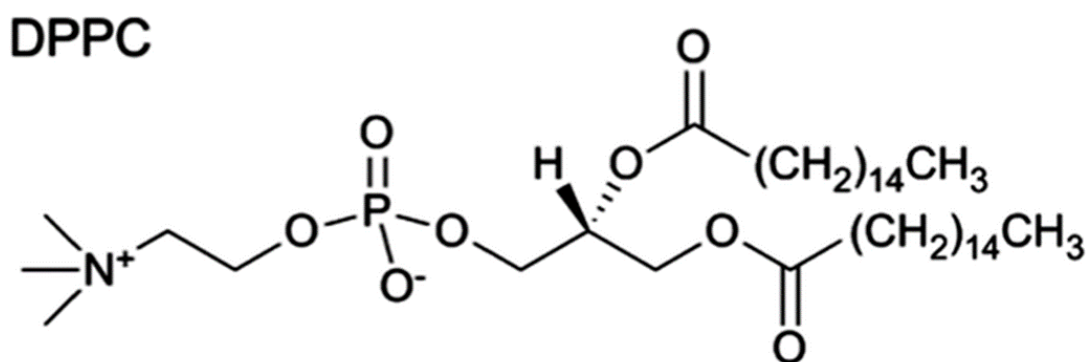
Figure 5.10: DPPC is a phospholipid with two 16-carbon saturated chains and a phosphate group with a quaternary amine group attached. Figure adapted with permission form [132]

When added to water, most commonly double-chain amphiphiles form bilayers. Those spherical bilayers enclosing an aqueous cell are called vesicles or liposomes[130, 131]. The formation of these structures represents aggregates formed by a physical process[130, 131]. These aggregates, when mixed with vitamin B$_{12}$, are considered to interact as protection spheres where the vitamin molecules are enclosed. DPPC is not expected to have any other specific reaction with vitamin B$_{12}$, and therefore their mixed behavioural analysis would offer

general information and insight into how the vitamin molecules can be organized as a Langmuir film.

5.3.1 LB isotherms

In principle, close packed monolayers are formed as large patches of ultrathin solid material when they are compressed. There was no change in the surface pressure when the trough area was above 120 cm^2, whereas a maximum surface pressure was reached when the area was 75–85 cm^2. Additionally, concerning stock solution volumes less than 120 μL, there was no change in the surface pressure. This indicates that the total area of the transferred material was less than 75 cm^2. For a volume greater than 120 μL, an irreversible collapse of the Langmuir film was observed. Hypothesizing that the assembly of **1** (B$_{12}$ + DPPC) and **2** (DPPC) films is dependent on their molecular structure, the differences in structure are expressed by relative differences in the surface pressure-area isotherms and changes in the final surface pressures.

The isotherms of the mixed monolayer **1** (B$_{12}$ + DPPC) and the phospholipid **2** (DPPC) are compared in Figure 5.11.
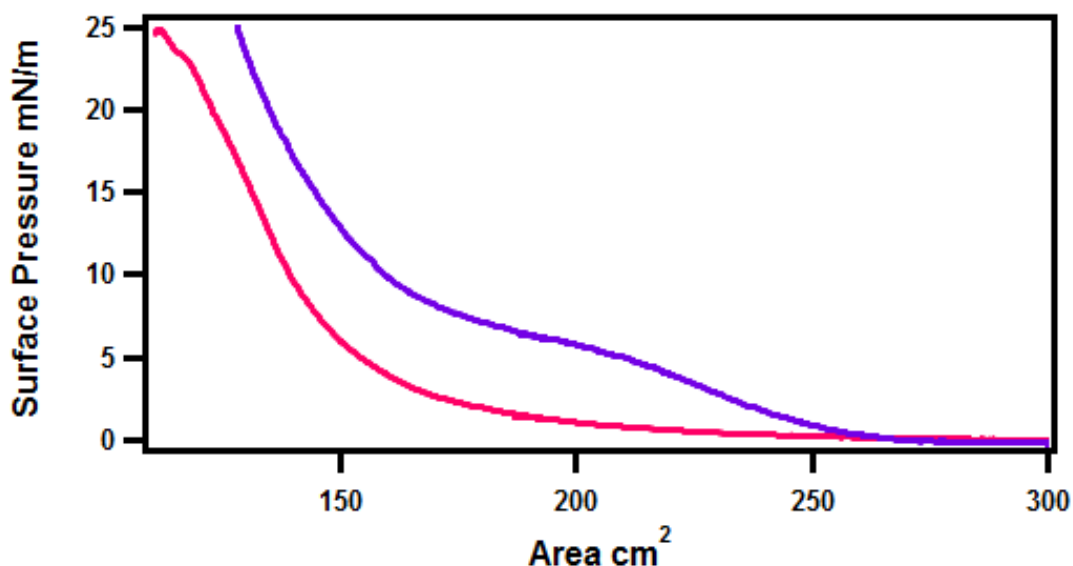

Figure 5.11: Surface pressure-area (π-A) isotherms of mixed monolayer of the vitamin B$_{12}$ + DPPC (**1**) (pink) and DPPC (**2**) (purple), respectively, on pure water at ambient temperature

This set represents two different isotherms: mixture DPPC/B$_{12}$ (pink isotherm, **1**) and pure DPPC (purple isotherm, **2**) deposited on the Langmuir aqueous subphase. While

compression of the trough barriers occurs concerning the isotherm of **(2)** (DPPC) first signs of a Langmuir film formation appear at 260 cm^2, no change is observed for the isotherm **(1)** (B$_{12}$/DPPC). From that point on, **(2)** (DPPC) exhibits the typical isotherm pattern that one should expect, switching between all expected phases up to the final formation of a DPPC Langmuir film, reaching saturation at pressure values of approximately 25 mN/m. Considering the isotherm of **(1)** (B$_{12}$/DPPC), this one follows a similar pattern to that of **(2)** (DPPC) but appears to be smoother, while the first pressure increase is demonstrated at 200 cm^2 and saturation is achieved at approximately the same pressure values as in **(2)** (DPPC). This difference in the two isotherms should be attributed to the existence of B$_{12}$ in the DPPC mixture. DPPC lipids are known to form bilayers when implementing Langmuir–Blodgett film formation technique[130, 131]. The hypothesis is that, upon mixing the two components, lipid molecules form vesicles that have the vitamin molecules embedded within them. These formations lead to a decrease in the free surface area that initially DPPC molecules occupy on the trough, as they are attracted by and attached around B$_{12}$ molecules, a fact that explains the delay in pressure rise in the case of **(1)** (B$_{12}$/DPPC).

5.3.2 Morphological investigation via atomic force microscopy

To be able to qualify the film morphology, thickness and nanoparticle distribution Atomic Force Microscopy had to be implemented. Two different LS films were obtained, DPPC (diluted in benzene) and a mixture of B$_{12}$/DPPC in benzene (1:5 v/v ratio) to examine the embedding of a B$_{12}$ film within a DPPC monolayer through potential morphological differences. There were no attempts made to produce a free standing B$_{12}$ monolayer as this has been shown not to form LB films without further functionalization[130, 131].
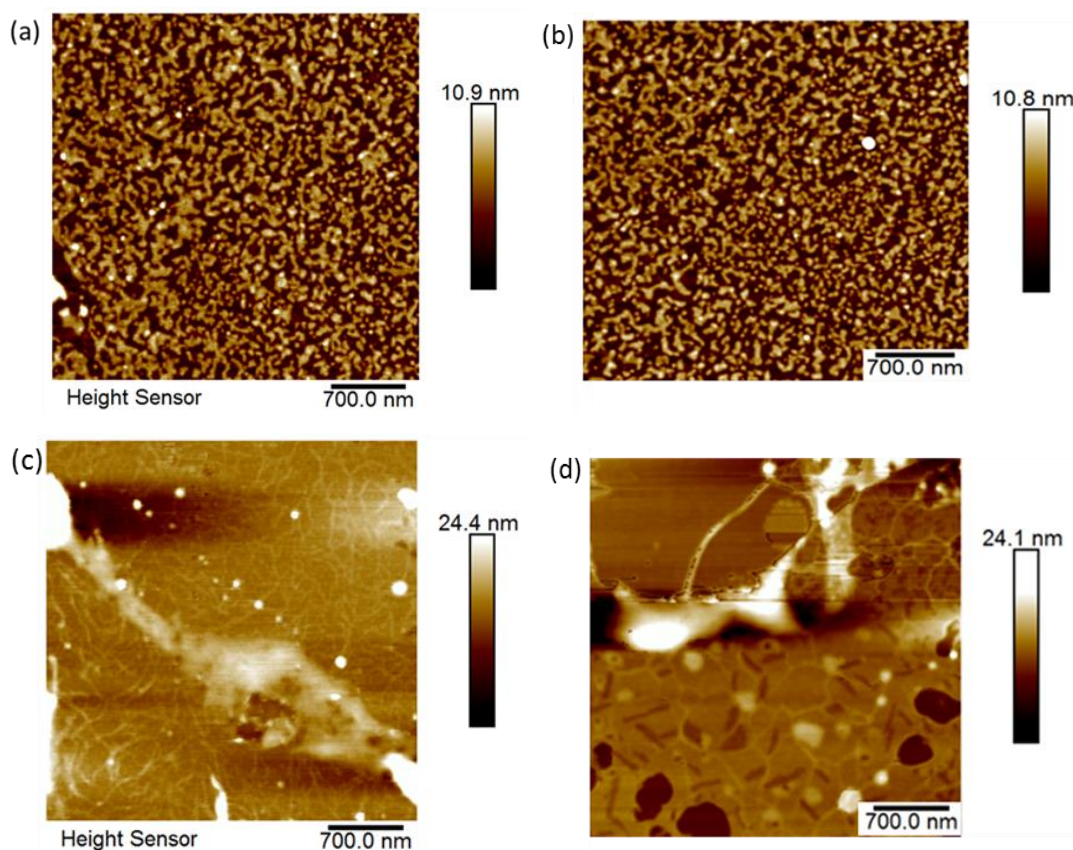
Figure 5.12: images (a) and (b) DPPC Langmuir film single deposition and images (c) and (d) B_{12} embedded in DPPC Langmuir film single deposition at a surface pressure 25 mN/m on a silicon substrate and room temperature

The AFM studies revealed the formation of continuous and homogenous LS films in both samples (Fig. 5.12). The flakes of sample **1** appear to be composed of nano-rings and nano grains with a mean diameter of 240 nm and 233 nm respectively in the case of nano-rings, and 86 nm and 80 nm respectively in the case of nano-grains. The average Langmuir film height for the cases **1** and **2** is 3,9 nm and 3,6 nm (slightly reduced for the B_{12} in DPPC Langmuir film) respectively. This observation is in agreement with the obtained TEM images (5.3.3) and is supportive of our scenario, according to which there is no formation of DPPC monolayer during the LB technique but a bilayer instead (unlike what has been reported in the past[130, 131]) and the B_{12} is embedded within the lipid molecules. This results in a slight decrease in the monolayer thickness, an observation which calls for further investigation. Notably, in performing the LB trials using just B_{12} in benzene, no monolayer was formed, as confirmed by AFM measurements and failure to measure the LB isotherm for the same system. This led to

the other conclusion that, without further functionalization of B_{12}, the only way to obtain a vitamin B_{12} film would be via a lipid such as DPPC.

5.3.2 LB-B_{12} film transmission electron microscopy studies

To further characterize the morphological differences between films (**1**) and (**2**) transmission electron microscopy and selected area electron diffraction were used. Single depositions of (**1**) (B_{12}/DPPC) and (**2**) (DPPC) were performed on silicon nitride substrates via the Langmuir–Schaefer (LS) horizontal dipping method. The TEM images give evidence of a continuous film (Fig. 5.13). The film is homogeneous and contains partially large or smaller aggregates. We hypothesize that these large aggregates, as well as the large void spaces between them, are responsible for the significant increase in surface pressure observed for the compression isotherm of (**1**) (B_{12}/DPPC) and (**2**) (DPPC). In case of (**1**) (B_{12}/DPPC), we can clearly observe spherical structures that correlate to the shape of DPPC vesicles and which contain B_{12} molecules. Furthermore, selected area diffraction of (**1**) (B_{12}/DPPC) exhibited a typical dot-pattern which proved that the obtained Langmuir film of (**1**) (B_{12}/DPPC) is polynanocrystalline. This diffraction pattern is a representative pattern formed by diffracting from mostly a single flake with minor overlap from others. The broad, diffuse rings are indicative of the scattering from the silicon nitride window. This clearly shows that a Langmuir crystalline film of B_{12} is formed within a bilayer of DPPC vesicles, and that it is thin enough for diffraction studies. Notably, for comparison reasons, single deposited DPPC Langmuir films (**2**) (DPPC) on silicon nitride windows did not diffract under the TEM beam.
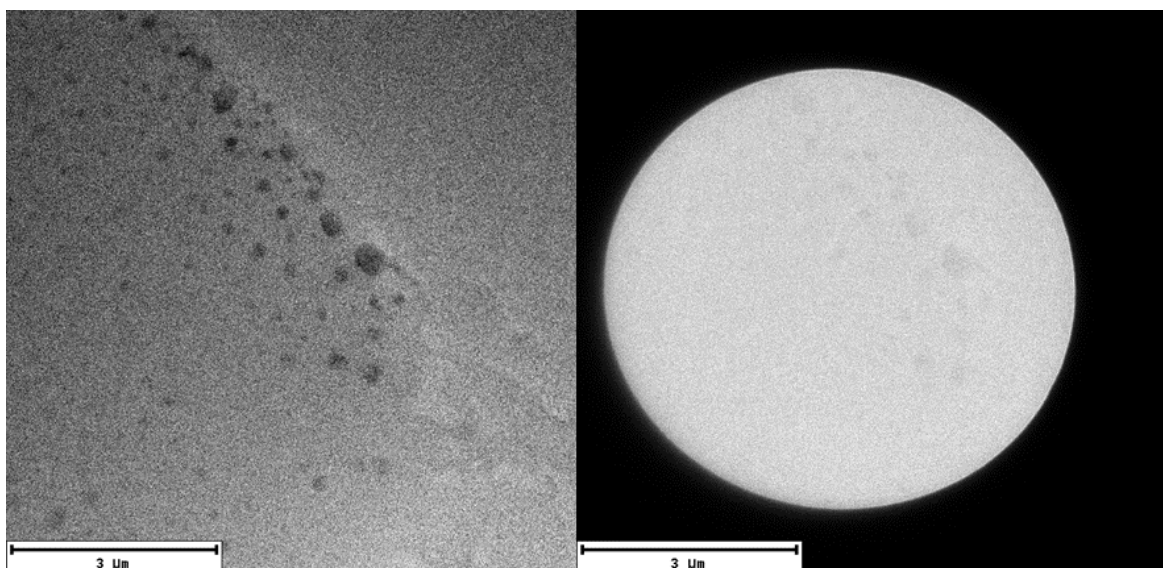
Figure 5.13: Real space imaging of **1** (B_{12}/DPPC) for a single deposition at surface pressure 25 mN/m
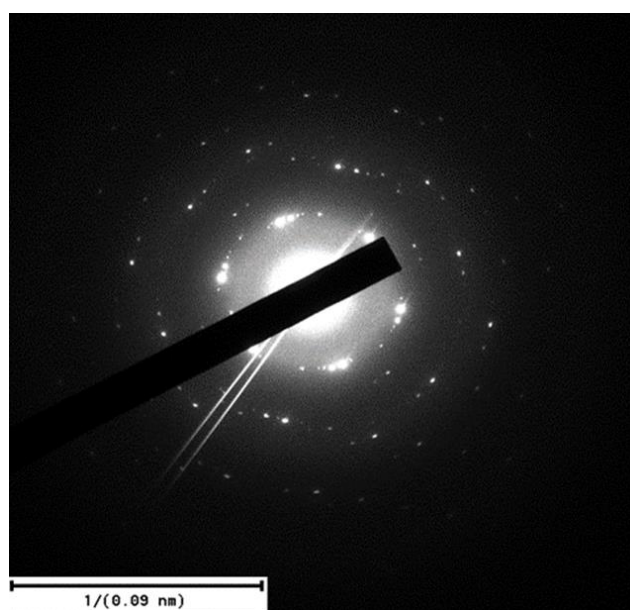
Figure 5.14: SAED pattern of **1** (B_{12}/DPPC)
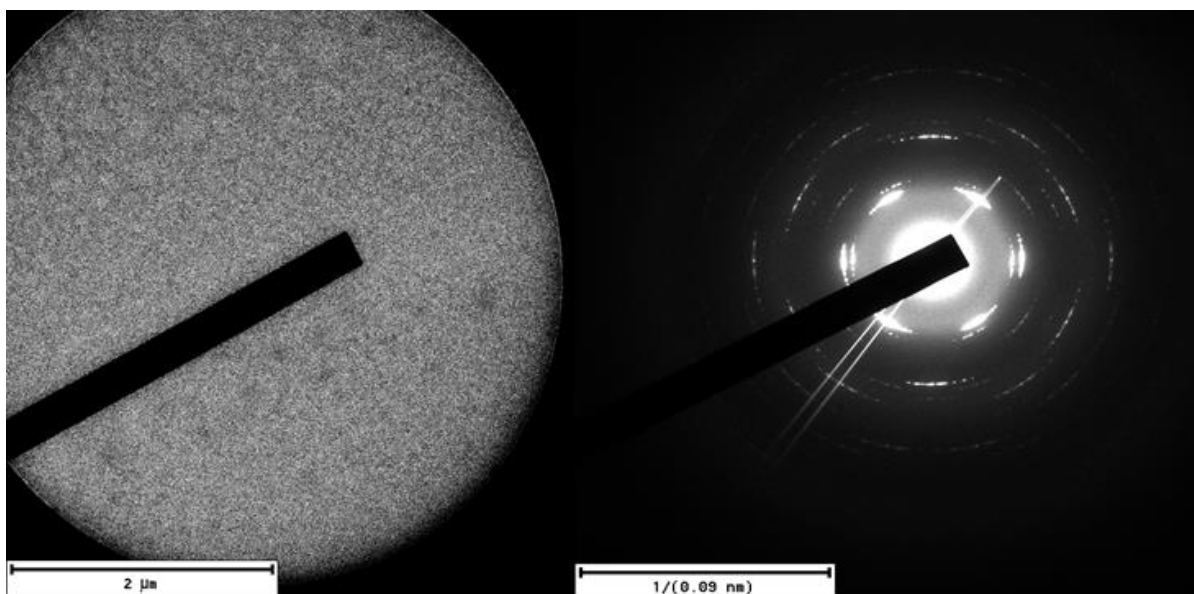
Figure 5.15: Real space image and SAED pattern of **1**

The cyanocobalamin LB-film formation would need some more improvement for further electron diffraction studies. Homogenous large area coverage can result in thicknesses remarkably close to the atomic scale, making the created films promising candidates for femtosecond electron diffraction studies. However, the technique cannot be considered repetitive and precise. The water solubility of cyanocobalamin is a major disadvantage for the LB technique. A promising film formation in the air–water interface would need the functionalization of the vitamin B_{12}.

6. Conclusions and outlook

The primary objective of this dissertation was the development and characterization of various thin films with the overall aim to develop general methods and techniques for fabricating samples that are suitable for time resolved electron diffraction studies, thereby obtaining a 'molecular movie' of the structural changes, which allows the determination of atomically resolved structure–function correlations. Systems such as metal–organic frameworks (MOFs), dithienylethenes (DTEs), and vitamin B_{12} were studied with various instruments and methods for their potential as electron diffraction compatible samples. A multitude of experimental techniques and characterization methods have been used including atomic force microscopy (AFM), transmission electron microscopy (TEM), ultraviolet-visible spectroscopy (UV-Vis), and X-ray photoelectron spectroscopy (XPS). For sample preparation and fabrication, the author focused on the Langmuir–Blodgett technique, on the knife-edge technique, ultramicrotomy, and spin coating. The major challenge posed by the objective of the thesis was the creation of sufficiently large-area single crystals compatible with fs electron diffraction studies. The electron diffraction measurements presented in this thesis were performed using a transmission electron microscope (TEM) where the sample area is not a problem due to the smaller beam size and higher electron beam currents. The samples were mostly mounted on standard TEM meshes and the diffraction patterns showed single crystalline structures for almost every sample.

Summary of the achievements of this thesis work.

Part 1: Metal–organic frameworks (MOFs), or for the purpose of FED studies, surface-mounted metal–organic frameworks (SURMOFs) were fabricated using the LB technique. To obtain SURMOF systems, MOF film architectures were deposited on substrates, ideally in a dense homogenous and oriented fashion. First, standard LB isotherms were collected and revealed the formation of a MOF nanosheet at the air-liquid interface. To create a standard and reproducible assembly protocol, many diffusion trials were done, and the reactant solutions were studied. In the case of the MOF growth with $CuCl_2$ as a metallic precursor and H_3BTC as an organic linker the chemical reaction was successful, whereas when $Cu(NO_3)_2$ was used as a metallic source there was no sign of a rapid on-surface chemical reaction. The most

crucial step in the film assembly process was the interfacial coordinative reaction, which occurs immediately after spreading the solution containing the linkers on the surface of the solution containing the metal joints. In order to prove the formation of the monolayer on a solid surface, XPS studies were performed to reveal the elemental composition of the fabricated samples and/or the unreacted features. In case of multilayer depositions at ambient conditions, the deposition process was followed by UV-Vis spectroscopy, which gave direct information about the successful fabrication of the multilayers. In order to assess the applicability of these systems for electron diffraction studies, AFM and TEM techniques were implemented to characterize the monolayers formed on the solid surfaces in terms of their morphology, thickness and crystallinity. The author provides TEM diffraction patterns and AFM images of LB-SURMOFs here for the first time, and hence there are no published results in the literature for comparison. The results revealed a rather poor surface coverage which do not meet the requirement for FED applications. However, the technique used proved to produce much better results than the conventional solvothermal synthetic techniques. The study of the formation of the Cu-BTC MOF nanosheets at the air/liquid interface has shown that crystalline sheets can form in ambient temperature and rather short waiting times. Apart from the composition and surface area, there is another structural aspect to discuss. High surface pressure results in assembly of the created crystalline domains, leading to an increased surface coverage. The large surface areas have correspondingly larger surface energies, resulting in significantly reduced stability as compared to MOFs with small surface areas.

Regarding future work, some further optimization of the experimental procedure, controlling conditions, and/or choice of MOF metal precursors and ligands could allow for producing systems with larger surface areas which could meet the requirements for time resolved electron diffraction studies. Ligands with a bigger planar geometry could provide a larger surface coverage and more stability. Another key to MOF film formation is having LB monitoring capabilities. For instance, to monitor the film growth on the LB surface with an imaging system such as Brewster Angle Microscopy (BAM), could lead to major improvements. This would allow one to monitor the MOF film formation closely. Observing the film compression and decompression mechanism can also provide additional insight into the film dynamics. Concluding this part, the films obtained holds promise for potentially meeting the

sample requirements for femtosecond electron diffraction studies. As possible next steps the author considers the incorporation of guest–host molecules into the MOF crystals.

Part 2: In this part a new amphiphilic DTE concept, which has been synthesized and characterized for its photochromism in an organic solution, was studied. The main goal here, as in the first part, was the fabrication and the complete characterization of molecular systems that could be good candidates for fs electron diffraction experiments. A better insight into these newly synthesized DTEs and their photochromic properties in the solid phase is also of great interest and was characterized as part of this thesis.

Monolayers of three different DTEs (**1–3**) were prepared and surface pressure-area (π-A) isotherms were recorded under different irradiation conditions. Langmuir films of **1** and **2** DTEs showed reproducible increase and decrease in surface pressure after UV and visible light irradiation. In comparison, only the cycloreversion of **3c** led to a further increase in the surface pressure of the Langmuir film under the same irradiation conditions as for the first two DTEs. AFM and TEM studies showed that the morphological changes of DTEs **1** and **2** were of a reversible nature which were in agreement with the surface-pressure results. The AFM and TEM images also showed that **3o** forms spherical aggregates. Moreover, the surface changes of **3o** appearing from spherical structures into worm-like structures shows that it undergoes a photoinduced change in morphology. A closer comparison of the AFM and TEM images showed that under visible irradiation the **3c** derivative leads to the formation of larger aggregates at the beginning according to AFM images, and there is evidence of a reversible change in morphology according to the TEM images. These larger aggregates could have been the reason for a significant increase in the surface pressure observed for the compression isotherm of **3**. Another hypothesis is that incomplete cycloreversion impedes the re-formation of smaller spherical structures observed for **3o**. Regardless of these photoinduced morphological changes, the photoisomerization of **3** was completely reversible as single-component multilayer thin films upon direct UV or visible light irradiation. Multilayered depositions did not reveal any film changes during the irradiation processes. The crystallinity of these systems was confirmed by high quality diffraction patterns. Unfortunately, the available sample area of interest was not sufficient for performing more detailed investigations. As an overall conclusion of part 2, the films created from all DTEs exhibited

thicknesses of a few nanometres, but the insufficient area coverage did not allow us to perform further electron diffraction studies.

For further investigations, the DTE derivatives in the crystal form will be cut using the ultramicrotome technique and eventually will be used for femtosecond electron diffraction studies.

Part 3: In this last part, the work was focused on the formation of B_{12} nanoscale thin films to be studied using fs electron diffraction studies. The goal was the creation of thin crystals with large surface areas in order to prevent multiple electron scattering and allow for a sufficiently large signal in FED studies. After testing a series of thin film deposition methods including the pioneering 'knife-edge' crystallization method, spin coating and ultramicrotomy, the Langmuir–Blodgett/Schaefer experimental technique turned out to be the best choice. The knife-edge crystallization method proved an excellent tool for achieving a large sample area coverage, but the sample transfer turned out to be challenging. Owing to the dissatisfactory results achieved by the knife-edge method, we turned our attention to ultramicrotomy (both dry and cryo). With both ultramicrotomy techniques, the crystals turned out to be too soft to withstand the knife pressure, making transfer of any successfully cut crystals without further damage to be impossible. As already stated, the Langmuir-Blodgett technique turned out to be a more successful method for the sample preparation. The fabricated Langmuir films were easily transferred through horizontal deposition on various substrates via the Langmuir–Schaefer (LS) deposition. Standard surface pressure-area isotherms showed a substantial difference in the structure and packing of pure DPPC and mixture B_{12}/DPPC. AFM imaging indicated that homogenous films were obtained in both cases, and that the slightly reduced thickness and particle diameter in the case of the mixture gave a strong hint of the embedding of the vitamin within the lipid vesicles. Furthermore, TEM imaging backed up these assumptions. SAED proved the nanocrystalline nature of the obtained B_{12}/DPPC Langmuir film, indicating a collection of crystalline domains. These results also proved that the formation of 2D films of B_{12} embedded in DPPC lipid is sustainable without further functionalization of the vitamin and showed that the vast majority of the obtained films were true bi-dimensional films with small within-error variations in thickness. A conclusion of the last part of this thesis is that the film creation with the traditional and most

common techniques were fruitless, as opposed to the LB technique which provided much better results. The vitamin B_{12} project was the most complicated. The water-solubility of cyanocobalamin rendered our attempts at a film formation unsuccessful. The crystal softness and sensitivity made the samples difficult to handle without damaging them. As a result, the film homogeneity, the area coverage, and thickness did not meet our expectations.

Future work will focus on the functionalization of the cyanocobalamin molecule, so as to be hydrophobic. Also, a cluster ion beam setup for polishing the surface of the crystals and the thin films will be introduced.

To summarize, in this thesis several thin film systems were fabricated and characterized and their compatibility with FED experiments was investigated. The main method for fabricating ultrathin films was the Langmuir–Blodgett method (LB) which proved to allow fabricating films of larger homogeneity and uniformity compared to the other conventional techniques. None of the other fabrication techniques presented here has achieved the same thickness and quality. Nevertheless, there were also a few limitations in the preparation method of LB monolayers and multilayers. Temperature, surface pressure, surface molecules overlapping, and transfer rate all play a key role in achieving a successful monolayer deposition, and sufficiently precise control of these parameters to assure reproducibility was difficult to achieve. Regarding the other techniques, the knife-edge technique, presented some limitations due to its recent invention and limited studies of parameters. Blading techniques are usually used for production of films in the micrometre thickness range. Despite the large area coverages, the substrate limitations and the sample complications impaired the success of our efforts. However, it is possible to improve the results by adjusting the blade height and the stage flexibility for different substrates. Finally, the spin-coating technique and ultramicrotomy, which are traditional techniques for fabricating thin films, revealed several well-known disadvantages. More precisely, the samples fabricated with spin coating present some characteristic defects such as air bubbles within the resist film. In case of microtomy, it was difficult to find the right crystal orientation which needs to be aligned perfectly parallel to the knife. In case of poor alignment, the sections cut from the sample fail to yield continuous films. All these results suggest that the LB technique is the technique best suited for the current purpose as confirmed by AFM and TEM techniques.

The electron diffraction patterns in particular revealed superior crystallinity, making these films promising candidates for time resolved electron diffraction studies. Future research should seek to overcome the remaining fabrication limitations enumerated above.

7. References

1.   Sciaini, G., Miller, R. J. Dwayne, *Femtosecond electron diffraction: heralding the era of atomically resolved dynamics.* Reports on Progress in Physics, 2011. **74**(9): p. 096101.

2.   Hildebrandt, G., *The Discovery of the Diffraction of X-rays in Crystals — A Historical Review.* Crystal Research and Technology, 1993. **28**(6): p. 747-766.

3.   Eckert, M., *Max von Laue and the discovery of X-ray diffraction in 1912.* Annalen der Physik, 2012. **524**(5): p. A83-A85.

4.   Miller, R.J.D., et al., `Making the molecular movie': first frames.* Acta Crystallographica Section A, 2010. **66**(2): p. 137-156.

5.   Dwyer, J.R., et al., *Femtosecond electron diffraction: 'making the molecular movie'.* Philos Trans A Math Phys Eng Sci, 2006. **364**(1840): p. 741-78.

6.   Ischenko, A.A., P.M. Weber, and R.J.D. Miller, *Capturing Chemistry in Action with Electrons: Realization of Atomically Resolved Reaction Dynamics.* Chemical Reviews, 2017. **117**(16): p. 11066-11124.

7.   Siwick, B.J., et al., *An Atomic-Level View of Melting Using Femtosecond Electron Diffraction.* Science, 2003. **302**(5649): p. 1382-1385.

8.   Eichberger, M., et al., *Sample preparation methods for femtosecond electron diffraction experiments.* Ultramicroscopy, 2013. **127**: p. 9-13.

9.   Thompson, R.F., et al., *An introduction to sample preparation and imaging by cryo-electron microscopy for structural biology.* Methods, 2016. **100**: p. 3-15.

10.   Jeanne Ayache, L.B., Jacqueline Boumendil, Gabrielle Ehret, Daniele Laub *Sample Preparation Handbook for Transmission Electron Microscopy Techniques.* Springer New York Dordrecht Heidelberg London, 2010.

11.   Dwyer, J.R., et al., *Experimental basics for femtosecond electron diffraction studies.* Journal of Modern Optics, 2007. **54**(7): p. 923-942.

12.   Morrell, W.E., *The experimental basis for the study of atomic structure.* Journal of Chemical Education, 1948. **25**(10): p. 551.

13.   Roberts, G., *Langmuir-Blodgett Films.* Springer Science + Business Media New York 1990.

14.   Hodge, P. and N.B. McKeown, *Langmuir—Blodgett films*, in *Principles and Applications of Nonlinear Optical Materials*, R.W. Munn and C.N. Ironside, Editors. 1993, Springer Netherlands: Dordrecht. p. 226-249.

15. Kuhn, H., *Present status and future prospects of Langmuir-Blodgett film research* Thin solid films, 1989. **178**: p. 1-16.

16. Tredgold, R.H., *The physics of Langmuir-Blodgett films.* Reports on Progress in Physics, 1987. **50**(12): p. 1609-1656.

17. de Gennes, P.G., *Deposition of Langmuir-Blodgett layers.* Colloid and Polymer Science, 1986. **264**(5): p. 463-465.

18. Kaganer, V.M., H. Möhwald, and P. Dutta, *Structure and phase transitions in Langmuir monolayers.* Reviews of Modern Physics, 1999. **71**(3): p. 779-819.

19. Niinivaara, E., et al., *Parameters affecting monolayer organisation of substituted polysaccharides on solid substrates upon Langmuir–Schaefer deposition.* Reactive and Functional Polymers, 2016. **99**: p. 100-106.

20. Yamamura, A., et al., *Wafer-scale, layer-controlled organic single crystals for high-speed circuit operation.* Science Advances, 2018. **4**(2): p. eaao5758.

21. Diao, Y., et al., *Morphology control strategies for solution-processed organic semiconductor thin films.* Energy Environ. Sci., 2014. **7**(7): p. 2145-2159.

22. Uemura, T., et al., *Very High Mobility in Solution-Processed Organic Thin-Film Transistors of Highly Ordered [1]Benzothieno[3,2-b]benzothiophene Derivatives.* Applied Physics Express, 2009. **2**(11): p. 111501.

23. Soeda, J., et al., *Inch-Size Solution-Processed Single-Crystalline Films of High-Mobility Organic Semiconductors.* Applied Physics Express, 2013. **6**(7): p. 076503.

24. Chen, C.-Y., et al., *Continuous blade coating for multi-layer large-area organic light-emitting diode and solar cell.* Journal of Applied Physics, 2011. **110**(9): p. 094501.

25. Michler, G.H., *Electron Microscopy Of Polymers.* 2008.

26. Dykstra, M. and L. Reuss, *Biological Electron Microscopy*. 2003.

27. Ladinsky, M.S., *Chapter Eight - Micromanipulator-Assisted Vitreous Cryosectioning and Sample Preparation by High-Pressure Freezing*, in *Methods in Enzymology*, G.J. Jensen, Editor. 2010, Academic Press. p. 165-194.

28. Wei, L.Y. and T. Li, *Ultramicrotomy of powder material for TEM/STEM study.* Microsc Res Tech, 1997. **36**(5): p. 380-1.

29. Bornside, D.E., C.W. Macosko, and L.E. Scriven, *Spin coating: One-dimensional model.* Journal of Applied Physics, 1989. **66**(11): p. 5185-5193.

30. Niranjan Sahu, B.P., S.Panigrahi, *Fundamental understanding and modeling of spin coating.* Indian J. Physics, 2009. **83**: p. 493-502.

31. C.J. Lawrence, W.Z., *Spin coating for non-Newtonian fluids.* Journal of Non-Newtonian Fluid Mechanics, 1991. **39**: p. 137-187.

32. Batchelor, G.K., *An Introduction to Fluid Dynamics*. Cambridge Mathematical Library. 2000, Cambridge: Cambridge University Press.

33. Mouhamad, Y., et al., *Dynamics of polymer film formation during spin coating.* Journal of Applied Physics, 2014. **116**(12): p. 123513.

34. Flack, W.W., et al., *A mathematical model for spin coating of polymer resists.* Journal of Applied Physics, 1984. **56**(4): p. 1199-1206.

35. Tippo, T., et al., *The effects of solvents on the properties of ultra-thin poly (methyl methacrylate) films prepared by spin coating.* Thin Solid Films, 2013. **546**: p. 180-184.

36. Rossos, A.K., et al., *Photochromism of Amphiphilic Dithienylethenes as Langmuir-Schaefer Films.* Langmuir, 2018. **34**(37): p. 10905-10912.

37. Rossos, A.K., et al., *Synthesis of Bidimensional Prussian Blue Analogue Using an Inverted Langmuir-Schaefer Method.* Langmuir, 2016. **32**(38): p. 9706-13.

38. Becerril, H.A., et al., *High-Performance Organic Thin-Film Transistors through Solution-Sheared Deposition of Small-Molecule Organic Semiconductors.* Advanced Materials, 2008. **20**(13): p. 2588-2594.

39. Deegan, R.D., et al., *Capillary flow as the cause of ring stains from dried liquid drops.* Nature, 1997. **389**: p. 827.

40. Hall, D.B., P. Underhill, and J.M. Torkelson, *Spin coating of thin and ultrathin polymer films.* Polymer Engineering & Science, 1998. **38**(12): p. 2039-2045.

41. Chatterjee, S., S.S. Gadad, and T.K. Kundu, *Atomic force microscopy.* Resonance, 2010. **15**(7): p. 622-642.

42. Butt, H.-J., B. Cappella, and M. Kappl, *Force measurements with the atomic force microscope: Technique, interpretation and applications.* Surface Science Reports, 2005. **59**(1-6): p. 1-152.

43. Binnig, G., C.F. Quate, and C. Gerber, *Atomic force microscope.* Phys Rev Lett, 1986. **56**(9): p. 930-933.

44. Bruslind, L., *Microbiology*. 2017.

45. Aleksandr Noy, D.V.V., Charles M. Lieber, *Chemical Force Microscopy.* Annu. Rev. Mater. Sci., 1997(27): p. 381-421.

46. Ogletree, D.F., R.W. Carpick, and M. Salmeron, *Calibration of frictional forces in atomic force microscopy.* Review of Scientific Instruments, 1996. **67**(9): p. 3298-3306.

47. Mate, C.M., et al., *Atomic-scale friction of a tungsten tip on a graphite surface.* Phys Rev Lett, 1987. **59**(17): p. 1942-1945.

48. Etzler, F.M. and J. Drelich, *Chapter 6 - Atomic Force Microscopy for Characterization of Surfaces, Particles, and Their Interactions*, in *Developments in Surface Contamination*

and Cleaning, R. Kohli and K.L. Mittal, Editors. 2012, William Andrew Publishing: Oxford. p. 307-331.

49.   Johnson, D. and N. Hilal, *Characterisation and quantification of membrane surface properties using atomic force microscopy: A comprehensive review.* Desalination, 2015. **356**: p. 149-164.

50.   Tang, C.Y. and Z. Yang, *Chapter 8 - Transmission Electron Microscopy (TEM)*, in *Membrane Characterization*, N. Hilal, et al., Editors. 2017, Elsevier. p. 145-159.

51.   Brown, R.b.P.D., *Transmission Electron Microscopy-A Textbook for Materials Science, by David B. Williams and C. Barry Carter.* Microscopy and Microanalysis, 2003. **5**(06): p. 452-453.

52.   Oberlin, A., *Electron microscopy of thin crystals by P. B. Hirsch, A. Howie, R. B. Nicholson, D. W. Pashley and M. J. Whelan.* Acta Crystallographica, 1966. **21**(3): p. 454-454.

53.   Perkampus, H.-H., *UV-VIS Spectroscopy and Its Applications*. 1992. p. 3-9.

54.   *Spectroelectrochemistry : theory and practice*, R.J. Gale, Editor. 1988, Plenum Press: New York :.

55.   House, J.E., *Chapter 11 - Molecular Spectroscopy*, in *Fundamentals of Quantum Mechanics (Third Edition)*, J.E. House, Editor. 2018, Academic Press. p. 271-296.

56.   Yossa Kamsi, R.A., et al., *Electronic Structure, Spectroscopic (IR, Raman, UV-Vis, NMR), Optoelectronic, and NLO Properties Investigations of Rubescin E (C31H36O7) Molecule in Gas Phase and Chloroform Solution Using Ab Initio and DFT Methods.* Advances in Condensed Matter Physics, 2019. **2019**: p. 22.

57.   Yahia, L.H. and L.K. Mireles, *4 - X-ray photoelectron spectroscopy (XPS) and time-of-flight secondary ion mass spectrometry (ToF SIMS)*, in *Characterization of Polymeric Biomaterials*, M.C. Tanzi and S. Farè, Editors. 2017, Woodhead Publishing. p. 83-97.

58.   Watts, J. and J. Wolstenholme, *An introduction to surface analysis by XPS and AES*. 2003.

59.   Gandara, F. and T.D. Bennett, *Crystallography of metal-organic frameworks.* IUCrJ, 2014. **1**(6): p. 563-570.

60.   Alhamami, M., H. Doan, and C.-H. Cheng, *A Review on Breathing Behaviors of Metal-Organic-Frameworks (MOFs) for Gas Adsorption.* Materials (Basel, Switzerland), 2014. **7**(4): p. 3198-3250.

61.   Carné-Sánchez, A., et al., *A spray-drying strategy for synthesis of nanoscale metal–organic frameworks and their assembly into hollow superstructures.* Nature Chemistry, 2013. **5**: p. 203.

62.   Gangu, K.K., et al., *A review on contemporary Metal–Organic Framework materials.* Inorganica Chimica Acta, 2016. **446**: p. 61-74.

63. Lee, J., et al., *Metal–organic framework materials as catalysts.* Chemical Society Reviews, 2009. **38**(5): p. 1450-1459.

64. Ahmad, N., et al., *Development of Mixed metal Metal-organic polyhedra networks, colloids, and MOFs and their Pharmacokinetic applications.* Scientific Reports, 2017. **7**(1): p. 832.

65. Feng, D., et al., *Stable metal-organic frameworks containing single-molecule traps for enzyme encapsulation.* Nature Communications, 2015. **6**: p. 5979.

66. Grant Glover, T., et al., *MOF-74 building unit has a direct impact on toxic gas adsorption.* Chemical Engineering Science, 2011. **66**(2): p. 163-170.

67. Li, S. and F. Huo, *Metal-organic framework composites: from fundamentals to applications.* Nanoscale, 2015. **7**(17): p. 7482-501.

68. Zhao, J., et al., *Facile Conversion of Hydroxy Double Salts to Metal–Organic Frameworks Using Metal Oxide Particles and Atomic Layer Deposition Thin-Film Templates.* Journal of the American Chemical Society, 2015. **137**(43): p. 13756-13759.

69. Shekhah, O., et al., *MOF thin films: existing and future applications.* Chem Soc Rev, 2011. **40**(2): p. 1081-106.

70. Bennett, T.D. and A.K. Cheetham, *Amorphous Metal–Organic Frameworks.* Accounts of Chemical Research, 2014. **47**(5): p. 1555-1562.

71. Wee, L.H., et al., *Copper Benzene Tricarboxylate Metal–Organic Framework with Wide Permanent Mesopores Stabilized by Keggin Polyoxometallate Ions.* Journal of the American Chemical Society, 2012. **134**(26): p. 10911-10919.

72. Dolgopolova, E.A. and N.B. Shustova, *Metal–organic framework photophysics: Optoelectronic devices, photoswitches, sensors, and photocatalysts.* MRS Bulletin, 2016. **41**(11): p. 890-896.

73. Kreno, L.E., et al., *Metal–Organic Framework Materials as Chemical Sensors.* Chemical Reviews, 2012. **112**(2): p. 1105-1125.

74. Wen, M., et al., *Design and architecture of metal organic frameworks for visible light enhanced hydrogen production.* Applied Catalysis B: Environmental, 2017. **218**: p. 555-569.

75. Yi, F.-Y., et al., *Chemical Sensors Based on Metal–Organic Frameworks.* ChemPlusChem, 2016. **81**(8): p. 675-690.

76. Xu, Y., et al., *Electrochemistry and electrochemiluminescence from a redox-active metal-organic framework.* Biosensors and Bioelectronics, 2015. **68**: p. 197-203.

77. Lei, J., et al., *Design and sensing applications of metal–organic framework composites.* TrAC Trends in Analytical Chemistry, 2014. **58**: p. 71-78.

78.   Czaja, A.U., N. Trukhan, and U. Müller, *Industrial applications of metal–organic frameworks.* Chemical Society Reviews, 2009. **38**(5): p. 1284-1293.

79.   Lemaire, P.C., et al., *Copper Benzenetricarboxylate Metal–Organic Framework Nucleation Mechanisms on Metal Oxide Powders and Thin Films formed by Atomic Layer Deposition.* ACS Applied Materials & Interfaces, 2016. **8**(14): p. 9514-9522.

80.   Jasuja, H., et al., *Synthesis of Cobalt-, Nickel-, Copper-, and Zinc-Based, Water-Stable, Pillared Metal–Organic Frameworks.* Langmuir, 2014. **30**(47): p. 14300-14307.

81.   Liu, Y., et al., *Catalytic degradation of chemical warfare agents and their simulants by metal-organic frameworks.* Coordination Chemistry Reviews, 2017. **346**: p. 101-111.

82.   Mazaj, M., V. Kaučič, and N. Zabukovec Logar, *Chemistry of Metal-organic Frameworks Monitored by Advanced X-ray Diffraction and Scattering Techniques.* Acta Chimica Slovenica, 2016: p. 440-458.

83.   Walton, R.I., et al., *Uptake of liquid alcohols by the flexible Fe(III) metal-organic framework MIL-53 observed by time-resolved in situ X-ray diffraction.* Chemistry, 2011. **17**(25): p. 7069-79.

84.   Chui, S.S.-Y., et al., *A Chemically Functionalizable Nanoporous Material [Cu$_3$(TMA)$_2$(H$_2$O)$_3$]$_n$.* Science, 1999. **283**(5405): p. 1148-1150.

85.   Zhuang, J.-L., et al., *Rapid Room-Temperature Synthesis of Metal-Organic Framework HKUST-1 Crystals in Bulk and as Oriented and Patterned Thin Films.* Advanced Functional Materials, 2011. **21**(8): p. 1442-1447.

86.   Seetharaj, R., et al., *Dependence of solvents, pH, molar ratio and temperature in tuning metal organic framework architecture.* Arabian Journal of Chemistry, 2016.

87.   Katsiaflaka, M., et al., *Atomically thin monolayers of metal organic frameworks (MOFs) through implementing a Langmuir-Schaefer method.* 2018. **2022**: p. 020007.

88.   Kozachuk, O., et al., *Solvothermal growth of a ruthenium metal-organic framework featuring HKUST-1 structure type as thin films on oxide surfaces.* Chem Commun (Camb), 2011. **47**(30): p. 8509-11.

89.   Ermakova, E.V., et al., *Interfacial self-assembly of functional bilayer templates comprising porphyrin arrays and graphene oxide.* Journal of Colloid and Interface Science, 2018. **530**: p. 521-531.

90.   Andrés, M.A., et al., *Fabrication of ultrathin MIL-96(Al) films and study of CO2 adsorption/desorption processes using quartz crystal microbalance.* Journal of Colloid and Interface Science, 2018. **519**: p. 88-96.

91.   Ohara, H., et al., *Nanoscale deposition of metal–organic framework films on polymer nanosheets.* RSC Advances, 2016. **6**(78): p. 74349-74353.

92. Rubio-Gimenez, V., et al., *High-Quality Metal-Organic Framework Ultrathin Films for Electronically Active Interfaces.* J Am Chem Soc, 2016. **138**(8): p. 2576-84.

93. Benito, J., et al., *Fabrication of ultrathin films containing the metal organic framework Fe-MIL-88B-NH2 by the Langmuir–Blodgett technique.* Colloids and Surfaces A: Physicochemical and Engineering Aspects, 2015. **470**: p. 161-170.

94. Benito, J., et al., *Langmuir-Blodgett Films of the Metal-Organic Framework MIL-101(Cr): Preparation, Characterization, and CO2 Adsorption Study Using a QCM-Based Setup.* ACS Appl Mater Interfaces, 2016. **8**(25): p. 16486-92.

95. Heinke, L., et al., *Surface-mounted metal-organic frameworks for applications in sensing and separation.* Microporous and Mesoporous Materials, 2015. **216**: p. 200-215.

96. Wiktor, C., et al., *Transmission electron microscopy on metal–organic frameworks – a review.* Journal of Materials Chemistry A, 2017. **5**(29): p. 14969-14989.

97. Wiktor, C., et al., *Imaging of intact MOF-5 nanocrystals by advanced TEM at liquid nitrogen temperature.* Microporous and Mesoporous Materials, 2012. **162**: p. 131-135.

98. Jean-Ruel, H., et al., *Ring-closing reaction in diarylethene captured by femtosecond electron crystallography.* J Phys Chem B, 2013. **117**(49): p. 15894-902.

99. Zou Qi, Z.J., Tian He, *Multi-Functional Molecular Switches Based on Photochromic Dithienylethenes.* Progress in Chemistry, 2012(9): p. 1632-1645.

100. Abe, S., et al., *Fatigue-Resistance Property of Diarylethene LB Films in Repeating Photochromic Reaction.* Langmuir, 1997. **13**(20): p. 5504-5506.

101. Fujise, T., et al., *Preparation of Dithienylethene with Amino Groups, and Photochromic Behavior in Langmuir-Blodgett Film of the Amphiphilicdithienylethene.* International Journal of Organic Chemistry, 2013. **03**(02): p. 158-161.

102. Morimitsu, K., S. Kobatake, and M. Irie, *Large geometrical structure changes of photochromic diarylethenes upon photoirradiation.* Tetrahedron Letters, 2004. **45**(6): p. 1155-1158.

103. Theodoratou, A., et al., *Photoswitching the mechanical properties in Langmuir layers of semifluorinated alkyl-azobenzenes at the air-water interface.* Phys Chem Chem Phys, 2015. **17**(43): p. 28844-52.

104. Nishi, H. and S. Kobatake, *Fabrication and Photochromism of High-density Diarylethene Monolayer Immobilized on a Quartz-glass Substrate.* Vol. 39. 2010. 638-639.

105. Ohshima, A., A. Momotake, and T. Arai, *Photochromism, thermochromism, and solvatochromism of naphthalene-based analogues of salicylideneaniline in solution.* Journal of Photochemistry and Photobiology A: Chemistry, 2004. **162**(2): p. 473-479.

106. Ulrich, S., et al., *Visible Light-Responsive DASA-Polymer Conjugates.* ACS Macro Letters, 2017. **6**(7): p. 738-742.

107. Irie, M., Y. Yokoyama, and T. Seki, *New Frontiers in Photochromism*. 2013.

108. Jia, S., et al., *Investigation of Donor-Acceptor Stenhouse Adducts as New Visible Wavelength-Responsive Switching Elements for Lipid-Based Liquid Crystalline Systems.* Langmuir, 2017. **33**(9): p. 2215-2221.

109. Chyla, A., et al. *Photochromic properties of anionic azobenzene amphiphiles in solution and Langmuir Blodgett films*. in *Trends in Colloid and Interface Science XI*. 1997. Darmstadt: Steinkopff.

110. Song, X., J. Perlstein, and D.G. Whitten, *Supramolecular Aggregates of Azobenzene Phospholipids and Related Compounds in Bilayer Assemblies and Other Microheterogeneous Media: Structure, Properties, and Photoreactivity1.* Journal of the American Chemical Society, 1997. **119**(39): p. 9144-9159.

111. Hobley, J., et al., *Laser-induced phase change in Langmuir films observed using nanosecond pump-probe Brewster angle microscopy.* Applied Physics A, 2008. **93**(4): p. 947-954.

112. Nakazawa, T., et al., *Brewster Angle Microscopic Observations of the Langmuir Films of Amphiphilic Spiropyran during Compression and under UV Illumination.* Langmuir, 2004. **20**(13): p. 5439-5444.

113. Tachibana, H., Y. Yamanaka, and M. Matsumoto, *Surface and photochemical properties of Langmuir monolayer and Langmuir–Blodgett films of a spiropyran derivative.* Journal of Materials Chemistry, 2002. **12**(4): p. 938-942.

114. Hirose, T., K. Matsuda, and M. Irie, *Self-Assembly of Photochromic Diarylethenes with Amphiphilic Side Chains: Reversible Thermal and Photochemical Control.* The Journal of Organic Chemistry, 2006. **71**(20): p. 7499-7508.

115. Higashiguchi, K., et al., *Photoinduced macroscopic morphological transformation of an amphiphilic diarylethene assembly: reversible dynamic motion.* J Am Chem Soc, 2015. **137**(7): p. 2722-9.

116. Zou, Y., et al., *Amphiphilic Diarylethene as a Photoswitchable Probe for Imaging Living Cells.* Journal of the American Chemical Society, 2008. **130**(47): p. 15750-15751.

117. Hirose, T. and K. Matsuda, *Photoswitching of chiral supramolecular environments and photoinduced lower critical solution temperature transitions in aqueous media following a supramolecular approach.* Org Biomol Chem, 2013. **11**(6): p. 873-80.

118. Randaccio, L., et al., *Vitamin B12: unique metalorganic compounds and the most complex vitamins.* Molecules, 2010. **15**(5): p. 3228-59.

119. Savage, H., *Water structure in vitamin B12 coenzyme crystals. I. Analysis of the neutron and x-ray solvent densities.* Biophysical Journal, 1986. **50**(5): p. 947-965.

120. O'Leary, F. and S. Samman, *Vitamin B12 in health and disease.* Nutrients, 2010. **2**(3): p. 299-316.

121. Brink-Shoemaker, C., et al., *The structure of Vitamin B12.* Proceedings of the Royal Society of London. Series A. Mathematical and Physical Sciences, 1964. **278**(1372): p. 1-26.

122. Crowfoot Hodgkin, D., et al., *Some Observations on the Structures of Wet and Air-Dried Crystals of Vitamin B12*. Vol. 113. 1960. 30-43.

123. Jones, A.R., *The photochemistry and photobiology of vitamin B12.* Photochemical & Photobiological Sciences, 2017. **16**(6): p. 820-834.

124. Miller, N.A., et al., *Polarized XANES Monitors Femtosecond Structural Evolution of Photoexcited Vitamin B12.* Journal of the American Chemical Society, 2017. **139**(5): p. 1894-1899.

125. Kräutler, B., *Vitamin B12: chemistry and biochemistry.* Biochemical Society Transactions, 2005. **33**(4): p. 806-810.

126. Sension, R.J., D.A. Harris, and A.G. Cole, *Time-Resolved Spectroscopic Studies of B12 Coenzymes: Comparison of the Influence of Solvent on the Primary Photolysis Mechanism and Geminate Recombination of Methyl-, Ethyl-, n-Propyl-, and 5'-Deoxyadenosylcobalamin.* The Journal of Physical Chemistry B, 2005. **109**(46): p. 21954-21962.

127. Demerre, L.J. and C. Wilson, *Photolysis of Vitamin B12.* Journal of the American Pharmaceutical Association (Scientific ed.), 1956. **45**(3): p. 129-134.

128. Brooks, A.J., et al., *Co−C Bond Activation in Methylmalonyl-CoA Mutase by Stabilization of the Post-homolysis Product Co2+Cobalamin.* Journal of the American Chemical Society, 2005. **127**(47): p. 16522-16528.

129. Halpern, J., *Mechanisms of coenzyme B12-dependent rearrangements.* Science, 1985. **227**(4689): p. 869-875.

130. Ariga, K., et al., *Syntheses and monolayer properties of vitamin B 12 derivatives with seven alkyl chains*. Vol. 169. 2000. 47-58.

131. Ariga, K., et al., *Langmuir monolayer of organoalkoxysilane for vitamin B12-modified electrode.* Physical Chemistry Chemical Physics, 2001. **3**(16): p. 3442-3446.

132. Takeshita, N., M. Okuno, and T.A. Ishibashi, *Molecular conformation of DPPC phospholipid Langmuir and Langmuir-Blodgett monolayers studied by heterodyne-detected vibrational sum frequency generation spectroscopy.* Phys Chem Chem Phys, 2017. **19**(3): p. 2060-2066.

8. Appendix

Appendix 1: Substrate treatment protocols

The research interest in manipulating hydrophilicity and hydrophobicity of solid surfaces with either strong or poor affection to water exploded in the last decades. The terms 'hydrophilicity' and 'hydrophilicity' are derived from Greek words *hydro* (water) and *phobos* (fear) or *philos* (friend) and originally referred to properties of molecules. In this thesis, the used substrates needed to be hydrophilic to have a better adhesion of a single layer created on the air–water interface. Hot piranha solution and a glow discharge device can be used to make a surface highly hydrophilic. The recipes and techniques used in this thesis are given below.

1.1   Piranha solution

Sulphuric acid (H_2SO_4, 98%) and hydrogen peroxide (H_2O_2, 30%) at a ratio of 3:1 and at 80–100 $^\circ$C for about 30 min were used to clean the substrates. Since the mixture is a strong oxidizing agent, it removes the organic matter but also hydroxylates most surfaces by adding OH groups, which make them highly hydrophilic. During the process, hydrogen peroxide is added slowly (drop by drop) into sulphuric acid, which is continuously stirred. Then the solution is heated up and the substrates are placed into the solution bath. A special Teflon holder is used for XPS, AFM, and TEM substrates to ease their transfer and proper soaking (Fig. 1). After the piranha solution, the substrates are transferred into distilled water and then blow-dried with compressed nitrogen. Every time piranha solution was used, it was self-prepared due to the self-decomposition of hydrogen peroxide.

Figure 1: Teflon holder used for the piranha cleaning

1.2 Glow discharge

Silicon and silicon nitride substrates were treated by DC glow discharge plasma to improve hydrophilicity. In DC glow discharge, there is a fixed anode as well as a fixed cathode. Electrons are accelerated from cathode to anode, bringing in more energy. On the way to the anode, electrons are led to many collisions with ions and neutrals. During the impacts, they transfer their energy to bonded electrons within ions and neutrals. When the electric field strength reaches a certain level, the free-moving electrons can get enough energy to knock out bonded electrons from neutral particles. A similar process to the mass breakdown takes place in the gas chamber. The electron and ion density are multiplied and finally the whole space is filled with positive and negative ions and electrons. In some cases, a heated filament is used as cathode electrode to emit constant flow of free electrons to help turn on plasma and improve the stability. Evaporated metals from heated filament can sometimes contaminate the sample. The ideal voltage range is between the anode and the cathode to generate the plasma. In case the voltage is too low, free electrons do not have enough energy to ionize the neutrals. If the voltage is too high, electrons move too fast to avoid any collisions with neutrals. The ideal voltage range is a function of gas species and pressure.

Appendix 2: Mechanical stability of DTEs-LB films

A slight decrease in the maximum surface pressure is observed after five cycles, suggesting that the DTEs have some solubility in water (Figure 2). Especially, **1** decreases by ca. 10%, **2** decreases by ca. 6%, and **3** decreases by ca. 4%. However, these changes are not significant. For this reason, Langmuir films of 1–3 are considered reversible and stable.
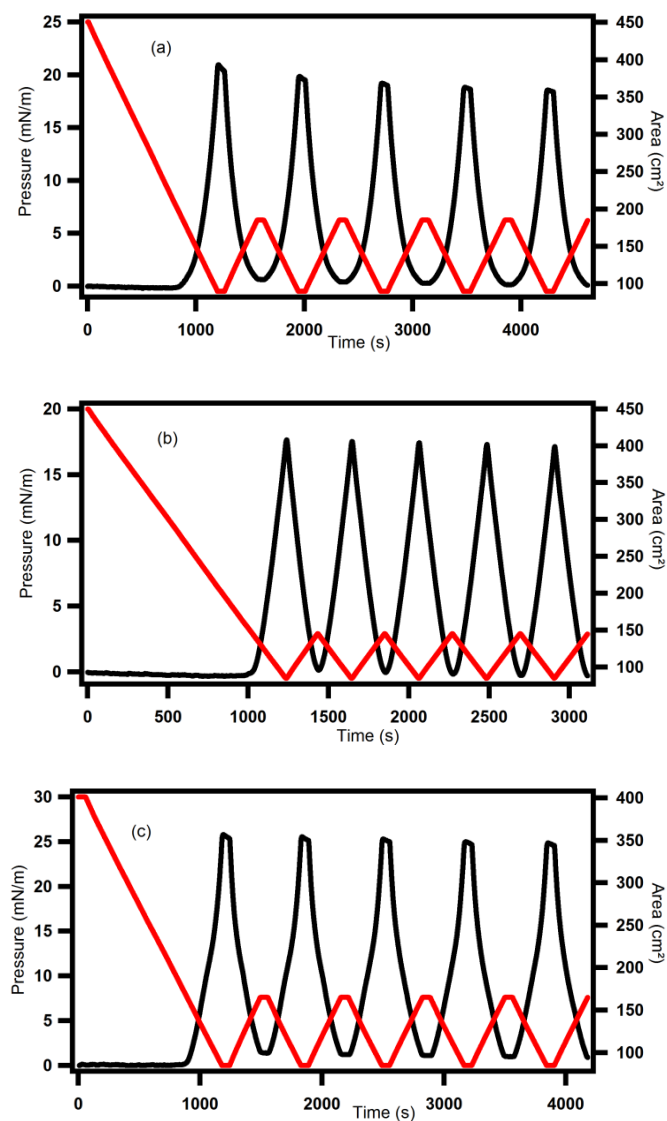
Figure 2: Five sequential compression–decompression cycles to assess the mechanical stability of Langmuir films of (a) **1**, (b) **2**, and (c) **3**. In all cases, the DTE concentration was 0.15 mg mL^{-1} and the transferred volume was 150 μL.

Appendix 3: Synthesis of dithienylethene derivative 3

DTE **3** was designed for Langmuir film and LS film studies. To enhance the amphiphilicity of the DTE core, a large branched alkyl substituent and a cationic methylpyridinium substituent were incorporated. Additional methyl groups were incorporated at the reactive carbons, as similar derivatives often display high fatigue resistance, quantum yields, high photoconversions, and efficient photochromism as crystalline solids.

The synthesis of **3** began with the conversion of an alkyl aryl ketone to a tertiary alcohol **4** via a Grignard reaction. Dehydration of **4** and the in situ reduction of the alkene intermediate using borane-dimethyl sulphide gave **5**, installing the branched alkyl substituent. Thereafter, **5** was conveniently converted to the corresponding boronic acid, which was used without further purification in a Suzuki–Miyaura reaction with 2,4-dibromo-3,5-dimethylthiophene. Subsequently, **6** was coupled with 4-(2,3,3,4,4,5,5-heptafluoro-1-cyclopenten-1-yl)-3,5-dimethyl-2-(4-pyridyl) thiophene to give **7**. Finally, methylation of **7** with methyl triflate produced the amphiphilic DTE **3** (Figure 3).
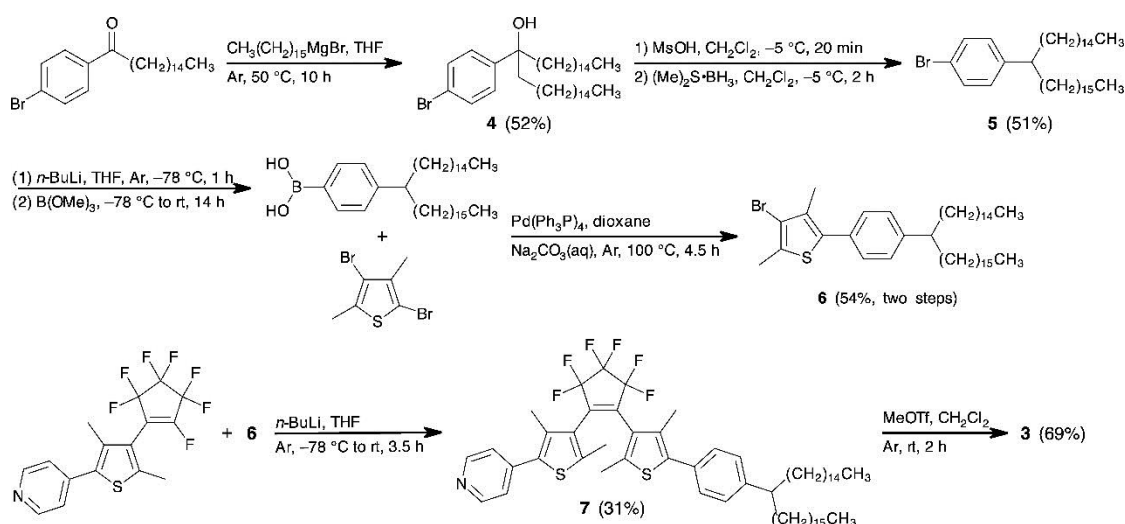
Figure 3: Synthesis of derivative **3**. Figure adapted with permission form [36]

Appendix 4: List of hazardous substances

Below is a list of the hazardous substances used in this work. They are marked with the relevant pictograms, as well as the H (hazard) and P (precautionary) statements.

Substance	Pictogram	H-statements	P-statements
Acetone		225, 319, 336	210, 261, 305+351+338
Benzene		225, 304, 315, 319, 340, 350, 372	201, 210, 301+310, 305+351+338, 308+313, 331
Chloroform		302, 315, 319, 332, 336, 351, 361, 373	261, 281, 305+351+338
Dimethylformamide		226, 312, 319, 332, 360	280, 305+351+338
Ethanol		225, 319	210, 240, 305+351+338, 403+233
Ferric chloride		290, 302, 314, 318	234, 260, 264, 270, 273, 280, 301+312, 301+330+331, 303+361+353,

			363, 304+340,310, 321, 305+351+338, 390, 405, 406, 501
Hexane		225, 304, 315, 336, 373, 411	210, 261, 273, 281, 301+310, 331
Hydrogen peroxide		271, 302, 314, 332, 335, 412	2201, 280, 305+351+338, 310
Methanol		225, 301, 311, 331, 370	210, 233, 240, 241, 242, 243, 260, 264, 270, 280, 301+310, 303+361+353, 304+340, 330, 363, 370+378, 403+233, 235, 405, 501
Sulphuric acid		314	260, 264, 280, 301+330+331, 303+361+353, 363, 304+340, 305+351+338,

			310, 321, 405, 501
Toluene		225, 361d, 304, 373, 315, 336	210, 240, 301+310, 302+352, 308+313, 314, 403+233

9. Acknowledgments

discussions, culture, language exchange and the food experiences. Days got better and drunker with you guys!!! Special thanks to Albert Casandruc for all the help, advise but mostly for the good time.

None of these would have been possible without my wonderful family. I am especially grateful to my parents Kostas Katsiaflakas and Vefa Kogiou for always supporting me in every decision I made. I have to apologize for worrying them with all my adventures during these years. I would also like to thank my grandma, Evangelia Kogiou for the nice discussions we had on the phone every week. Special thanks to my brothers Giorgos and Giannis Katsiaflakas for making their visits to Hamburg memorable. I am really lucky having you all.

10. Declaration on oath

''I hereby declare on oath, that I have written the present dissertation by my own and have not used other than the acknowledged resources and aids. The submitted written version corresponds to the version on the electronic storage medium. I hereby declare that I have not previously applied or pursued for a doctorate (PhD studies).'' 16.01.2019